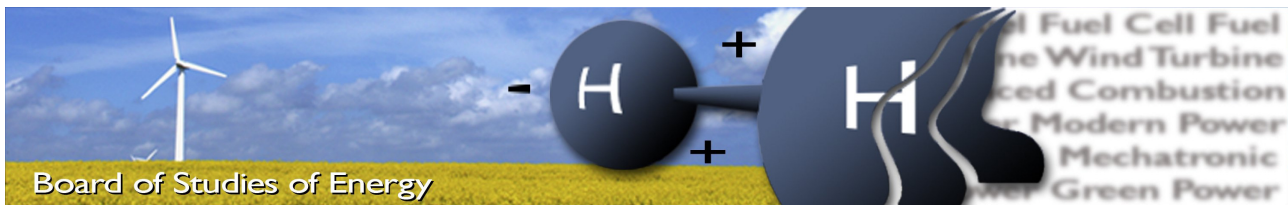# MPPT Wind and Photovoltaic using multiple input DC/DC converter

Group:?
Aalborg University
Department of Energy Technology
June 1, 2014

Board of Studies of Energy

Title:	Current Control of a multiple input DC/DC converter
Semester:	4rd semester M.Sc., PED4
Semester theme:	Optimization, Diagnosis and Control of Power Electronic Drives or Converters
Period:	01/02-2014 - 1/06-2014
ECTS:	30
Supervisor:	Erik Schaltz
Project group:	

Andres Lopez-Aranguren Oliver

Number of reports:2
Number of pages: 107
Appendix pages:10
CD's: 2

ABSTRACT:

The purpose of this project is to design and build a double input DC/DC converter for controlling a hybrid system formed by a photovoltaic system and a vertical axis wind turbine, with the goal of tracking the maximum power point. Both power generation systems must be deeply studied in order to understand their principle of working and find the most optimum MPPT algorithm for this purpose. Once the MPPT algorithm has been selected, it will be simulated with both power generation models. Several multiple input power converter topologies will be analysed and the most suitable for this application will be studied.A simulation will be carry on using the models developed for this purpose in order to study its behaviour. The selected double input converter will be simulated and the control system will be tested in the simulation. Finally it will be built and tested in the laboratory first and afterwards with both power generation systems.

By signing this document, each member of the group confirms that all participated in the project work and thereby that all members are collectively liable for the content of the report.

Resume

Renewable energies sources are becoming really important since the last decade. However due to the fact that they extremely depend on weather conditions, the usage of power electronics systems to extract the maximum power and controlling the energy flow becomes an essential issue.

This project is based on a hybrid system formed by a vertical axis wind turbine and a photovoltaic system. The project is developed in Nicaragua, in collaboration with the national engineering university of Managua, with the purpose of improve the quality of life of people in the communities by bringing them electricity through renewable energies.

This project start with an overview of the system, based on a vertical axis wind turbine developed by students from the UNI and a photovoltaic system.

A deep research about both power generation system is done in order to understand the behavior of these renewable energy under weather changes.

Afterwards, different maximum power point tracking algorithms are studied and the one most suitable for this application is selected and analysed.

Double input converters are studied and the one considered more appropriate for this aplication is analysed and simulated.

Finally the double input DC/DC converter selected is designed and built. Some laboratory test are done in order to verify its behaviour under different scenarios.

Preface

This report is produced by a 10th semester student from Institute of Energy Technology at Aalborg University. This project is done in

I would like to address many thanks to Erik Schaltz my supervisor from Aalborg University and to my supervisors of the UNI of Managua, Jernimo Zeas, head of the Wind Energy Department and Jose Manuel Arcia from the Electronic department, for helping me throughout this project and for giving me constructive criticism. Furthermore I would like to direct a big thanks to my family and friends for encouraging me and for being proud of what I do.

Reading instructions

The report will have a short introduction and an ending at each section. There will throughout the project be source references.They are written using Harvard method which means the sources are written as follows, [Surname, Year]. If only a single source is used in a chapter or a section it is found at the end. If multiple sources are used in a chapter they the will be found immediately after each text section. All sources are assembled in a bibliography at the back of the report. An explanatory text is found under every figure, and table. In the start a nomenclature list is found where all units, abbreviations, and parameters are listed. On the enclosed CD, all relevant data from simulations and laboratory test and computer models are saved. In addition there is a PDF-version of the project attached to the CD.

Table of Contents

List of Symbols

Symbol	Description	Units
A	Swept area of the blades	m^2
C_p	Coefficient of performance	–
D	Duty ratio of a PWM signal	–
d	Distance of the movement	m
$\bar{E}_a$	Distance of the movement	m
H	Height of the Wind turbine blades	m
$\bar{I}_a$	Phase-a stator current	A
I_{DC}	Output current of the rectifier	A
I_{PV}	Photovoltaic module current	A
I_{SC}	Photovoltaic module Short Circuit Current	A
I_d	Photovoltaic module Diode current	A
I_o	Photovoltaic module dark condition current	A
q	Electron charge	C
J	Inertia	kg/m^2
k	Boltzmann constant	J/K
m	Unity of mass	kg
U	Kinetic energy	J
$\bar{V}_{an}$	Phase-a stator voltage	V
v_w	Wind speed	ms
V_{DC}	Ouput voltage of the rectifier	V
V_{PV}	Photovoltaic module voltage	V
V_{OC}	Photovoltaic module Diode current	V
V_d	Single cell output voltage	V
$V_b att.$	Battery voltage level	V
pp	Number of pole pairs	–
q	Actual battery capacity	C
q_{max}	Nominal battery capacity	C
R_e	Incident radiance	$kHz/\left(\mu W/cm^2\right)$
R_m	Measuring resistor	Ω
R_s	Measuring resistor	Ω
$T_e mm$	Electro-mechanical Torque	Nm
T_m	Mechanical Torque	Nm
w_e	Electrical speed	rad/s
w_m	Mechanical speed	rad/s
$w_m o$	Cut-in Mechanical speed	rad/s
x	Space of the movement	m
X_s	Stator reactance	Ω
ρ	Density	kg/m^3
λ	Tip spit ratio	–

Abbreviations

| Description	Acronym
Alternating Current	AC
Analogue to Digital Conversion	ADC
Ampere-Hour	Ah
Depth of Discharge	DOD
Direct Current	DC
Horizontal Axis Wind Turbine	HAWT
International Energy Agency	IEA
LED	Light Emitter Diode
Maximum Power Point Tracking	MPPT
Nickel Cadmium	Ni-Cad
Pulse Width Modulation	PWM
Permanent Magnet Synchronous Generator	PMSG
Personal Computer	PC
Photovoltaic	PV
Renewable Energy Sources	RES
Real Time Clock	RTC
State of discharge	SOC
Vertical Axis Wind Turbine	VAWT

Chapter 1

Introduction

1.1 Background

In the last decade, the concept of climate change has become a central issue for governments in all over the world. This fact forced governments to make a big investment in renewable energies, with the challenge of pursuing the research and development of alternative energies, which are now more efficient and reliable. In addition, renewable energies are becoming increasingly cost-competitive with other non renewable energy sources.

The access to the electricity is essential for the development of people in poor countries. However, the International Energy Agency(IEA) estimated in 2011 that there was approximately 1.2 billion people living without access to electricity. Extending the national grid to remote and inaccessible areas can be extremely costly and it is usually not feasible for non developed countries. However, it is possible to be achieve universal access to electricity though renewable energies

Nicaragua is the second poorest country in Latin America and 28% of its population does not have access to electricity [1]. However, this country possess a big potential in the context of renewable energy sources. Nicaragua is third-highest country in terms of renewable energy potential of Latin America, with an amount of approximately 4.500 MW of renewable energy generation potential, between geothermal, hydroelectric, biomass and wind sources [18]. In fact, thanks to its natural resources, the country could generate nine times more energy from renewable than it consumes and could sell excess energy across its borders thanks to this outstanding potential.

Figure 1.1 shows the irradiation map of Nicaragua in which the high irradiation potential can be observed. The wind power potential of the country is shown in Figure 1.2.
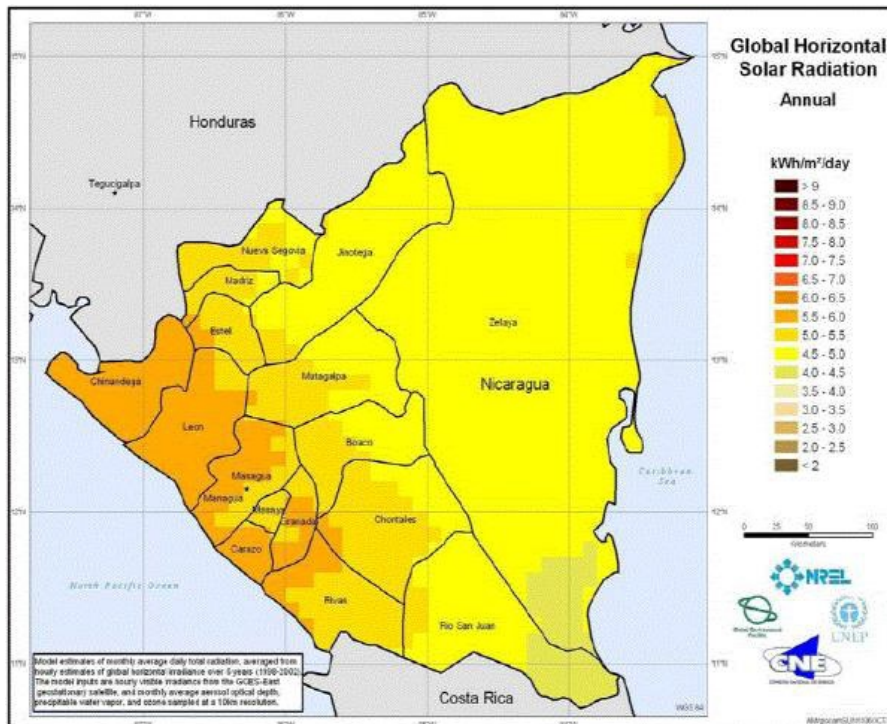
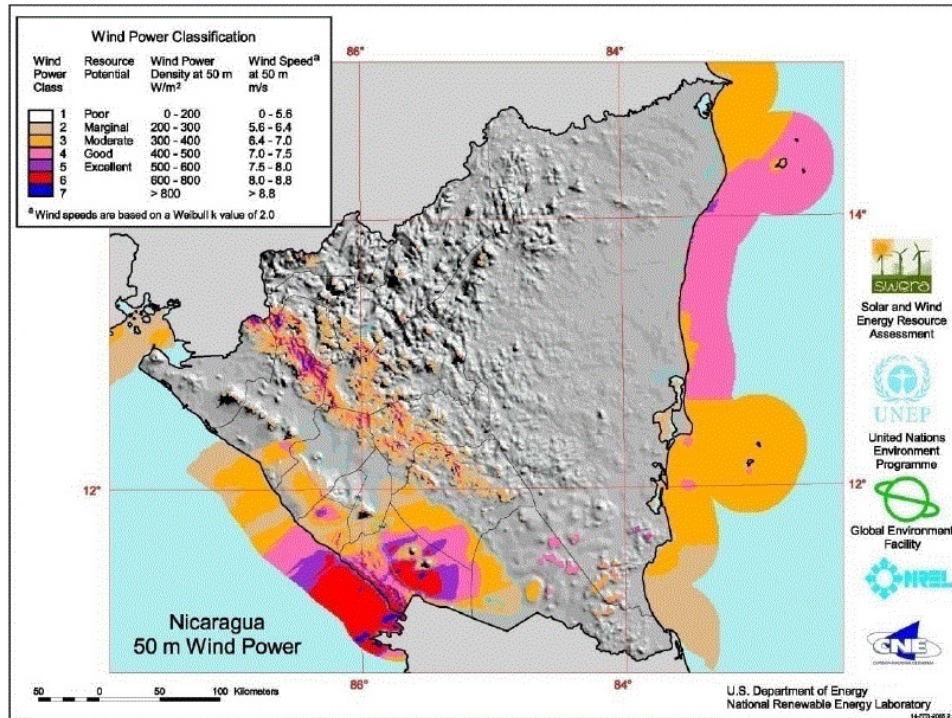*Figure 1.1.* Solar irradiation map of Nicaragua.

Figure 1.2. Map of the wind power clasification in Nicaragua

The usage of power electronics is indispensable for controlling renewable energy sources. Due to the high initial installation cost of either wind or photovoltaic systems, being able to extract the maximum power from the wind or sun and maximize the efficiency in conversion and energy storage becomes essential. In addition, the fact that renewable energy sources as photovoltaic energy and wind energy heavily depend on climate and weather conditions makes indispensable to continuously extract the maximum available power.

The usage of power converters in renewable energy systems allows to vary the operating point of these alternative sources in such a way the maximum possible power is extracted. Therefore the behaviour of the system is optimize for different conditions such wind speed, solar irradiation, cell temperature or load levels, by tracking the maximum power point(MPPT). Different techniques for tracking the maximum power point of both solar and wind power generation system are employed nowadays.

If the efficiency of renewable power generation systems is optimise, expenditures in initial installation are decreased and therefore the overall cost of alternative energy system is reduced, making them for accessible for everyone.

As the available power from renewable energy sources is intermittent and stochastic, if different but complementary alternative energies as wind and sun are combined could lead into a more reliable system which can continuously fed the load demand. This technology is called hybrid systems and it is becoming popular in the field of energy generation systems, due to its reliable operation, cleanliness and efficiency compared with single source energy systems.

Hybrid systems are a combination of different energy sources which have different $V - I$ characteristic and they are usually connected through different power converters [8]. However, by using several DC/DC power converters the overall cost of the system is high and the configuration becomes relatively complex.

Power converters for controlling hybrid systems can be simplified by using what it is called multiple input converters(MIC). Having a single system with several inputs simultaneously controlled and the energy produced independently can be added depending on the load demand, reduce the overall cost of the system, the complexity of hybrid systems and facilitates the synchronization and control of the

renewable energy sources [8].

Figure 1.3 shows a basic hybrid system formed by a small horizontal axis wind turbine(HAWT) and photovoltaic panels. Both power generation systems are connected to a hybrid controller which regulates the charge of the batteries using both renewable energy systems.
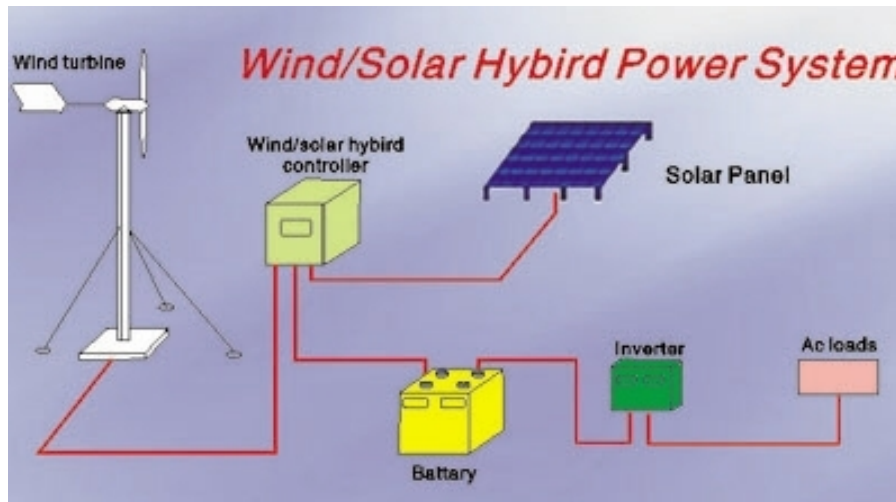
Figure 1.3. Hybrid system supplied by photovoltaic system and wind power generation system. A hybrid controller is connected to control the charge the batteries.

The aim of this report is to design a double input DC/DC converter which can control the power generated by a hybrid system formed by a vertical axis wind turbine and a photovoltaic module, maximizing the power generated by both renewable input sources and controlling the charge of a battery.

The motivation for making this report is to contribute to the develop of the usage of renewable energies in Nicaragua by designing a real system which can control the power generated by both solar and wind energy systems. Hybrid and MISO systems are becoming a new tendency in the field of renewable energy systems, which makes the goal of this project a real challenge.

The whole process of this research is done in Nicaragua in collaboration with the Engineering National University of Managua.

1.2 Problem Statement

The considerably dependency of wind and solar power generation systems from external conditions, makes these renewable energy systems unpredictable and sometimes unreliable. Hybrid systems can combine both complementary energy sources, maximizing and optimizing its output power through a maximum power point technique can solve make renewable energy systems to be more reliable and efficient.

The main focus of this report is to design and develop a double input DC/DC converter which can control and sum the power produced by a hybrid system. The hybrid system is formed by a wind power generation system and a photovoltaic module. The wind power system consist on a vertical axis wind turbine and a permanent magnet synchronous generator developed by students of the UNI(Engineering National University of Nicaragua).

The power converter must extract the maximum available power from both generation systems in order to fed the load demand and control charge of a battery. In order to achieve the final goal, it is required first to fully understand the principle of working of both alternative energy generation systems and the different maximum power point tracking techniques.

1.3 Objective

The objective of this project is to design and build a double input DC/DC converter for a hybrid system formed by a VAWT and a photovoltaic module, both in simulations and in a real system provided by the UNI. This includes an study of both power generations systems, different maximum power point techniques will be studied and simulated in order to find the most suitable for this application. It is required to do an study of different multiple input power converters and analysing the final system selected for this purpose. A further objective is to improve the system so it can be used in communities in Nicaragua and people can be benified by this technology.

1.4 Methodology

First the system overview is explained in Chapter I. Wind energy systems are analysed and studied in Chapter II as well as the MPPT tracking algorithm is simulated with the wind turbine model developed for this purpose. In Chapter III photovoltaic energy is studied. In Chapter IV multiple input DC converter are showed and analysed. Chapter V shows the MIC converted selected and the small signal analyses. Finally in Chapter IV the system design is explained and laboratory results are showed
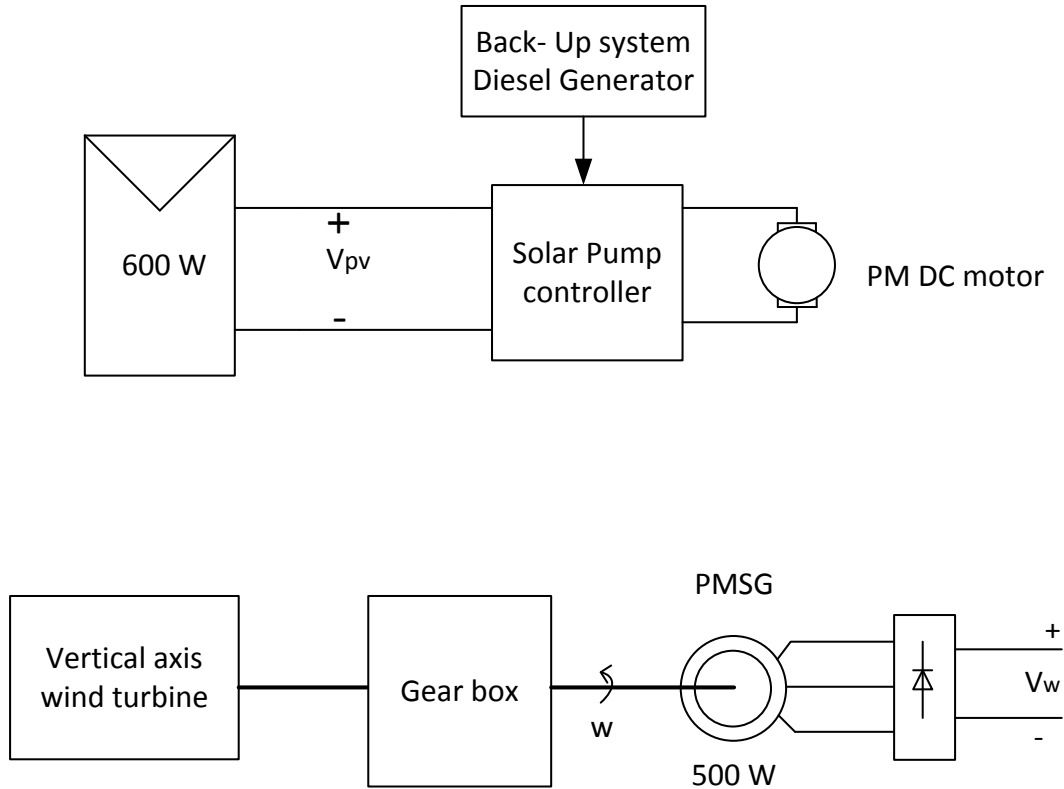
Chapter 2

System description

In this chapter a general description of the hybrid system is presented. The essential system model parts are presented for a better understanding of the goal of this report.

Figure 2.1. Diagram of the current system needed to be improved. The solar system supplying the DC load on the top and the wind generator on the bottom.

The initial system is formed by a 600 W PV-stand alone system used to supply a submersible water pump for an irrigation system. The power generation system is based on three PV modules which main electrical characteristics are shown in Table 2.1. Where the maximum output power is P_{mp}=200 W, the open circuit Voltage V_{OC}=34.53 V , the short circuit current I_{SC} =7.96 A, the maximum power voltage V_{mp}=27 V and the maximum power current I_{mp}=7.41 A.

Table 2.1. 200W-PV module electrical characteristics

PV Modules	
P_{mp}	200 W
V_{OC}	34.53 V
I_{SC}	7.96 A
V_{mp}	27 V
I_{mp}	7.41 A

The submersible water pump is the GRUNDFOS SQFLEX model 11SQF-2. It is a helical rotor pump

formed by a brushless, electronically commutated AC-motor with a permanent-magnet rotor. These motors are called electronically commutated motors(ECM), which can be either powered with AC current or with DC though an integrated inverter. This motor has a nominal power of P_n=0.9 kW, the DC supply voltage is in the range of V_{DC}=[30;300] V, the AC supply voltage V_{AC}= [90;240] V, the input nominal current is I_n=7 A, the power factor PF =1 and the speed is n_n=[500 ;3000] rpm. Table 2.2 shows the electrical characteristics previously mentioned.

Table 2.2. SQFLEX GRUNDFOS submersible power pump electrical characteristics

AC PM motor	
V_{DC}	[30;300] V
V_{AC}	[90;240] V
P_n	0.9 kW
I_n	7 A
PF	1
n_n	[500 ;3000] rpm

The submersible pump has its own controller which protects the pump against dry-running protection and it has a water level switch for a water tank or reservoir. In addition in case the PV modules has not enough power to run the pump, it rectifies the signal from an AC generator.

In Figure (2.1) the initial system is shown. The vertical axis wind turbine system is not used yet for the need of a controller. It is connected to a 500 W three phase Permanent Magnet Synchronous Generator. For rectifying the output voltage, a 3-Phase rectifier is used.

Table (2.3) shows the electrical characteristic of the PMSG.

Table 2.3. System PV configuration rated values

Permanent magnet Synchronous Generator electrical characteristics	
Rated Mechanical Power	500 W
Rated Rotor Speed	419 RPM
Number of Pole Pairs	6
V_{LL}	18.5 V
I_{LL}	34 A
Stator Winding Resistance	0.8 Ω
Stator Synchronous Reactance	1.22 Ω
Permanent magnet flux linkage	0.165 Wb
Connexion	Star connexion

In the previous system, both the Photovoltaic and the wind turbine system require a MPPT controller for better performance. It is also required a controller for braking the wind turbine in case of really high wind speeds.

The aim of this project is to design a controller which can add the energy produced by both systems to fed the load or in case only one is producing energy, they system still works.

A battery pack will be added to the output of the controller so the energy can be stored and it can be used during the night. Thereby it is required that the controller also includes a charge algorithm for the batteries.

Figure 2.2 shows the hybrid system simultaneously controlled by a multiple input DC/DC converter. The control unit reads the output voltage and current from both generation systems and the output

voltage and current of the controller.

By comparing the read signals and the reference voltage or current, the control unit generates the control signal for the DC/DC converter to operate as desired. The control unit also reads the current from the batteries. Most of the charge controllers evaluate the SOC(State of Charge) of the battery by reading the voltage battery level. However, it is more accurate to read the current coming into the battery and the current used by the load to estimate the battery charge level.
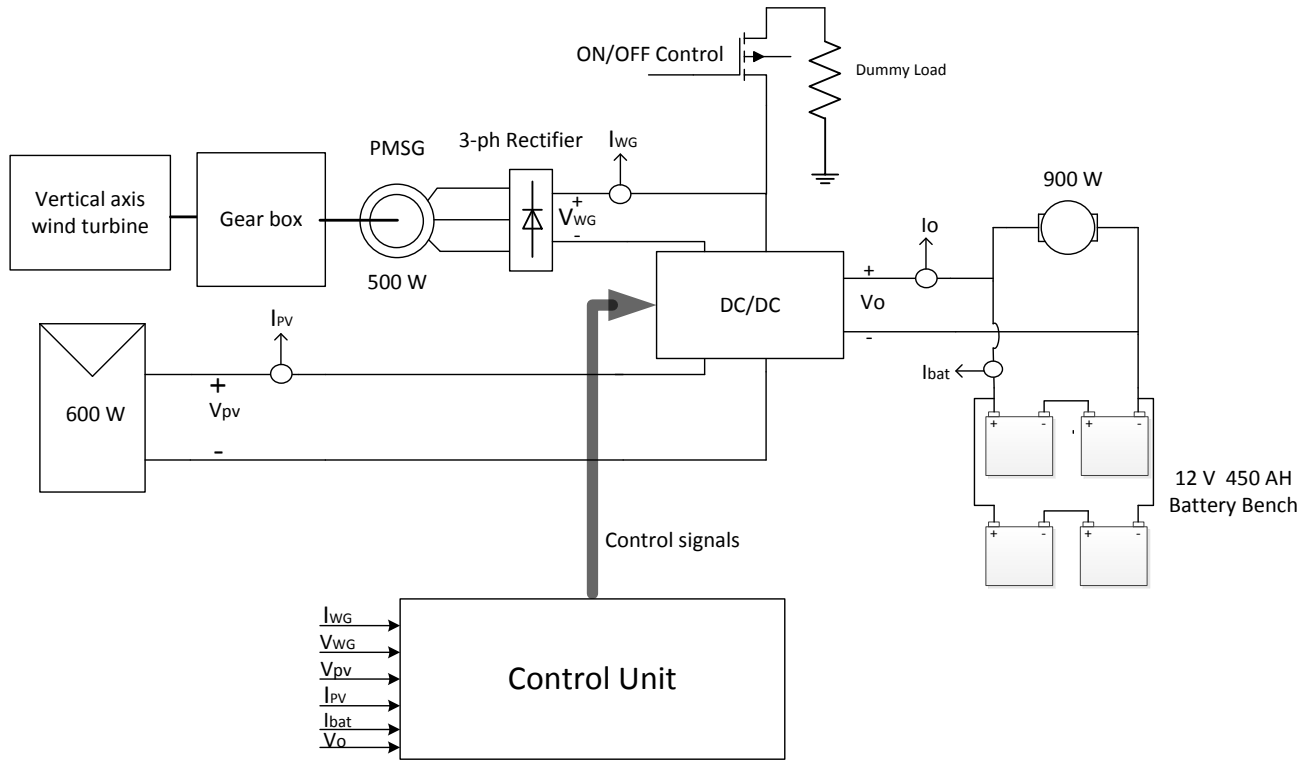
Figure 2.2. Prosed system with a double input DC/DC converter connected to the load and the batteries. The inputs are the rectifier of the wind turbine and the solar array. The control unit reads the DC/DC converter input current and voltage, battery voltage and current and it generates the control signals for the converter.

Figure **??** shows the helical axis wind turbine used for this project as well as the PMSG developed by students from the National University of Managua:

In this chapter, the system to be improved has been presented. A generated description of both generation systems(wind turbine and photovoltaic system) has been done and a general idea of the solution proposed has been given. In the next chapters, theory of both generation systems will be explained and the control system will be studied and implemented.

Figure 2.3. Picture of the wind turbine system used for this project, formed by the helical wind turbine and the permanent magnet syncronous generator designed by students of the UNI

Chapter 3

Wind Energy systems

Domestic wind turbines are used for several purposes, they are usually used to supply energy to small micro-grid systems or urban applications. There are different wind turbine designs available on the market and they can be studied into two groups, Vertical Axis Wind Turbines(VAWT) and Horizontal Axis Wind Turbines(HAWT).

Figure 3.1 shows a diagram of both types of domestic wind turbines, VAWT and HAWT:
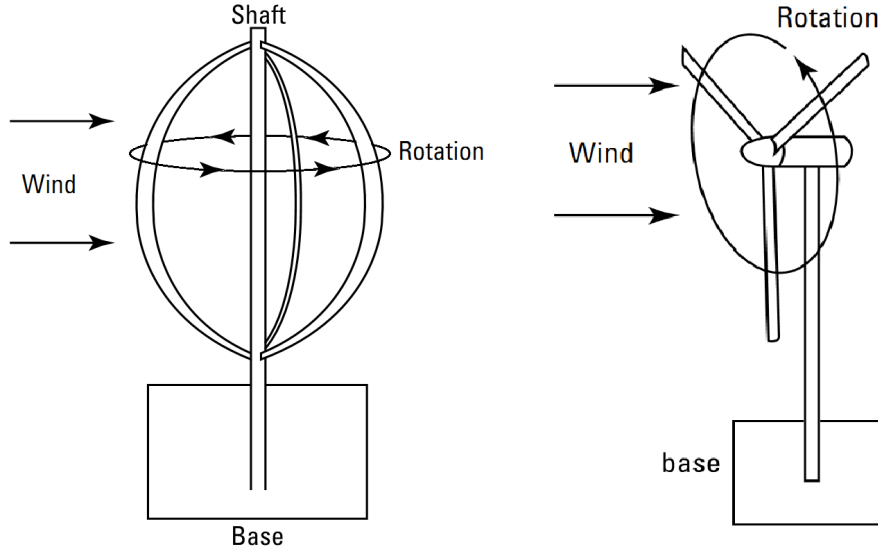
Figure 3.1. Vertical axis wind turbines (VAWT) and Horizontal Axis Wind turbines(HAWT) [9].

VAWT is believed to be the most suitable design for urban wind environment, which is characterised for having high fluctuations regarding wind direction and wind speed. It presents a suitable response for turbulent wind areas and Its vertical blades arrangement makes this type of wind turbine undependable of the wind direction [2]. In addition, noise reduction is achieved with VAHT design due to its performance at lower tip spit ratio than the HAWT.

3.1   Wind energy power generation systems

The energy of the wind is treated as kinetic energy which is produced by particles with a certain mass, m floating with a certain speed, V_w. The kinetic energy U of any fluid is defined as shown in Equation 3.1:

$$U = \frac{1}{2}m \cdot v_w{}^2 = \frac{1}{2}\rho \cdot A \cdot x \cdot v_w{}^2 \qquad \text{[J]}$$

(3.1)

where m is the mass of the fluid and v_w is the fluid speed. The mass can be expressed in function of the density, ρ (which in this case is the air density), the swept area, A and x the distance of the movement.

The power is defined as the variation of the energy during a timespan, $P = \frac{\Delta U}{\delta t}$. If there is any movement, the distance changes with the time and the variation of distance with respect to time is equal to the speed. Thereby, Equation 3.1 can be expressed as follows (3.2):

$$(3.2) \qquad\qquad P_{m,ideal} = \frac{1}{2}\rho \cdot A \cdot v_w{}^3 \qquad\qquad [W]$$

However, it is not possible to extract the total amount of energy in the wind. The phenomenon of the energy absorbed by a wind turbine is shown in Figure 3.2 :
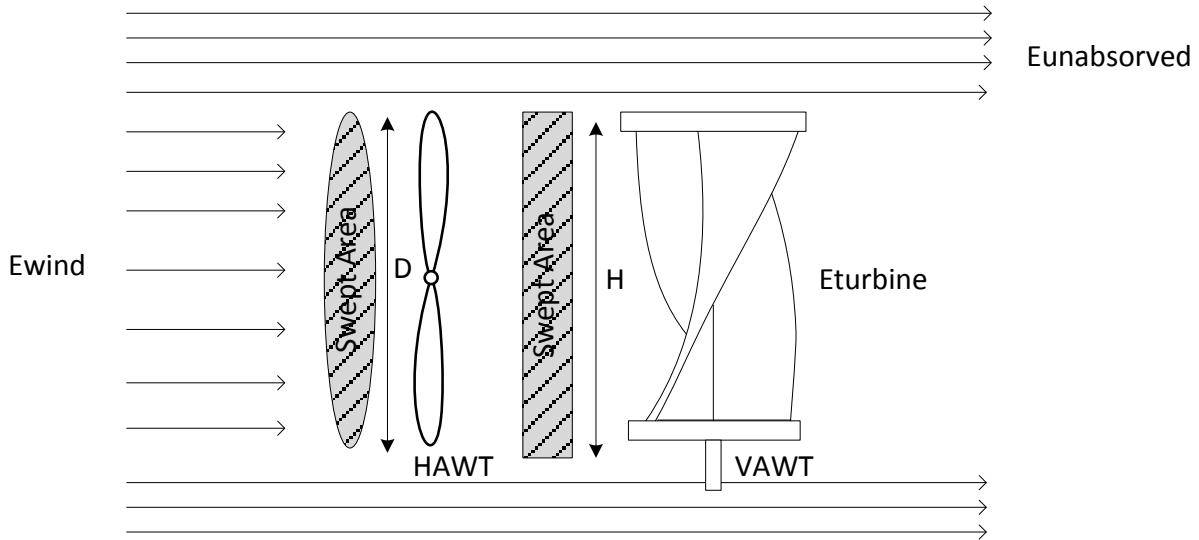
Figure 3.2. Energy absorbed by the wind turbine blades, where D is the diameter of the HAWT blades and H the height of the VAWT blades. The wind impacts on the swept area and the wind energy is transformed into mechanical energy.

As shown in Figure 3.2 not all the wind energy is absorbed. The Betz limit is defined as the maximum kinetic energy which a wind turbine can absorb and transform into mechanical energy from the wind. This coefficient is 59.3% and it defines the theoretical maximum power which can be extracted from any wind turbine [6].

The power coefficient C_p is defined as the power produced by the wind turbine divided by the total power available on the wind:

$$(3.3) \qquad\qquad C_p = \frac{P_{Turbine}}{P_{Wind}} \qquad\qquad [-]$$

where P_m is the mechanical power in the rotor of the wind turbine.

The power extracted from the wind is depending on the power of performance, C_p as previously explained. Therefore, Equation 3.2 can written as in (3.4):

$$(3.4) \qquad\qquad P_m = C_p(\frac{1}{2}\rho \cdot A \cdot v_w{}^3) \qquad\qquad [W]$$

The coefficient of performance, (C_p) of Equation 3.4, is limited to a maximum of 0.59 (Betz's limit), which is essentially depending on the tip speed ratio λ.

The tip speed ratio (λ) is the ratio between the rotational speed of the blades and the velocity of the wind, v_w. It is defined in Equation 3.5:

$$\lambda = \frac{w_m \cdot R}{u_w} \qquad [\text{-}]$$

(3.5)

where R is the radio of the wind turbine, w_m the rotor angular speed and u_w the wind speed.

The tip speed ratio plays an important role when designing wind turbines, they are designed to extract as much power out of the wind as possible. The rotor can not rotate neither too slow nor too quickly so the blades must let pass the proper amount of wind. For low speed wind turbines higher number of blades is needed to cover more area of the wind, and for high speed wind turbines less blades are needed.

In Figure 3.3 the coefficient of power as a function of the tip spit ratio, λ for various types of wind turbines is shown.
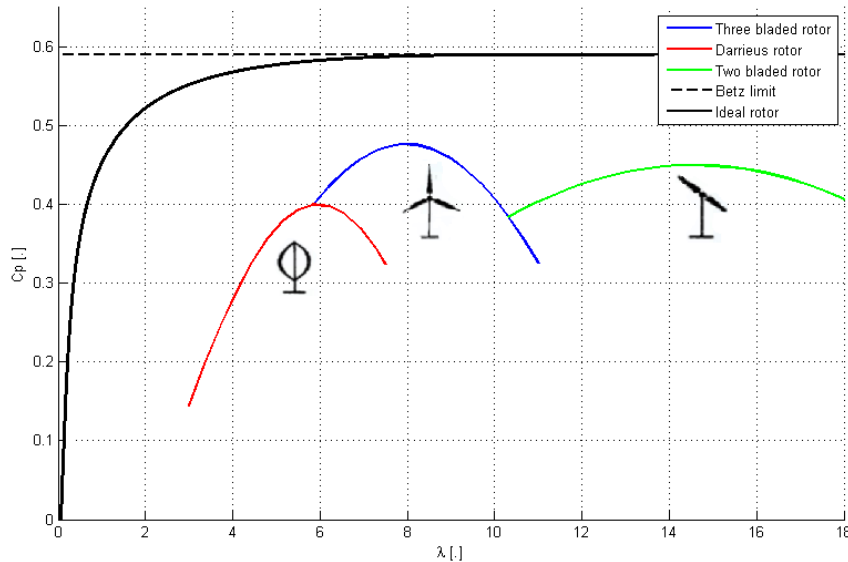
Figure 3.3. Coefficient of performance depending on the tip spit ratio for different types of wind turbines [9].

As seen in Figure (3.3) the tip spit ratio changes for different type of wind turbines. The Betz limit curve reaches the 0.59 and the different types are lower than this limit.

It must be denoted that C_p also depends on the pitch angle β, which is the angle between the position of the blades and the wind direction. However, due to the fact that this report is focused on a VAWT, this parameter will not be considered.

Figure 3.2 shows the vertical axis wind turbine helical blades used for this study. The area of the blades attacked by the air is a rectangle where H is the heigh of the blades and D the diameter of the rotating surface.

The mechanical power equation applied to this type of wind turbine can be rewritten as follows (3.6):

$$P_w = v_w{}^3 C_p(\lambda)(\frac{1}{2}\rho \cdot H \cdot D) \qquad [\text{W}]$$

(3.6)

Equation 3.4 shows the relation between the mechanical torque produced by the vertical axis wind turbine depending on the wind speed.
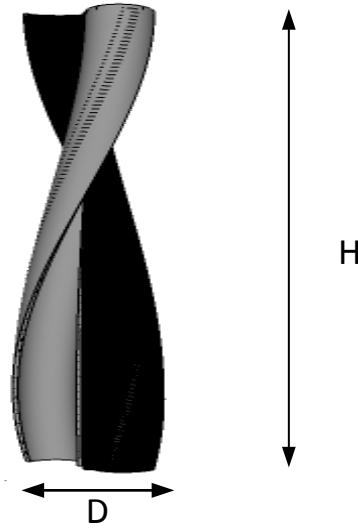
Figure 3.4. Vertical axis vind turbine with helical blades where H is the height of the blades and D the length

The relation between the torque and the mechanical power is shown in Equation 3.7.

$$(3.7) \qquad\qquad T = \frac{P_m}{w_m} \qquad\qquad \text{[N m]}$$

From Equation3.24 and 3.7, Equation 3.8 can be derived:

$$(3.8) \qquad\qquad T_m = \frac{C_p(\lambda) \cdot v_w{}^2 (\rho \cdot H \cdot D^2)}{\lambda} \qquad\qquad \text{[N m]}$$

3.2   Permanent Magnet Synchronous Generator and three phase rectifier

The mechanical power produced in the shaft of the generator is defined as:

$$(3.9) \qquad\qquad P_m = T_m \cdot \omega_m \qquad\qquad \text{[W]}$$

where T_m is the wind turbine mechanical torque and ω_m is the rotor mechanical speed.

The mechanical equation of a PMSG is defined as follows (3.10), neglecting the viscous friction:

$$(3.10) \qquad\qquad T_m - T_{em} = J\frac{d\omega_m}{dt} \qquad\qquad \text{[N m]}$$

where T_{em} is the PMSG electromagnetic torque and J is the wind turbine's moment of inertia .

In the same way the equation of the power is defined as shown in (3.10):
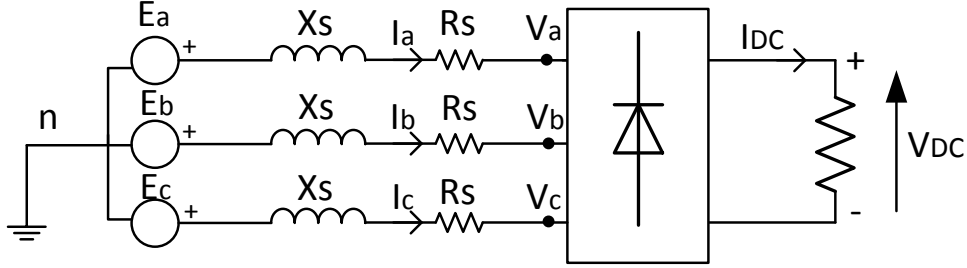
$$(3.11) \qquad\qquad P_m - P_g = \omega_m \cdot J\frac{d\omega_m}{dt} \qquad\qquad \text{[W]}$$

When the system reaches the steady state, the mechanical torque is equal to the electromagnetic torque (3.12):

$$(3.12) \qquad\qquad T_m = T_e \qquad\qquad \text{[N m]}$$

The simplified equivalent circuit of a Permanent Magnet Synchronous Generator is shown in Figure 3.5.

Figure 3.5. Equivalent circuit of a Permanent Magnet Syncronous Machine

The phase voltage $\bar{V}_{an}$ of a PMSG can be expressed as follows:

$$(3.13) \qquad\qquad \bar{V}_{an} = \bar{E}_a - \bar{I}_a(jX_s - R_s) \qquad\qquad \text{[V]}$$

where X_s is the stator reactance, R_s is the stator resistance and I_a is the phase-a stator current.

The electromotive force E of the PMSG is defined as shown in Equation (3.14)

$$(3.14) \qquad\qquad E = k \cdot \omega_m \qquad\qquad \text{[V]}$$

where λ_{pm} is the constant of the generator.

If the stator resistance is neglected and the stator reactance is expressed as $X_s = L \cdot w_e$. The absolute value of the electromotive force of the generator from Equation 3.13 is defined as follows (3.15):

$$(3.15) \qquad\qquad E^2 = V_{an}{}^2 + (I_a L_s \omega_e)^2 \qquad\qquad \text{[-]}$$

The relation between the electrical and the angular speed is $\omega_e = \frac{\omega_m}{pp}$, where pp is the number of pole pairs of the rotor of the PMSG. From (3.15) the current is isolated and it results in (3.16)

$$(3.16) \qquad\qquad I_a = \frac{pp\sqrt{(\lambda_{pm}\omega_m)^2 - V_{an}{}^2}}{L_s \omega_m} \qquad\qquad \text{[V]}$$

Equation 3.16 gives the relation between the phase current of the machine with the mechanical speed of the rotor and the phase voltage. In the same way the voltage after the rectifier can be expressed as in Equation 3.17

(3.17)
$$V_{DC} = \frac{3\sqrt{6}}{\pi} w_m \sqrt{\lambda_{pm}^2 - \left(\frac{I_{DC}\sqrt{6}L_s}{\pi}\right)^2} \qquad \text{[A]}$$

The power at the output of the stator is given in Equation 3.18 which is the same after the three phase rectifier if it is considered ideal.

(3.18)
$$P = 3 \cdot V_{an} \cdot I_a = V_{DC} I_{DC} \qquad \text{[W]}$$

where V_{DC} and I_{DC} are the rectifier output peak voltage and current values.

The relation between the phase voltage, V_{an} and the output voltage of the rectifier, V_{DC} is defined in Equation 3.19 [10].

(3.19)
$$V_{DC} = \frac{3}{\pi}\sqrt{6}V_{an} \qquad \text{[V]}$$

Equation 3.20 defines the value of the DC current output of the 3-phase rectifier depending on the phase current of the stator of the PMSG [10].

(3.20)
$$I_{DC} = \frac{\pi}{\sqrt{6}}I_a \qquad \text{[A]}$$

From Equation 3.16, 3.18, 3.19 and 3.20, Equation 3.21 is derived. This equation represents the power produced after the rectifier depending on the DC-Voltage and the rotor speed.

(3.21)
$$P = \frac{\pi p p V_{DC}}{\sqrt{6}L_s\omega_m}\sqrt{(\lambda_{pm}\omega_m)^2 - \left(\frac{\pi}{3\sqrt{6}}V_{DC}\right)^2} \qquad \text{[W]}$$

As the term inside the square root must be positive, it yields:

(3.22)
$$\omega_m \geq \frac{\pi}{3\sqrt{6}\lambda_{pm}}V_{DC} \qquad \text{[rad/s]}$$

Equation 3.23 gives the minimum speed for the PMSG for starting to generate energy. As shown in Equation 3.23 the DC bus voltage defines the cut-in speed of the PSMG.

(3.23)
$$\omega_{mo} = \frac{\pi}{3\sqrt{6}\lambda_{pm}}V_{DC} \qquad \text{[rads]}$$

Figure 3.6 shows various power curves varying the mechanical speed for different fixed voltages. In here, it is shown that as higher the DC voltage as higher is the cut-in speed of the PMSG.

In Figure 3.7 several curves of the power output of the rectifier as the DC voltage increases are shown, but in this case the mechanical speed is fixed for each curve. It is possible to see that there is only one DC voltage value in which the PMSG delivers the maximum power.
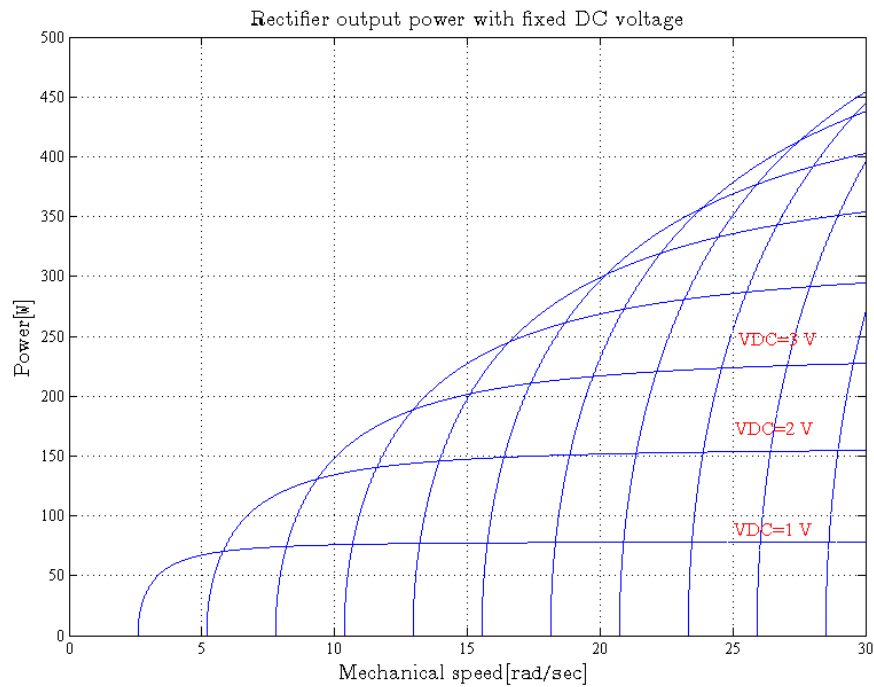
Figure 3.6. Rectifier power output with different fixed rotor mechanical speed and varying the DC output voltage
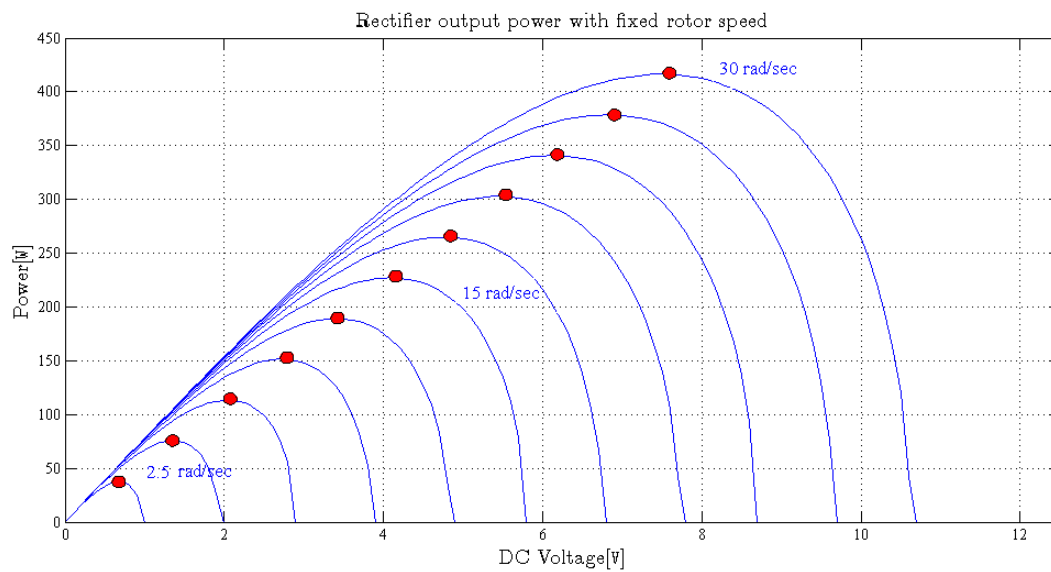
Figure 3.7. Rectifier DC power output with different fixed DC voltages and varying the rotor angular speed w_m.

If it is desired to convert energy at low wind speeds, as shown in Figure (3.6) the DC bus voltage should be low. If on the other hand, maximum power is required for high wind speeds, the DC voltage should be high.

Thereby, a DC/DC converter it is required to control the output voltage of the rectifier and to fix the output voltage of the system. By doing this, maximum power at any wind speed can be achieved.

3.3 Maximum Power Point Tracking

There are several methods to track the maximum power point of WG systems.

Figure (3.8) shows a common MPPT schematic diagram where the optimal power-rotational speed curve characteristic is usually saved in the DSP control unit.The rotational speed of the generator is measured and the corresponding optimal curve is compared with the power delivered by the power converter. The control unit generates the control signal according to this error [7].
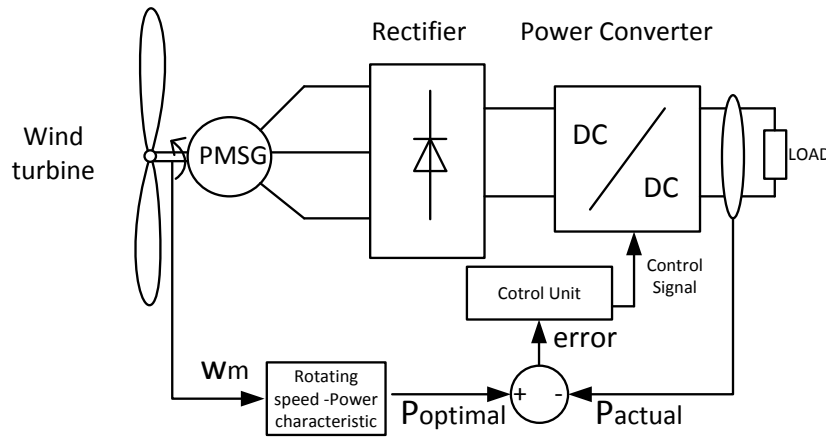
Figure 3.8. Maximum power point control system method using the rotor speed and the output power of the DC/DC converter

Figure (3.9) shows another possible maximum power point tracking schematic diagram. In here the wind speed is measured, and having the tip spit ratio of the wind turbine, the optimal rotational speed is calculated and compared with the one measured by a tachometer. The error signal is analysed by the control unit which generates the control signal for the power converter and the optimal rotational speed can be tracked.

The need of a tachometer in both previous methods and even a anemometer in the last one are need for tracking the maximum power point. Look-up tables with wind reference values and C_p coefficients depending on the tip spit ratio λ are also needed.

Due to the lack of a reliable anemometer, a tachometer and enough wind information in this project a simpler method will be used. Figure 3.10 shows the schematic diagram of the control system implemented, where the output voltage and current of the rectifier are read. The control unit processes these values and generates the control signal according to the MPPT algorithm.

In Equation 3.4 the mechanical power depends on the power coefficient and the wind speed. Figure 3.11 shows power coefficient- tip spit ratio curve for a wind turbine. Each wind turbine has its own power coefficient curve.

The tip spit ratio depends on the rotational speed and the wind speed $\lambda(u_w, w_m)$, and at the same time the coefficient of performance depends on the tip spit ratio. Thereby, Equation 3.4 can be written as follows (3.24)
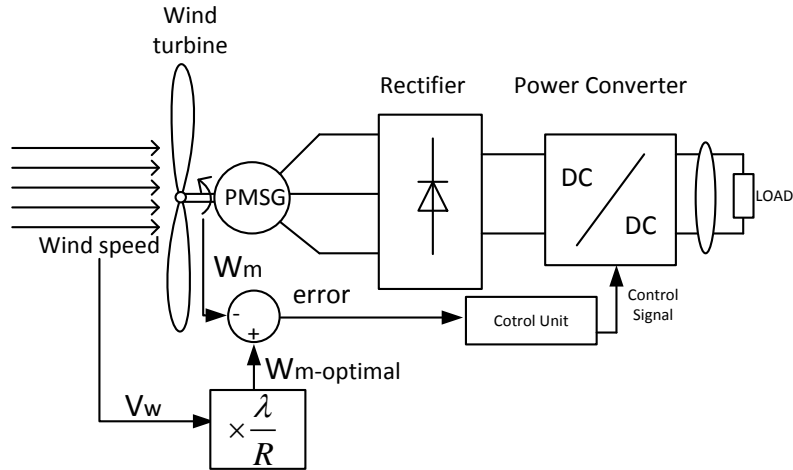
Figure 3.9. Maximum power point control system method using the wind speed and the rotor speed.
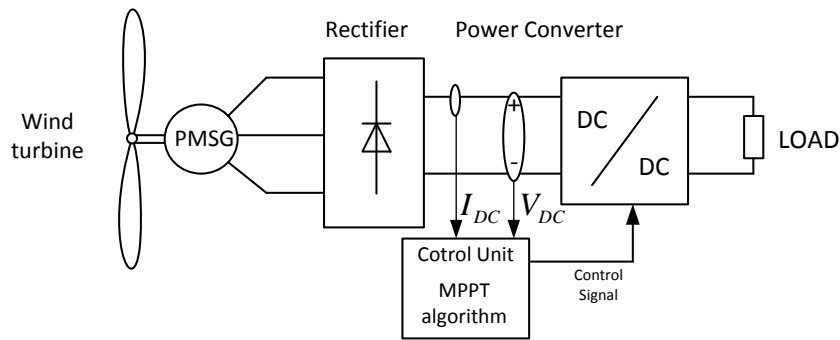

Figure 3.10. Maximum power point control system method using the output voltage and current of the 3-phase rectifier.
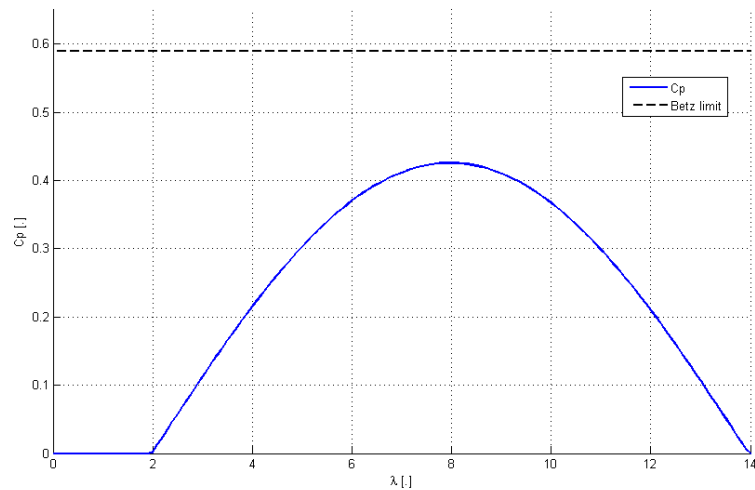
Figure 3.11. Power coefficient C_p versus tip spit ratio λ [9].

$$(3.24) \qquad P_m = C_p(w_m, u_w)v_w{}^3(\frac{1}{2}\rho \cdot A \cdot d) \qquad \text{[W]}$$

From Equation 3.24various power- mechanical speed for different fixed wind speeds can be plotted as shown in Figure 3.12. On each wind speed value, there is only one mechanical speed where the power is maximum.
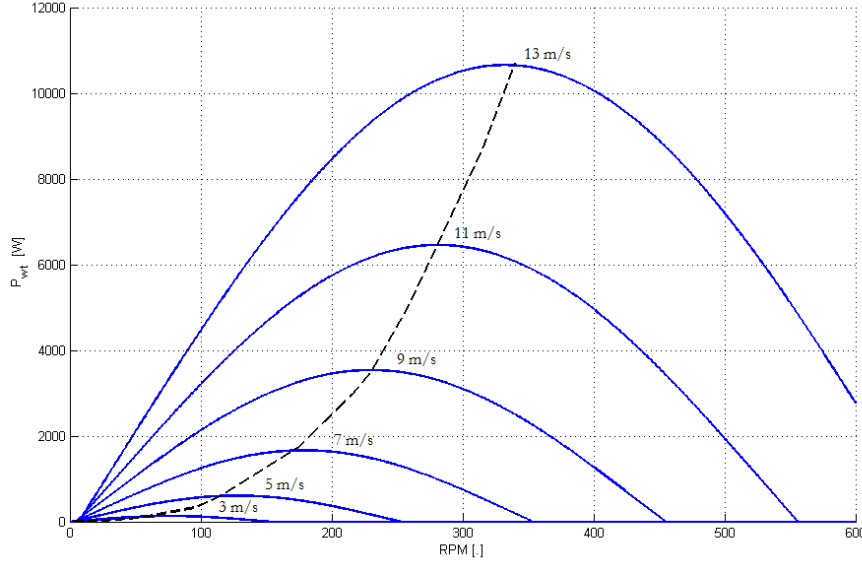
Figure 3.12. Power-mechanical speed curve for different wind speeds [9].

Equation (3.25) shows the torque equation where it only depends on the wind speed and the mechanical speed:

$$(3.25) \qquad T_m = \frac{C_p(w_m, u_w)v_w{}^3(\frac{1}{2}\rho \cdot A \cdot d)}{w_m} \qquad \text{[Nm]}$$

In the same way, various torque-mechanical speed curves can be plotted as shown in Figure 3.13. It is obvious that for maximum power higher speed is needed whereas for maximum torque the speed must be lower. In the plot, the maximum torque curve rises for different wind speeds with almost constant speed, but for maximum power the speed increases together with the wind speed.

As shown in Figure 3.10 a DC/DC converter is needed to track the maximum power point of the generator at any speed. The control unit processes the power output of the rectifier and generates a duty signal for the DC/DC converter so the PMSG works under the desired condition.
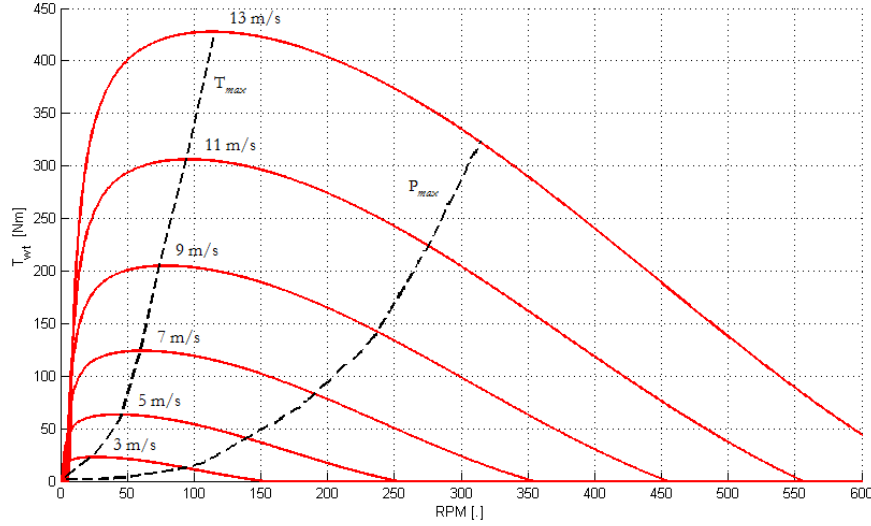
The algorithm used to track the maximum power point is explained below:

From Figure 3.12 it can be observed that at the point of maximum power, the variation of power with respect to the rotor mechanical speed is zero (3.26):

$$(3.26) \qquad \frac{dP}{dt} = 0 \qquad \text{[-]}$$

By applying the chain rule $(\frac{dy}{dx} = \frac{dy}{du}\frac{du}{dx})$ the follow equation can be stated (3.27) :

$$(3.27) \qquad \frac{dP}{dw_m} = \frac{dP}{dD}\frac{dD}{dV_{DC}}\frac{dV_{DC}}{dw_e}\frac{dw_e}{dw_m} = 0 \qquad \text{[-]}$$

Figure 3.13. Torque-mechanical speed curve characteristic for different wind speeds [9].

Each derivative is calculated independently below.

The V_{DC} is the voltage after the rectifier. If the DC/DC converter connected at the output is a Step-up converter, the relation between the input voltage V_{DC} , the output voltage(in this case is the battery level) and the duty cycle D is shown in Equation 3.28. The derivative of the duty cycle D with respect the DC voltage V_{DC} is shown in (3.29)

$$(3.28) \qquad\qquad V_o = \frac{V_{DC}}{(1-D)} \rightarrow D = 1 - \frac{V_{DC}}{V_o} \qquad\qquad [-]$$

$$(3.29) \qquad\qquad \frac{dD}{dV_{DC}} = -\frac{1}{Vo} \neq 0 \qquad\qquad [-]$$

The design of the MPPT algorithm proposed is being explained for the case of a Step-Up DC/DC converter. However, the same tracking method can be applied to other DC/DC converter topology by using the same procedure but using the proper converter relation and its derivative, as shown in Equation 3.30 for the Buck-Boost converter example:

$$(3.30) \qquad\qquad V_{DC} = V_o \frac{(1-D)}{D} \rightarrow \frac{dV_{in}}{dD} = -\frac{1}{D^2} \qquad\qquad [-]$$

In Equation 3.17 it can be observed that the derivative of V_{DC} with respect the angular speed w_m is not zero (3.31):

$$(3.31) \qquad\qquad \frac{dV_{DC}}{dw_e} > 0 \qquad\qquad [-]$$

The relation between the mechanical speed w_m and the electrical speed w_e is $w_e = pp \cdot w_m$ where pp is the machine pole pairs. Then the derivative can not be zero (3.32).

$$(3.32) \qquad\qquad \frac{dw_e}{dw_m} = pp > 0 \qquad\qquad [-]$$

It has been proved that from Equation 3.33, the only parameter which makes to fulfil the equation is $\frac{dP}{dD}$.

$$\frac{dP}{dw_m} = \frac{dP}{dD} = 0 \tag{3.33}$$ [-]

This proves that there is a value of the duty cycle D which makes the function $P(D)$ to converges to the maximum power point at a certain wind speed v_w.

The voltage after the rectifier if a Step-up converter is connected and considered the output voltage as the battery voltage level V_{batt} is defined as (3.34) :

$$V_{DC} = (1-D)V_{batt} \tag{3.34}$$ [V]

Equation 3.35 results from combining (3.21) and (3.34)

$$P = \frac{\pi pp(1-D)V_{batt}}{\sqrt{6}L_s\omega_m}\sqrt{(k\omega_m)^2 - (\frac{\pi}{3\sqrt{6}}(1-D)V_{batt})^2} \tag{3.35}$$ [W]

Plotting Equation 3.29 varying the duty cycle D from 0 to 1 for and a battery voltage level of $V_{batt} = 14.5$ Figure 3.14 is obtained. In here, two power curves are plotted, for $w_m = 20$ rad/s and $w_m = 30$rad/s.
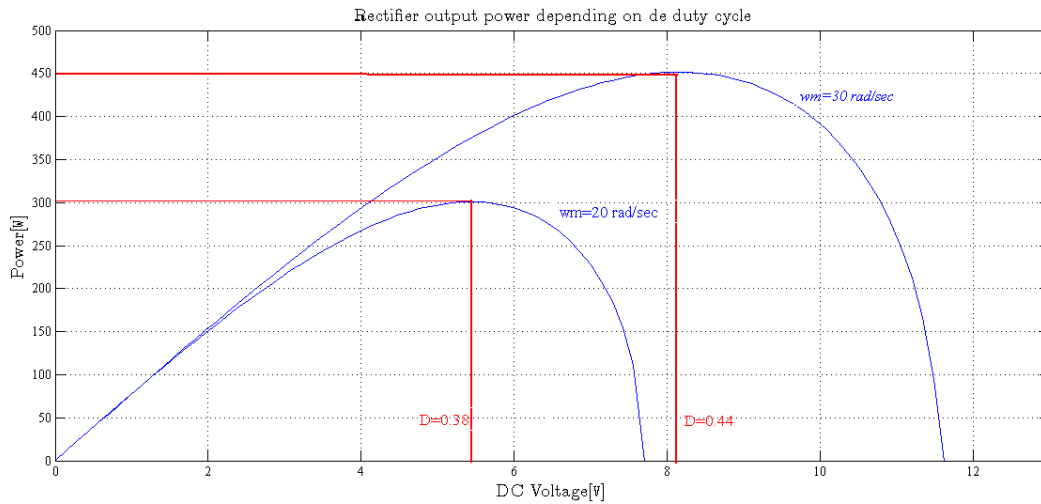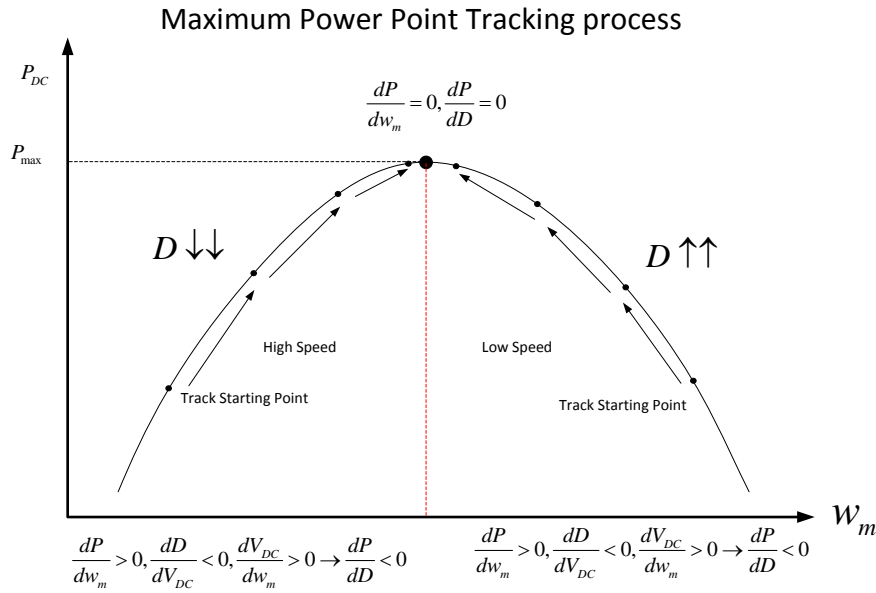

Figure 3.14. Power rectified generated by the PMSG varying the duty cycle from 0 to 1 for $w_m = 20$rad/s and $w_m = 30$rad/s. The X-axis represents the DC voltage after the rectifier which is $V_{DC} = (1-D)V_{batt}$

As pointed in the graph, when the $w_m = 20$rad/s the maximum power point occurs when the duty cycle is $D = 0.38$ whereas when the $w_m = 30$rad/s, $D = 0.44$ for maximum power. Thereby, Figure 3.14 proves what stated before, for tracking the maximum power point it is required to find the specific duty cycle at a each mechanical speed.

The maximum power point tracking process is showed in Figure 3.15. When the starting point is on the low speed side of the curve, the system must increase the duty cycle until the desired point is reached. On the other hand, when the starting point is on the high speed side, the duty cycle is increased so the speed is reduced and the MPP is tracked.

Figure 3.15 content (labels):

Maximum Power Point Tracking process

P_{DC}

$\frac{dP}{dw_m}=0, \frac{dP}{dD}=0$

P_{max}

$D \downarrow\downarrow$

$D \uparrow\uparrow$

High Speed

Low Speed

Track Starting Point

Track Starting Point

w_m

$\frac{dP}{dw_m}>0, \frac{dD}{dV_{DC}}<0, \frac{dV_{DC}}{dw_m}>0 \rightarrow \frac{dP}{dD}<0$

$\frac{dP}{dw_m}>0, \frac{dD}{dV_{DC}}<0, \frac{dV_{DC}}{dw_m}>0 \rightarrow \frac{dP}{dD}<0$

Figure 3.15. Maximum power point tracking algorithm designed for the Wind turbine system to work under the most optimum condition.

On the left part of the graph, when reducing the value of the duty cycle the mechanical speed is reduced and the power increases until it reaches the MPPT

When the system is working on the right part of the graph, if the duty cycle increases the mechanical speed is reduced and the power is increased until the MPPT is reached.

Figure 3.16 shows the algorithm for tracking the maximum power point for any wind speed. It consist on perturbing the system by increasing or decreasing the duty cycle and in the next cycle evaluate if the power has increased or decreased.

If the power and the duty cycle has increased means that the system is on the right side of the power-mechanical speed curve of Figure 3.15. Then, as the perturbation is on the right path, the duty cycle must continue increasing.
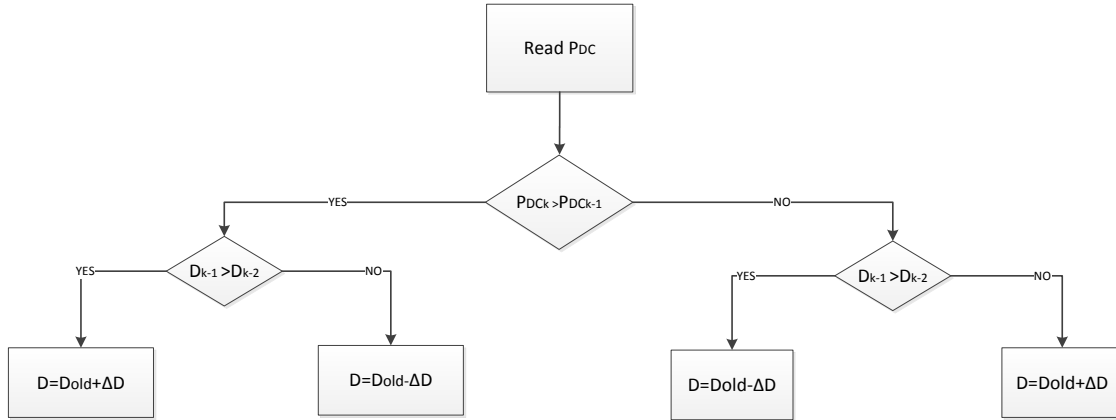
If the power has increased and the duty cycle decreased means that the system is on the left side of the curve. As the case before it is the right way so the duty cycle must keep decreasing.

When the power is lower than the previous one, it means that the perturbation is not proper and its sign must be changed to find the right path.
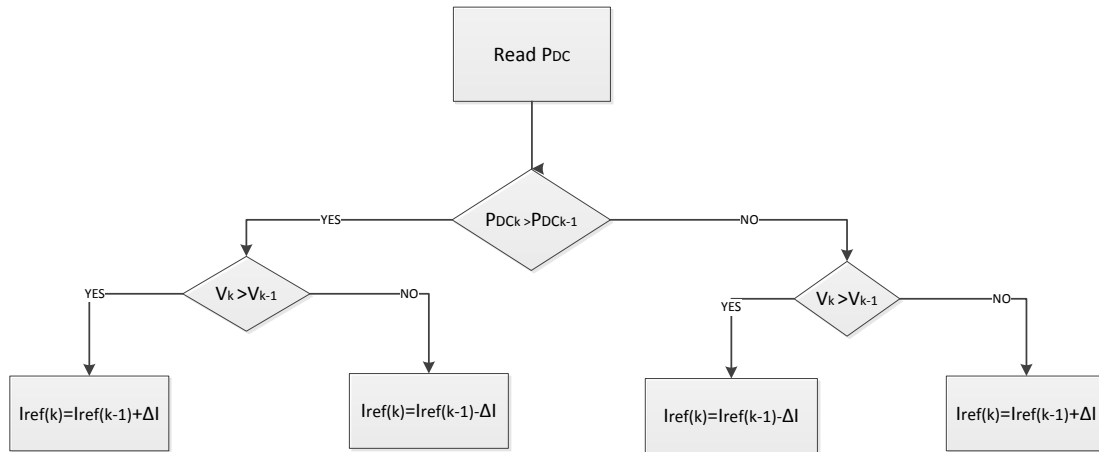
However, this algorithm must be improved because there is no control of the current and it could rise to a certain point in which it can damage the whole system. As the voltage is directly dependent on the duty cycle, the algorithm showed in the schematic diagram from Figure 3.16 is modified so the parameter to track is the reference current instead of the duty cycle. Thanks to this, the reference current can be limited to a certain desired value so the system is protected and the performance of the MPPT algorithm performs as previously explained.

Figure 3.17 shows the improved MPPT algorithm schematic diagram in which the perturbation is done over a reference current depending on the change of power and voltage at the input of the DC/DC converter. It must be noticed that the sign of the perturbation has changed due to the fact that when the duty cycle increases, the voltage decreases and vice-versa.

The new MPPT algorithm generates a reference current which is compared to the current value of the current, I_{DC}. The error signal must be conditioned so it can be compared to the triangular control

Read P$_{DC}$

P$_{DCk}$ >P$_{DCk-1}$

YES   NO

D$_{k-1}$ >D$_{k-2}$ D$_{k-1}$ >D$_{k-2}$

YES   NO   YES   NO

D=D$_{old}$+ΔD   D=D$_{old}$-ΔD   D=D$_{old}$-ΔD   D=D$_{old}$+ΔD

Figure 3.16. Maximum power point tracking algorithm

Read P$_{DC}$

P$_{DCk}$ >P$_{DCk-1}$

YES   NO

V$_k$ >V$_{k-1}$ V$_k$ >V$_{k-1}$

YES   NO   YES   NO

Iref(k)=Iref(k-1)+ΔI   Iref(k)=Iref(k-1)-ΔI   Iref(k)=Iref(k-1)-ΔI   Iref(k)=Iref(k-1)+ΔI

Figure 3.17. The improved maximum power point tracking algorithm designed for controlling the current flowing through the system apart from its MPPT characteristic [23].

signal , V_{tri} and the PWM signal to switch the MOSFET of the DC/DC converter is generated. Figure 3.18 shows a sketch of this process.

In this Chapter 3, first a brief explanation of the wind energy theory has been given. The principle of working of the Permanent Magnet Syncronous Generator connected to a three phase rectifier has been explained. Finally, different MPPT methods for wind power generation systems were presented and the one selected for this purpose has been studied.

3.4 Verification of the Wind turbine power generation system

In this section, simulations results of the Wind power generation together with the control system and charge controller will be studied.

Figure 3.19 shows the simulation schematic diagram designed for this project. The model is formed by the following blocks: Vertical Axis Wind turbine, PMSG and rectifier, battery, load and MPPT control system.

The parameters used for both the $PMSG\&Rectifier$ and VAWT blocks are shown in Table 3.1:
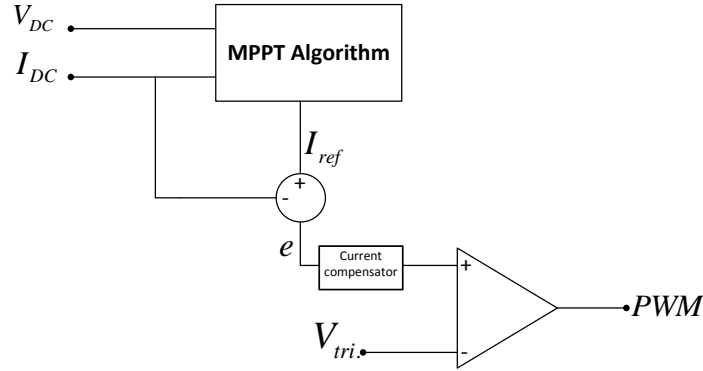
Figure 3.18. Switching PWM signal conditioning circuit for the MPPT tracking process proposed [23].
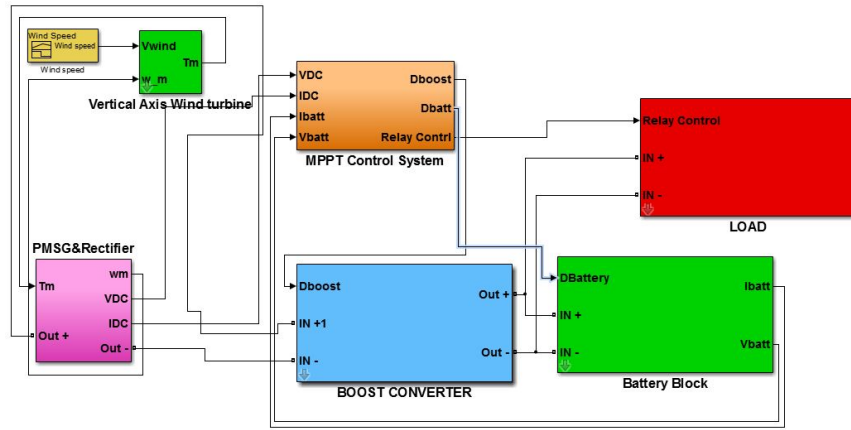

Figure 3.19. Simulation of the Wind turbine system designed for controlling batteries

Table 3.1. Wind turbine and PMSG parameters used for the simulations

Parameter	Value
Height of the wind turbine(H)	3 m
Diameter(D)	0.85 m
Stator resistances(R_s)	0.425Ω
Armature Inductance(L_s)	0.016180715H
Permanent magnet flux linkage(λ_{pm})	0.165Wb
Number of pole pairs	6

It has been used the PMSG block from the library SimPowerSystems of SIMULINK, connected to a three-phase rectifier. The Vertical Axis Wind turbine block has been modelled following the C_p-λ relation from [11] to study the system under more realistic environment. Figure 3.20 shows the coefficient of power (C_p) versus the tip spit ratio(λ) for three different types of wind turbine. The performance curve for the combined blade(CT Darrieus-Savonius) is the one used for this simulation.

The load block is formed by a 12Ω resistance and a relay to control the discharge of the battery. The battery block is formed by the SimPowerSystems battery block, a MOSFET to control the battery current and a resistance of 0.1Ω in series to reduce the spikes produced by the switching current. The switching frequency for the battery MOSFET control is 250Hz.
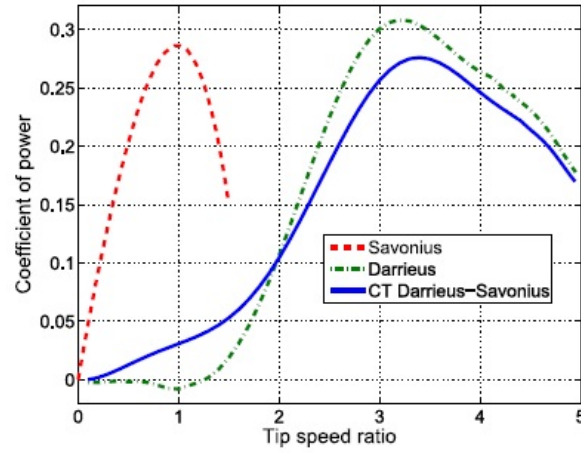
Figure 3.20. Coefficient of performance(C_p) versus the tip spit ratio (λ).

Simulation results are shown below. Figure 3.21 on the top the wind speed input for the system is shown. Wind speed goes first from $v_w = 0$m/s to $v_w = 6$m/s. It is maintained constant at $v_w = 6$m/s during 0.05s and then it increases to $v_w = 10$m/s. In this wind speed change the performance of the system can be studied. Figure 3.21 on the bottom, the mechanical speed of the machine is shown.
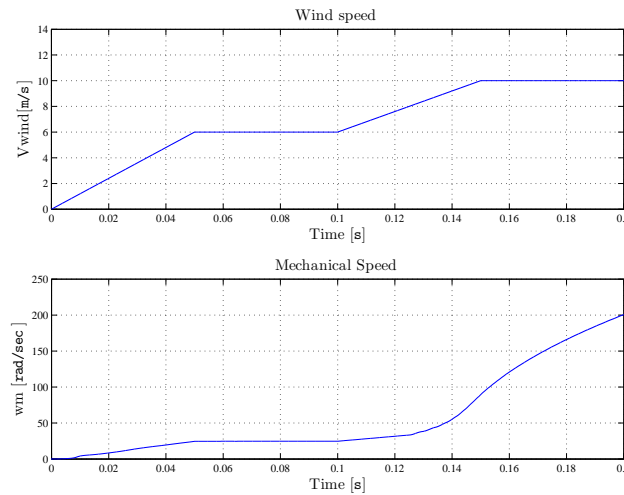

Figure 3.21. System input wind speed waveform and mechanical speed of the machine

Figure 3.22 shows the mechanical output power of the generator. From 0 sec to 0.01 sec the mechanical output is zero and it starts to rice once the power produced is greater enough to compensate the internal power losses of the generator. At this point the wind turbine starts to rotate and to produce power. It reaches a mechanical output power of 200W when the speed is 6ms. The nominal power of the machine is reached when the wind speed is over 10ms.

Figure 3.23 shows the PMSG stator phase voltages and rectifier output voltage. In Figure 3.23 the stator phase current and rectifier current are shown.
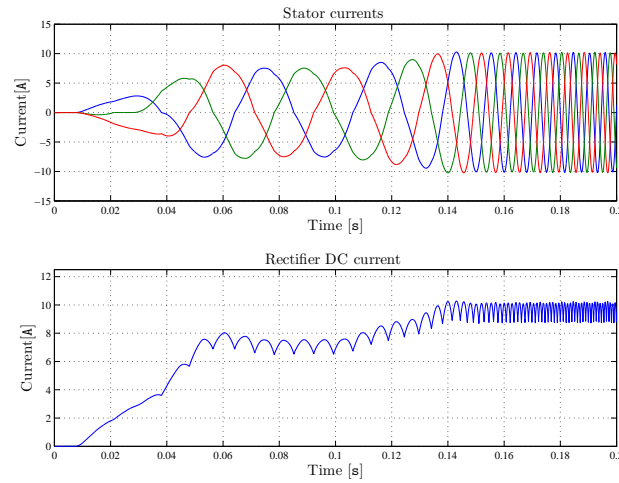
Finally, in Figure 3.25 the rectifier output current is plotted together with the battery current. It switches with a duty cycle of 0.9 and 250Hz.
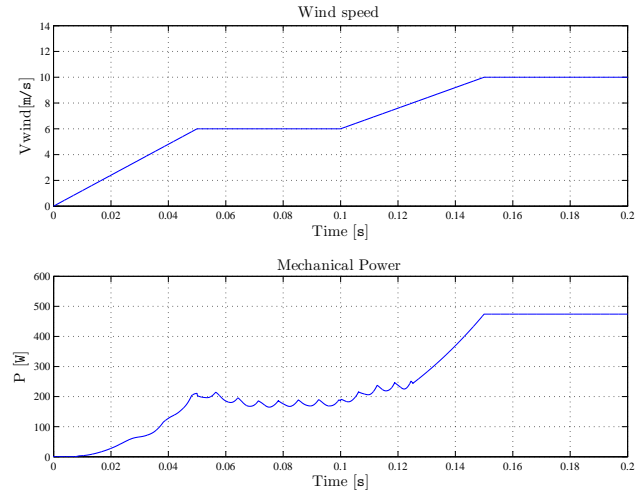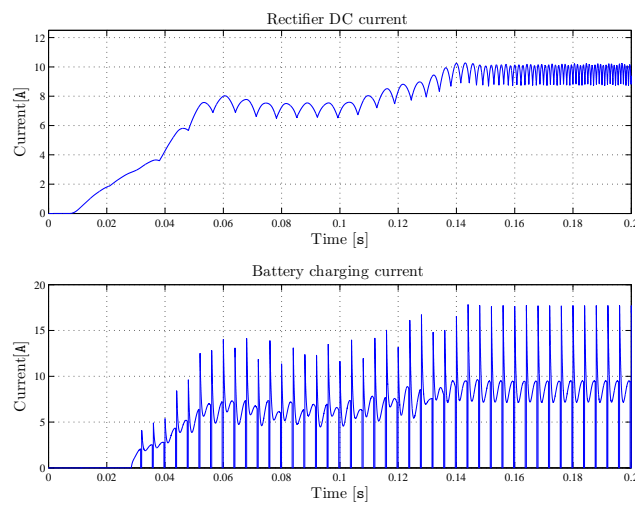
Figure 3.22. Wind speed input and mechanical power generated by the PMSG under the input wind speed range.
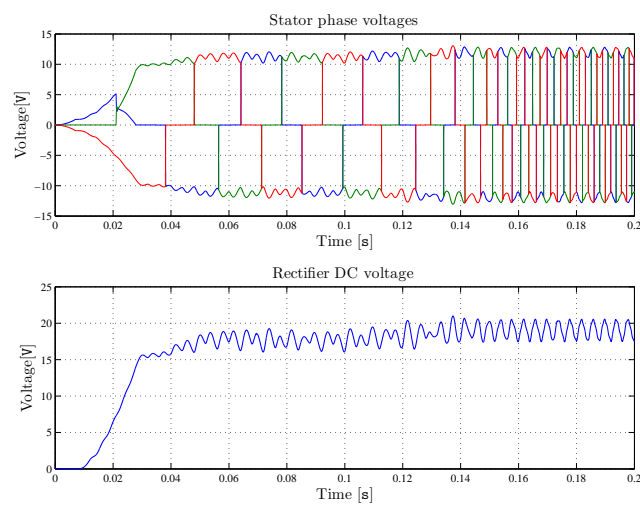
Figure 3.23. Wind speed input and PMSG stator phase voltages.

Figure 3.24. Wind speed input and stator phase currents.

Figure 3.25. DC current waveform after the rectifier, top and battery switching charge current, bottom.

Chapter 4

Photovoltaic systems and energy storage

In this chapter photovoltaic systems principle of working will be briefly studied in order to state the basic equations to build a real model of a photovoltaic model will be stated. Afterwards, the maximum power point tracking for photovoltaic systems will be explained.

4.1   Photovoltaic principles

Photons consist on electromagnetic radiation particles which form the sunlight. DC current is generated when solar cells, formed by semiconductor materials, are illuminated by photons.

An ideal photovoltaic cell can be represented by the equivalent circuit of Figure 4.1. It is formed by an ideal current source and a parallel real diode.
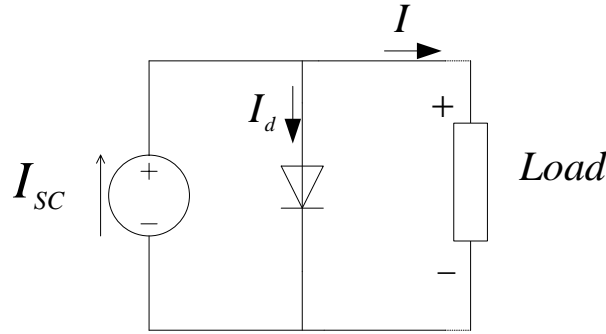
Figure 4.1. Equivalent circuit model for a photovoltaic cell.

By analysing the circuit shown before it is possible to get the electrical equations of a photovoltaic cell. The Shockley ideal diode equation given in (4.1) defines the I-V characteristic of a diode in both reverse and forward bias [25]:

$$(4.1) \qquad\qquad I_d = I_o(e^{\frac{qV}{kT}} - 1) \qquad\qquad \text{[A]}$$

where V is the voltage across the diode and therefore the voltage across the PV cell, q is the electron charge (q=1.602 · 10^{-19}C), k is Boltzmann constant k=1.381 · 10^{-23} J/K, T is the junction temperature and I_o is the reverse saturation current.

The output current of the the circuit showed in Figure (4.1) is defined as follows 4.2:

$$(4.2) \qquad\qquad I = I_{SC} - I_d \qquad\qquad \text{[A]}$$

Combining Equation 4.1 and 4.2, Equation 4.3 is obtained:

$$(4.3) \qquad\qquad I = I_{SC} - I_o(e^{\frac{qV}{kT}} - 1) \qquad\qquad \text{[A]}$$

By setting $I = 0$ in Equation 4.3 , the reverse saturation current can be calculated as follows (4.4):

$$(4.4) \qquad 0 = I_{SC} - I_o(e^{\frac{qV}{kT}} - 1) \rightarrow I_o = \frac{I_{SC}}{e^{\frac{qV}{kT}} - 1} \qquad [\text{-}]$$

The open circuit voltage is calculated by setting the short-circuit current previously defined in (4.3) and isolating the voltage (4.5).

$$(4.5) \qquad V_{OC} = \frac{kT}{q}\ln(\frac{I_{SC}}{I_o} + 1) \qquad [\text{V}]$$

Several cells must be connected in series to produce a high output voltage since one single cell only produce around 0.6 V. In addition, if it is desired to increase the current produced by the PV module, cells can be connected in parallel. The open circuit voltage across one single cell is then, $V_{OC,cell} = \frac{V_{OC}}{N_S}$ and the short-circuit current $I_{SC,cell} = \frac{V_{SC}}{N_P}$

The PV cell model studied before neglects few things: the parallel resistance, series resistance and recombination. Figure 4.2 shows a more accurate equivalent circuit of a photovoltaic cell.
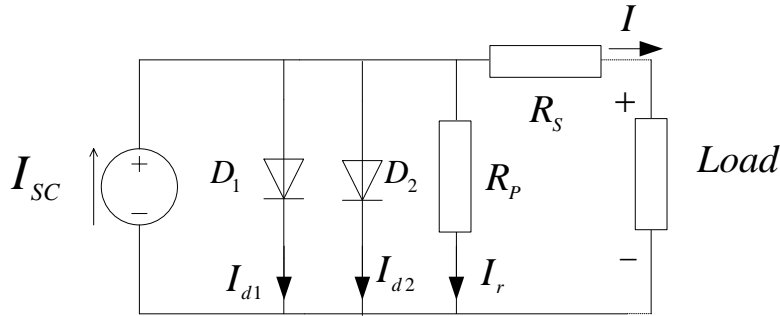
Figure 4.2. A more accurate equivalent circuit of a photovoltaic cell

The series resistance simulates the losses in the semiconductor material, the current collecting bus and the metal grid. The parallel resistance is equivalent to a small current leakage in the system. The effect of recombination in the depletion region of the PV cell produces a non-resistive current which can be understood as a second diode in parallel [4].

In order to improve the study of a photovoltaic module and therefore to obtain a better model, the parameters mentioned in the previous paragraph are included in Equation 4.3 which leads to Equation 4.6:

$$(4.6) \qquad I = I_{SC} - I_{o1}(e^{\frac{q(V+IR_S)}{kT}} - 1) - I_{o2}(e^{\frac{q(V+IR_S)}{kT}} - 1) - \frac{(V + IR_S)}{R_P} \qquad [\text{A}]$$

The short-circuit current for a certain temperature (T) is given in (4.7):

$$(4.7) \qquad I_{SC,T} = I_{SC}I_{SC,Tref}(1 + \alpha(T - T_{ref})) \qquad [\text{A}]$$

where the $I_{SC,Tref}$ is the short circuit current at reference temperature T_{ref} ($T_ref = 298K$) and α is the temperature coefficient of the I_{SC}.

Equation 4.8 shows the short-circuit current, $I_{SC,G}$ for a certain insolation value, G:

$$I_{SC,G} = G I_{SC,T} \qquad \text{[A]}$$

(4.8)

The reverse saturation current, can now be calculated for the reference temperature T_{ref} as shown in Equation 4.9:

$$I_{o,Tref} = \frac{I_{SC,Tref}}{e^{\frac{qV_{OC,cell}}{nkTref}} - 1} \qquad \text{[A]}$$

(4.9)

Having the reverse saturation current at T_{ref} from Equation 4.9, it can be calculated at the temperature of the module T as done in Equation 4.10:

$$I_{o,T} = (I_{o,Tref})[\frac{T}{T_{ref}}]^{\frac{3}{n}}(e^{-[\frac{qV_{OC,cell}}{nK}][\frac{T_{ref}}{T-1}]}) \qquad \text{[A]}$$

(4.10)

Equation 4.6 can be simplified by combining both diodes including the ideality factor, n. In addition R_P is neglected due to the small effect it produces[4]. By doing these simplifications Equation 4.11 is derived:

$$I_{PV} = I_{SC,G} - I_{o,T}(e^{\frac{q(V_{OC,cell}+IR_S)}{nkT}} - 1) \qquad \text{[A]}$$

(4.11)

For obtaining the value of the series resistance, X_V is calculated first.

$$X_V = I_{o,Tref}\frac{q}{nkT_{ref}}e^{\frac{qV_{OCcell}}{nKT_{ref}}} \qquad \text{[A]}$$

(4.12)

$$R_s = -\frac{dv}{di} - \frac{1}{X_V} \qquad \text{[A]}$$

(4.13)

The current output of a PV module can be then calculated by applying Newton's equation showed in Equation 4.14:

$$I_{PV_{k+1}} = I_{PV} - \frac{f(I_{PV})}{f'(I_{PV})} \qquad \text{[A]}$$

(4.14)

Equation 4.15 summarizes the three equations needed for using Newton's equation:

(4.15)
$$
\begin{aligned}
I_{PV} &= I_G - I_{o,T}(e^{\frac{(V_{PV,cell}+I_{PV}R_S)q}{nKT}} - 1) \\
f(I_{PV}) &= I_G - I_{PV} - I_{o,T}(e^{\frac{(V_{PV,cell}+I_{PV}R_S)q}{nKT}} - 1) \\
f'(I_{PV}) &= -1 - \frac{q}{nKT}I_{o,T}(e^{\frac{(V_{PV,cell}+I_{PV}R_S)q}{nKT}})
\end{aligned}
\qquad \text{[A]}
$$

where V_{PV} is the load voltage divided by the number of cells in series.

In order to ensure that the equation converges in all the results, previous Equation 4.15 is done five times in the model.

The power produced by a solar module is directly depending on the solar irradiation, cell temperature and the load impedance.

The temperature of the module affects the output voltage of the panel, for high temperatures it decreases. Regarding the insolation which the module is exposed, the current generated by the PV module will increase or decrease.

As both parameters previously mentioned are not constant and they result uncontrollable the power produced by the PV module is variable and unpredictable. The maximum power point (MPP) is a basic concept in solar systems, which defines the maximum power the PV panel can give to the system depending on solar irradiation level.

Figure (4.3) shows the effect of variation of the irradiation level over the I-V characteristic of a PV module. When increasing the irradiation, the output voltage is almost constant whereas the output current gets a lot higher.
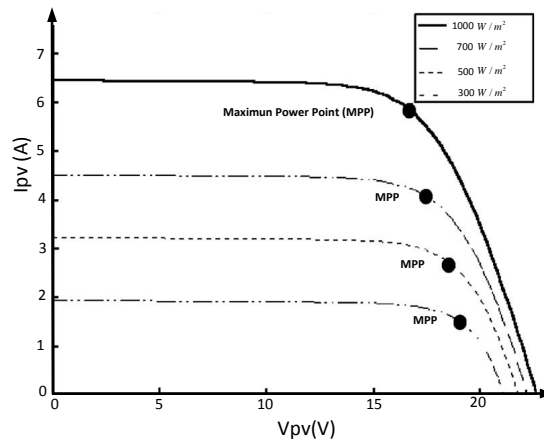
Figure 4.3. I-V curve characteristic curve from an ideal photovoltaic panel [20]

In Figure (4.4) the power-voltage curve of a photovoltaic module is plotted where the maximum power point for different values of insolation are highlighted.

As previously mentioned, the module temperature has an important effect on the power produced by the PV system. Figure 4.5 shows how the power of the system is affected by an increase of the temperature of the cells. For three different temperature values, the voltage changes. For lower temperatures the voltage gets higher and consequently MPP is higher than for high cell temperatures.

As it has been explained the weather conditions have an important effect on the power generated by the PV module. However, it is possible to control the power produced so it reaches its maximum possible at any case. It is important to mention that the PV module can be considered as a variable voltage source, depending on the load connected the current will be higher or lower. In case of having a battery connected as a load, it will will fix I-V behaviour of the PV module, which will not always be the MPP of the PV panel citemppt.

In Figure (4.6) a photovoltaic module ideal I-V characteristic is shown. In here , the battery voltage, and consequently the output voltage of the PV panel, will oscillate between 10.5 V and 14.5 V. Due to this fact the power point of the system will be far from its maximum in some cases.

By controlling the output voltage and current of the PV module with a DC/DC converter, it is
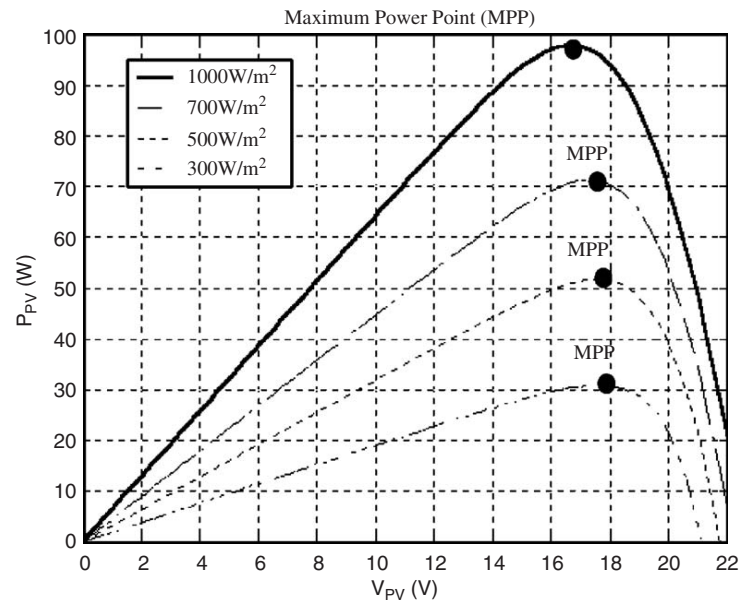
Figure 4.4. Power and Current characteristic from a photovoltaic module [20].
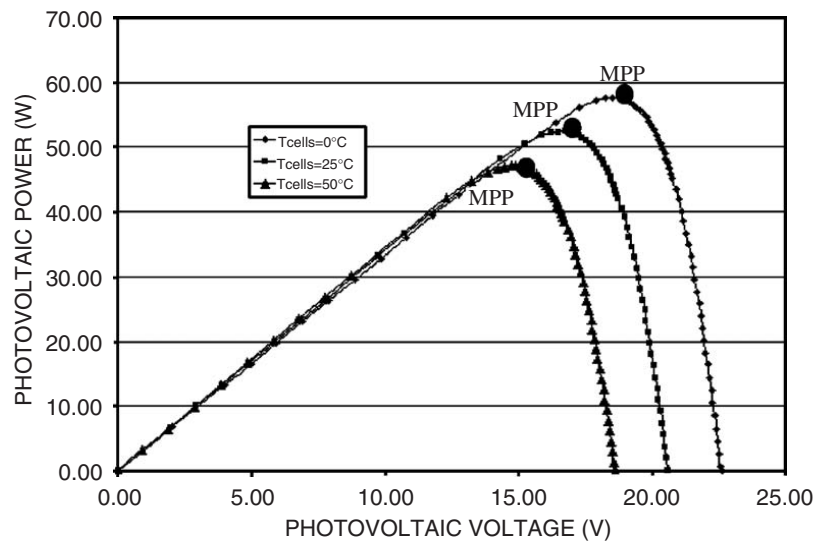

Figure 4.5. Characteristic curve of the power and voltage depending on the temperature of the PV module [20].
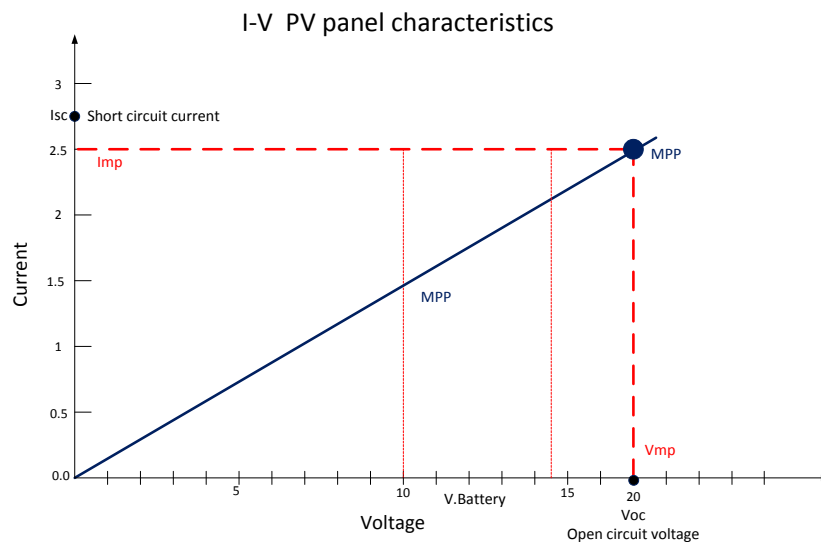

Figure 4.6. I-V 60 Watt 12 V PV panel characteristics

possible to make the photovoltaic system to work under the desired conditions of current and voltage and therefore the maximum possible power point can be tracked (this process is called Maximum Power Point Tracking, MPPT).

In this Section 4.1 a short explanation of the photovoltaic theory has been given as well as the effect of external and unpredictable conditions, as insolation and temperature, on the power produced by this generation systems. In the next section, the way to control the output power of the PV module will be explained.

4.2 Maximum Power Point Tracking

In this section the principle of working of Maximum Power Point Tracking(MPPT) charge controllers for PV applications will be explained.

Pulse width modulation DC/DC converters make possible to track the maximum power point of the module under certain conditions. This is called MPPT(Maximum Power Point Tracking MPPT control) technique which consist on adjusting the electrical working point of the module to maximize the power available [20].

Figure (4.7) shows a common schematic of MPPT charge controller. In here, the current and voltage output of the PV module is read and processed by a micro-controller, which will generate the control system tracking the maximum power point.
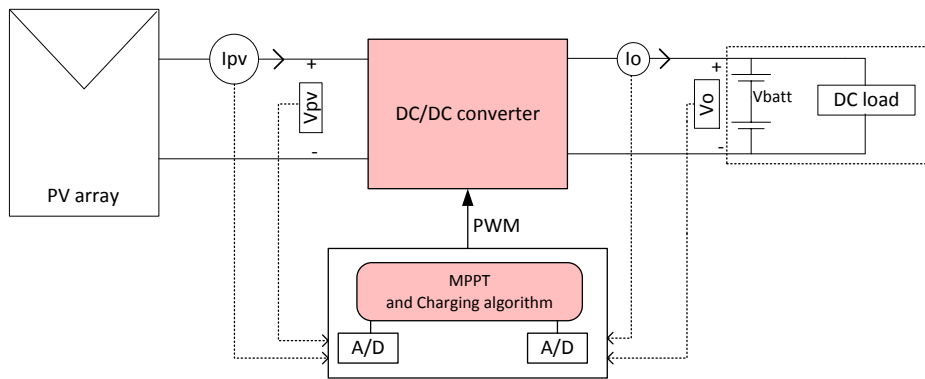
**Figure 4.7.** Charge controller schematic diagram

In a photovoltaic module there is only one point on the I-V curve characteristic where the power is maximum. By introducing DC/DC power converter between the PV system and the batteries make possible the system to work under its maximum power point.

Power Feedback method is a common MPPT topology which uses the power output of the module and uses it as a feedback input . Inside this topology, three different methods are widely used: Perturbation and Observation(P&), the incremental conductance(IncCOnd) and the hill climbing method(HC) [21].

Both the IncCond and the P&O regulates the photovoltaic module voltage to continuously track the optimal set point (V_{mp}). In Figure 4.4 it is obvious that for each maximum power point, the variation of power over a change in the output voltage is zero. These algorithm try to find the optimal voltage which makes $\frac{dP}{dV} = 0$ for any temperature or insolation.

On the other hand, the Hill climbing method consist on making a small variation on the duty ratio of the converter which will produce a perturbation on the module current and on the voltage. Figure

4.8 shows that being on the left part of the MPP an increase on the voltage causes and increase on the Power and vice-versa. However, if the system is working on the right part of the MPP the power increases when the voltage decreases.
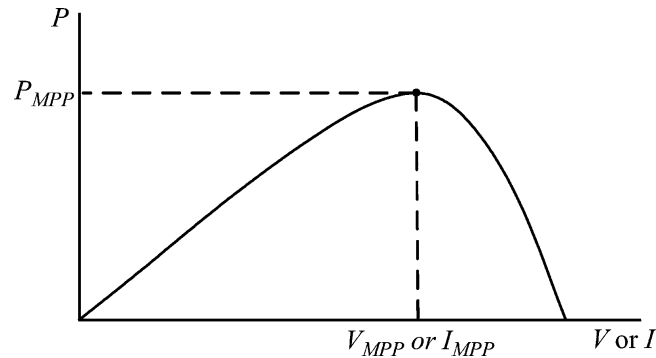
Figure 4.8. Power-voltage and current curve of a photovoltaic module [5].

This method consist on making a perturbation on the duty cycle and comparing the new power output with the feedback one. If the power has increased means that the perturbation is on the right way. If the power decreased the sign of the perturbation needs to be changed. Once the system has reached the MPPT it will oscillate around this point and the oscillation will depend on the perturbation set. For a small perturbation, the oscillation will be low but the system will take more time to reach the MPP. It is possible to set the algorithm to reduce the perturbation once the system is getting close to the MPP.

This algorithm is the same as the one used for tracking the MPP for the wind turbine. Figure 3.16 from Chapter 3.16 shows the flowchart diagram of this algorithm, implemented for this purpose.

It has been selected Hill Climbing method for the PV system due to its simplicity and the fact that it is not required to be periodically tuned and the converge speed can be adjusted by changing the value of the perturbation. The disadvantage of this algorithm is that it can fail under rapidly changing atmospheric conditions [5]. However sun irradiation it is usually constant in the location of the system used for this report.

The importance of a charge controller.

The MPPT control system is part of what is called charge controller. It can consist on either an analog circuit or a digital system(A DSP or a Microcontroller). The main and most important function of the charge controller apart from MPPT is to protect the batteries from the PV panels when they are over charged, and to protect them from the loads in case they are over discharged .

Charge controllers depending the battery voltage value measured regulates the current flowing into the battery, if it is higher or lower than the maximum or minimum voltage which can reduce the battery lifetime it will shut down the charging current coming from the PV module or the one given to the load.

In the next Section 4.3 lead-acid battery principle of working and charge algorithm will be presented. By introducing a DC/DC converter between the PV module and the battery, it is possible to considerably increase the lifetime of the battery.

4.3 Energy storage

Stand-alone renewable energy systems are not connected to the grid and they present the need of a storage system which stores the energy when the load does not fit the energy production. For situations when there is not enough energy produced they are needed to supply the load demand. In this section batteries for stand-alone PV system will be described and charge and discharge process

will be studied, as it is what concerns the most for the purpose of this report.Basic theory about lead-acid batteries is explained in Appendix A.

The battery capacity is commonly measured in ampere-hours(Ah), which is equal to 3600 As. The fundamental measure unit for energy storing systems is Coulombs(C) and the relation is 1 As = 1C which leads to 1 Ah=3600 C

The battery capacity is defined by three important factors which are : temperature, discharge rate and depth of discharge.

The rate of discharge determines the amount of energy that the battery can supply during a certain amount of time. It is usually defined as the relationship between the nominal capacity of the battery and the discharge or charge current. It is specified as C/XX where XX is the rate of discharge and C the capacity of the battery. For example Table (4.1) shows a manufacture discharge rate table of a nominal 12 V-105Ah battery. In here, five amperes represents a C/20 discharge rate for a 105 Ah battery. As seen in the table when the battery is discharged during twenty hours the capacity of the battery reaches its nominal value. However, the faster is the discharge rate the lower gets the battery capacity.

Table 4.1. Discharge rate of a common 12 V-105Ah battery[3].

Capacity(Ah)						
2-h rate	5-h rate	10-h rate	20-h rate	48-h rate	72 h rate	100-h rate
68	85	97	105	112	114	117

The depth of discharge(DOD) defines the percentage of energy delivered from the battery in relation with the energy when the battery is fully charged. This parameter is really important when working with Lead-Acid batteries due to the fact that the lifetime of the battery directly depends on the depth of discharge.

Figure Figure 4.9 shows the lifetime curve of a random battery given from the manufacturer. It shows the lifetime of the battery in number of cycles of charge and discharge depending on how is the depth of discharge. By looking at the curve it is possible to observe how the lifetime is reduced when increasing the DOD.

The state of discharge(SOC) is the ratio between the nominal capacity q_{max} and the actual capacity q as given in (4.16):

$$SOC = \frac{q}{q_{max}} \qquad [\text{V}]$$
(4.16)

Battery temperature

Battery temperature considerably affects the behaviour of the battery(mainly the voltage vs. SOC).It may be depressed arround 0.5 Vfrom the charge and discharge curves. The internal resistance is affected by the temperature of the cells, being higher for cooler temperatures. The voltage then increases when the cells are cold. However for temperatures lower than 0°C the ampere-hour curve is affected [14].
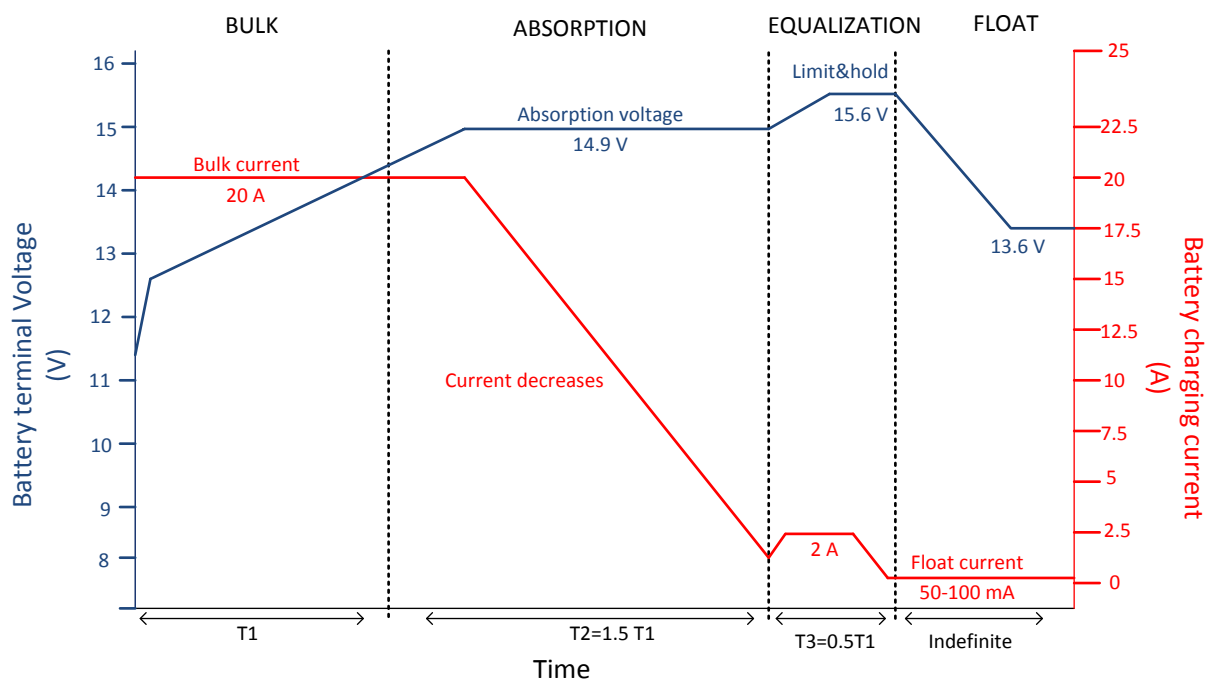
Battery Charging Process

When charging a battery there are four stages of charging: Bulk, Absorption, Equalization and Float. However it is not always required to apply the four stages, it depends on the type of battery and the charge controller. In Figure (4.10) a charge algorithm is shown for a 12 V lead-acid battery [19].
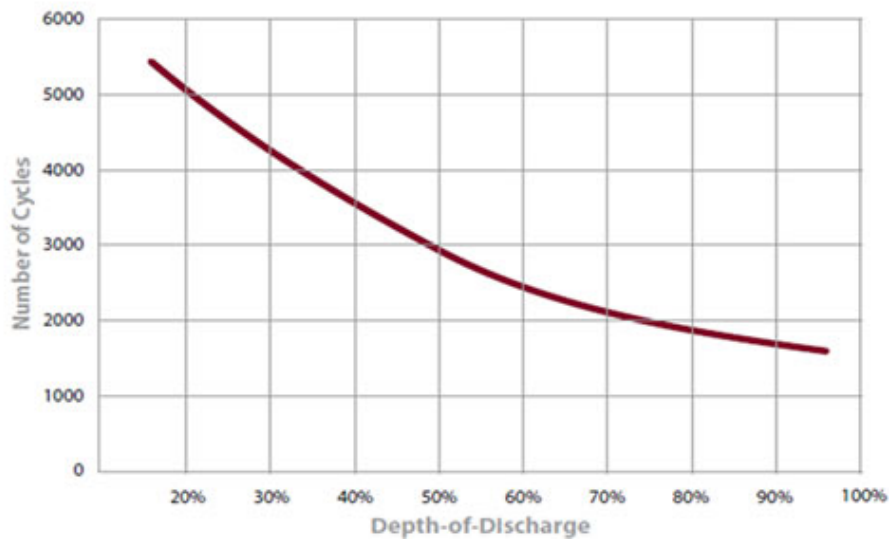
Figure 4.9. Lead-Acid battery lifetime graph depending on the depth of discharge and the number of charge and discharge cycles[3].

Figure 4.10. Four stages battery charging algorithm bulk, absorption,equalization and float [19].

The bulk charge mode occurs when the battery is fully discharged.In this stage the charge controller gives the maximum current it can supply and the voltage increases. As seen in the sketch of Figure (4.10) the current is held constant until the voltage reaches a certain level.

At this point, the charge controller dynamicaly reduces the current given to the battery which keeps drawing current until it is fully charged. This stage is called Absorption when the current is varying and the voltage is held constant.

Some charge controllers only uses this two essential stages to charge the battery. However, some battery manufacturers recommend to follow the next two stages.[19]

The equalization charge mode is used to end up the charge of the battery. As shown in in the sketch of Figure (4.10) the charger increases the voltage of the battery around 3 or 4 V and there is a rise in the current drawed by the battery until the battery is fully charged.

The last stage called Float,

Equalization Charge mode Once the battery is 95% charged, the Equalization stage is used to end up the charge of the battery. On this stage the battery charger gives to the battery 3 V or 4 V above the no load fully charged voltage. The battery will then try to draw as much as current as the charger can give. Then the battery charger will reduce the current and after a certain time it will jump to the next stage.

This stage is not essential in the charge algorithm, it depends on the battery manufacturer requirements [19].

Float Charge mode

It is also called storage or maintenance charge mode.

It consist on keeping the battery fully charged indefinitely. The charger gives a fixed voltage to the battery with a value slightly higher than the no load fully charged battery, typically between 13.2 to 13.6 V. The current is set to a small value or the controller is turned off [19].

4.3.1 Batteries charging process and load management

The battery charging and load management used on this project will be briefly explained.Figure (4.11) shows the schematic diagram between the DC/DC converter circuit and the batteries and load. In here, the battery voltage and current are read and signals for controlling the switches are generated.

Series-Interrupting,Pulse width Modulated Design

There are several techniques to control the battery charge management. In this report Pulse width modulated control has been chosen for several reasons: It Prevents the process of sulfation and it helps preventing the degradation of the battery plates, consequently it increases battery service life dramatically [17].

As shown in Figure (4.11) a semiconductor switching element is placed between the power generation system and the battery and is controlled by a PWM signal with a certain frequency. By controlling the width of the PWM control signal, it is possible to regulate the amount of current flowing into the battery. When the battery is discharged, the pulse is practically on all the time allowing the maximum possible current charge the battery. This case would correspond to the Bulk stage of the battery charging algorithm previously explained in (4.3) Once the battery has reached a certain voltage level, the Equalization stage starts where the current is dynamically reduced to end the battery charge process. The width of the PWM signal is reduced according to the voltage level of the battery.

In Section (4.3) four stages were introduced in the charge algorithm process. However, in this project only the fundamental stages, Bulk and Equalization are used due to simplification.
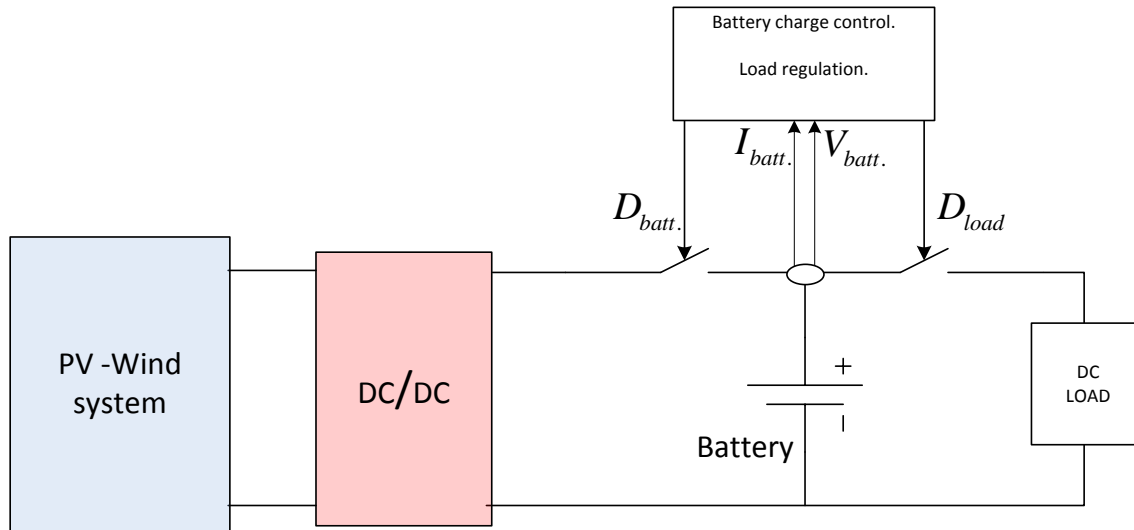
Figure 4.11. fdsafsd

When the battery reaches the fully charge voltage level specified by the manufacturer, a permanent OFF signal is given to the switch leaving the circuit in open circuit so no current flows into the battery.

It is important to mention that as faster is the charge and discharge of a battery, the higher becomes its stress, reducing its lifetime. However, renewable energies as wind is uncontrollable and unpredictable, being necessary to use all the energy produced. The manufacturer gives a recommendable the maximum charging current which usually varies between the 10-30 % of its nominal capacity.

Load management

In order to increase the lifetime of the battery it is really important to protect it from overdischarge. For doing this, a relay is connected between the battery and the load positive terminal. This relay will be active until the control unit reads a low level on the battery voltage.

When the load is disconnected from the battery, there is a phenomena called hysteresis, which makes the battery voltage to jump over its real value. Thereby, the system would reconnect the load again because the systems thinks the battery has been recharged, causing the battery to be overdischarged. By having a higher voltage level to reconnect the load, this problem is avoided.

In this chapter a brief review of photovoltaic theory has been done. The MPPT systems has been explained and the algorithm chosen for improving the behaviour of the PV system has been stated. It has also been explained principle of working for lead-acid batteries as well as the strategy for charging them, increasing their life time.

4.4 Verification of the photovoltaic power generation system

In this section the the photovoltaic power generation system will be studied in order to verify the behaviour of the Photovoltaic module model and the MPPT system implemented for this purpose.

The schematic diagram of the simulation done is shown in Figure 4.12. It consist on the PV module model built for this project(it can be found in the CD), a buck converter and a $12V - 105Ah$ battery block. The PV module parameters used are based on a common 60 Wpanel with V_{OC}=18Vand $I_{SC} = 3.3A$. The MPPT block is based on the maximum power point tracking algorithm explained in Chapter 4.
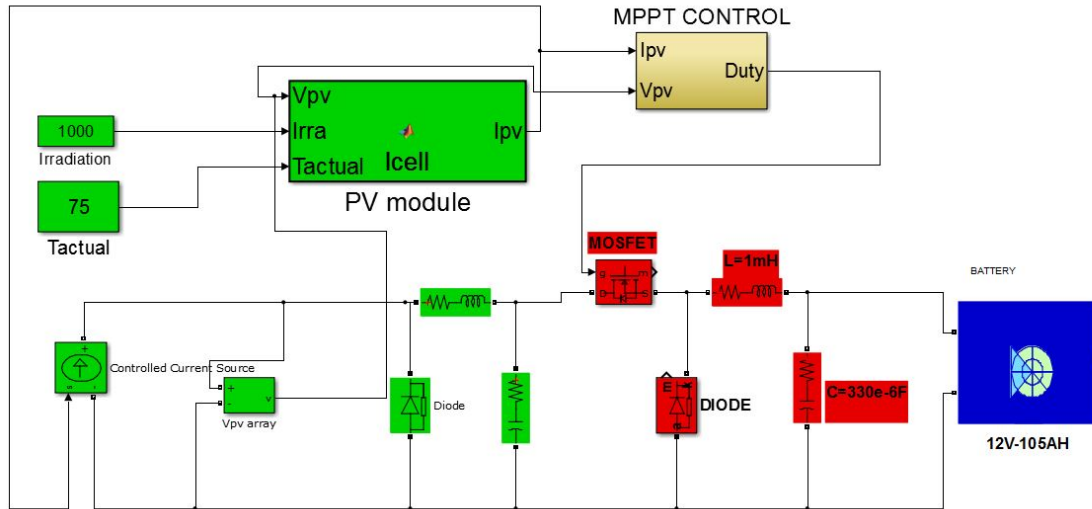
Figure 4.12. Simulation schematic of the MPPT controller designed for this purpose

In Figure 4.13 the system response of the MPPT algorithm block is showed. The insolation input is first $G = 0.5\text{kg/m}^2$, and after $0.4\,\text{sec}$ is increased to $G = 1\text{kg/m}^2$
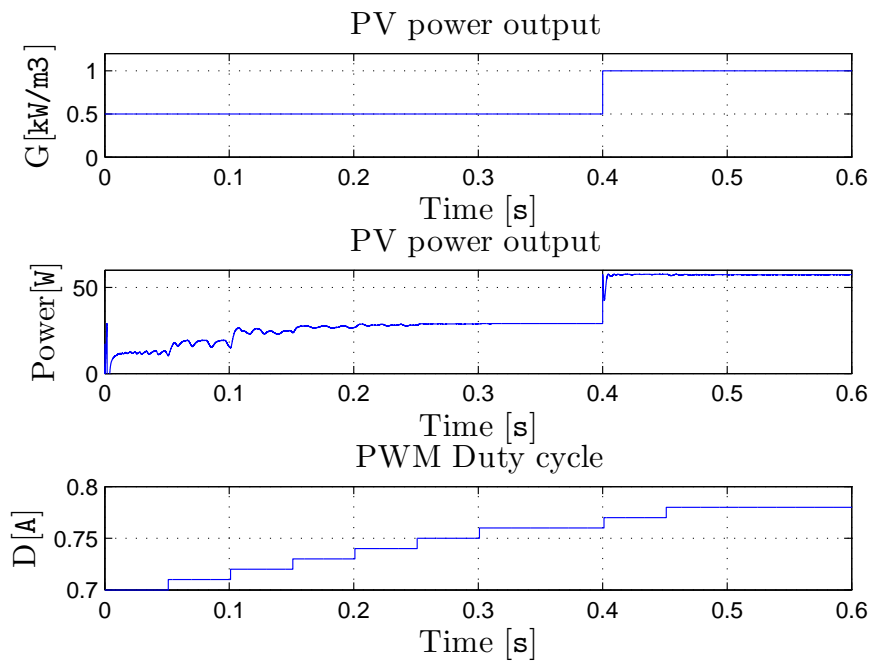
Figure 4.13. Maximum power point tracking response.

Chapter 5

Multiple Input DC converters

In this chapter Multiple Input Converters(MIC) will be introduced and different topologies will be exposed. The system selected for the purpose of this report will be analysed.

Solar and wind energy can be understood as two variable energy sources having different $V-I$ characteristic. Thereby, in order to combine both energy generation systems it is required that both of them have the same output voltage.

For doing this, what is usually done is that each voltage source is connected to a single DC/DC converter which fixes the output voltage to the desired one. Figure (5.1) shows the schematic diagram of both energy generation system voltages connected to two converters and the output connected in parallel to a load.

In this connection both voltage source will produce a stable output which will fed the power demanded by the load.
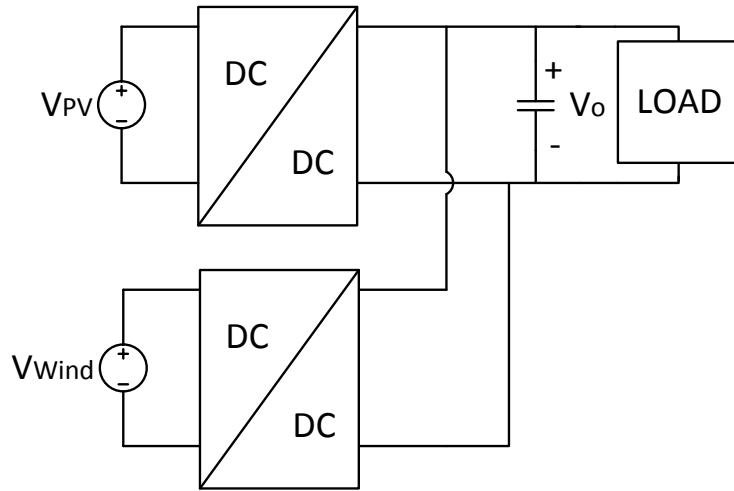
Figure 5.1. Solar and Wind hybrid system controlled with two DC/DC converters.

However, due to simplicity dual-input DC/DC converters are preferred for this applications. Where both voltage sources are connected to the same converter which generates a stable output voltage and supplies the load the energy produced by both systems. Figure (5.2) shows a general schematic a dual-input DC/DC converter.

Dual-input converters have some advantages against using independent DC/DC converters. The first one is the reduction of the number of the components used for the same purpose, which means smaller the space needed for the system,cost reduction and an increase in the efficiency of the system. In addition, MIC does not require synchronization for maximizing the output power of the converter depending on the load requirements [24].
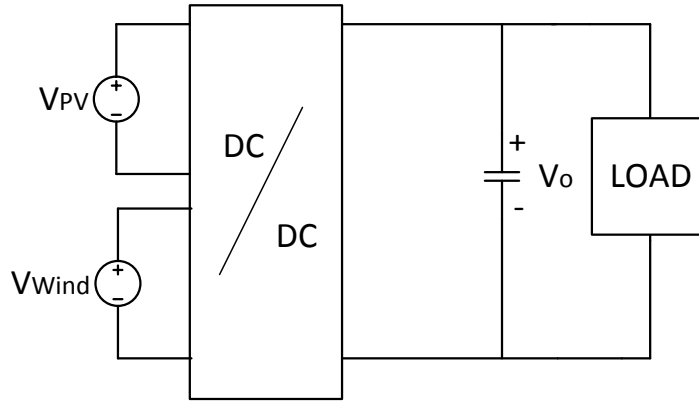
Figure 5.2. Solar and Wind hybrid system controlled by a dual-input DC/DC converter.

5.1 MIC Converter topologies

There has been proposed several isolated and non isolated topologies of multi-input converters in the last decade. Magnetically connected circuit(MCC) is the isolated MIC topology based on the use of transformers to achieve flux addition. However this topology is often undesirable because having a transformer make the system bulky, costly and less efficient [8].

Non isolated MIC topologies are also called ECC or electrically connected circuit which are based on combining various input power generation sources either in series or in parallel. This topology is much more atractive as it is transformless, low cost and its modular structure allows to connect several input sources [8]. ECC parallel connected presents an important disadvantage, only one of the different energy input can supply energy to the load at a time. Series connected MIC solves this problem, several input sources can be connected in series and supply energy to the load.

However, it should be denoted that most of the research done about MIC technology is based on single input DC/DC converter topology and have not been fully studied and completely synthesised [8].

Figure 5.4 shows an isolated MIC topology proposed in [8]. This MIC uses the concept of magnetic flux addition to step up the voltage from both input sources and supply energy simultaneously to the load.
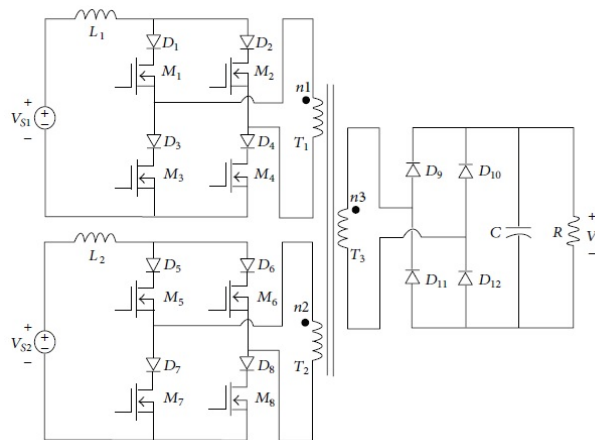
Figure 5.3. Multiple Input DC/DC converter based on magnetic flux activity.

Even though the isolation characteristic of this converter makes this topology attractive, it has not been considered for the purpose of this report, due its complexity and the needed of a transformer.

Figure 5.4 shows the two topologies considered for the purpose of this report. They are based on single input DC/DC converters. Both technologies present the following similar characteristics: They can supply power to the load individually or simultaneously and soft switching technology is feasible [24].

Figure 5.4(a) an sketch of the double input buck converter is shown. In Figure 5.4b, a multiple input converter with step-up characteristic is presented. In addition, it can behave as a buck-boost converter by changing the three possible control signals.
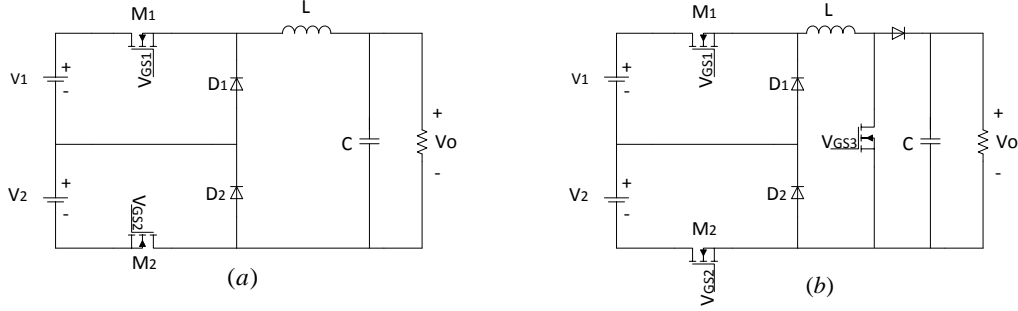
Figure 5.4. Three main topologies for multiple input DC/DC converters. In (*a*) a double input buck-boost converter, (*b*) a double input buck converter and (*c*) step-up double input DC/DC converter.

Figure 5.5 presents a topology which results from recombination of the previous topologies. By controlling the switches, it is possible to change the mode of operation of the converter in such a way that the system can be configured to work under buck-boost, buck or boost conditions. It also presents bidirectional characteristic, which can be very useful for other applications.

5.1.1 MIC topology selection

In order to select the most suitable converter for this purpose it is required to consider the system to be controlled. Table 5.1 shows the main characteristics of the hybrid system. After the analysis of the wind power generation system, it has been determined that it will not exceed the characteristics showed in the table.

Table 5.1. Hybrid System electrical characteristics

Energy Input	$V_{in}(V)$	$I_{in}(A)$	$P_{in}(W)$
Solar	$[0; 18]$	$[0; 5.5]$	100
Wind	$[0; 25]$	$[0; 20]$	500

In order to charge a 12 V battery as desired, it will be necessary to step-down the voltage when both generation systems are supplying energy simultaneously. Thereby, considering this fact Figure (5.4)b is the most optimum choice.

However, when the photovoltaic power generation system is not supplying energy during the night, it might be necessary, to step-up the voltage from the wind power generation system to use the energy at low wind speed. Thereby the system from Figure (5.4)b has been considered the most suitable option for this application.

5.2 Double input buck-boost converter analysis

The analysis followed for this topology is similar as the one explained for the boost converter in Appendix B. As the first part of the double boost circuit is formed by the double buck topology, it will be briefly analysed first.
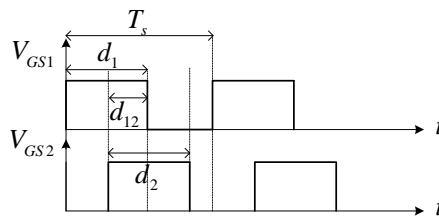
Circuit from Figure 5.4b, buck mode has four different stages, showed in Figure 5.6. Switching schemes from control signals are shown in Figure 5.7, in which intermediate synchronization has been used in this report.
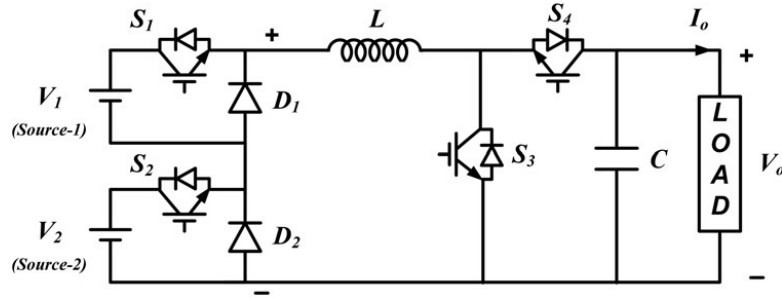
Figure 5.5. Multiple input topology with its main characteristic of adaptivity
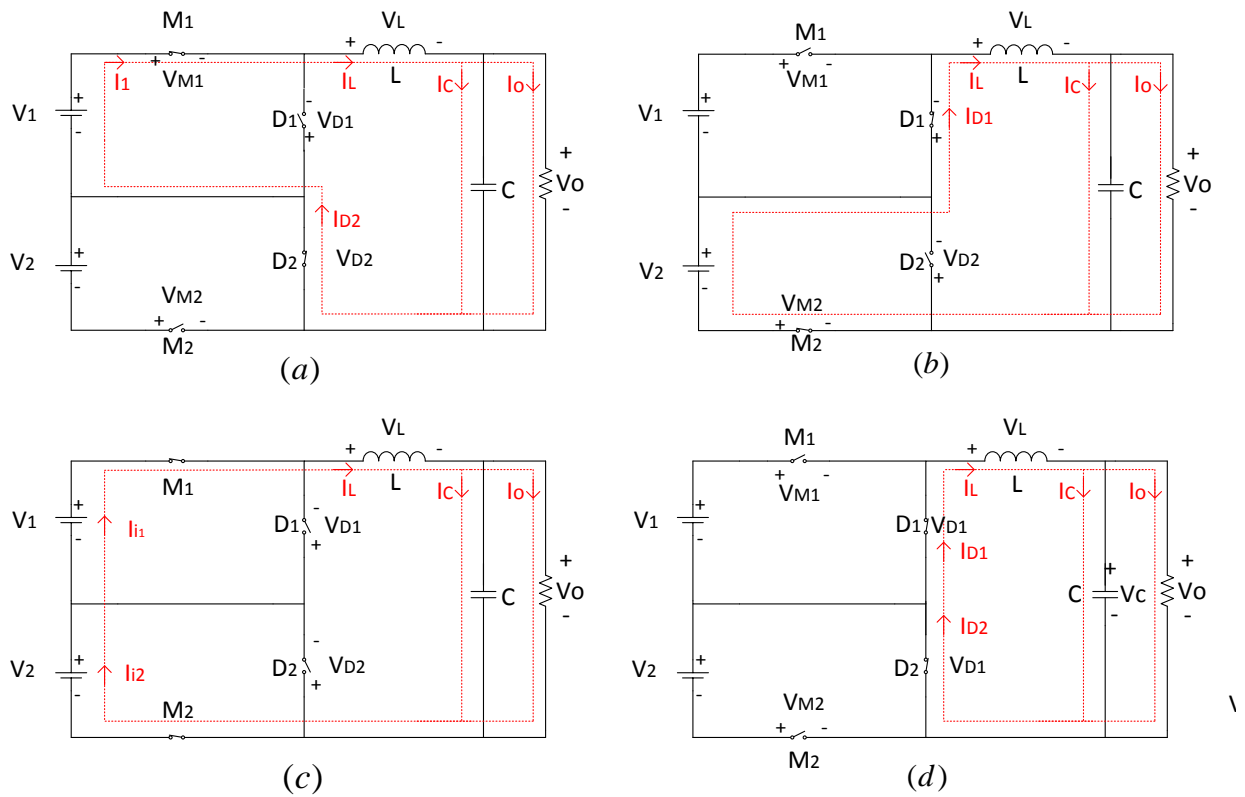
Figure 5.6. Double input buck converter topology.

Figure 5.7. Intermediate synchronization of switching waves.

According to the volt-second balance theorem, the average inductor voltage is zero as shown in Equation 7.1.

(5.1)
$$i_L = \frac{1}{L} \int_0^{T_s} v_L(t)dt + i_L(0) \rightarrow \int_0^{T_s} v_L(t)dt = 0 \qquad [\text{-}]$$

By analysing the circuit at the four different stages shown in Figure 5.6, Equation 5.2 is derived. In here, d_1 and d_2 are the duty cycles of the control signals V_{GS1} and V_{GS2}, whereas d_{12} corresponds with the duty cycle of the signals when they are both in ON state.

(5.2)
$$T_s\left[(V_1 - V_o)(d_1 - d_{12}) + (V_1 + V_2 - V_o)(d_{12}) + (V_2 - V_o)(d_2 - d_{12}) + (-V_o)(1 - d_1 - d_2 + d_{12})\right] = 0 \quad [\text{-}]$$

Simplifying Equation 7.1, the input-output relation depending on the duty cycle of both switches is derived in (5.3)

(5.3)
$$V_o = V_1 d_1 + V_2 d_2 \qquad [\text{V}]$$

In the same way, circuit from Figure 5.4b is analysed by including the duty cycle of the signal V_{GS3}, d_3. The behaviour of the system is now similar to the boost converter explained in Chapter B.

Figure 5.8 shows the three switching signal waveforms V_{GS1}, V_{GS2} and V_{GS3} and the current and the voltage in the inductor, V_L and I_L.
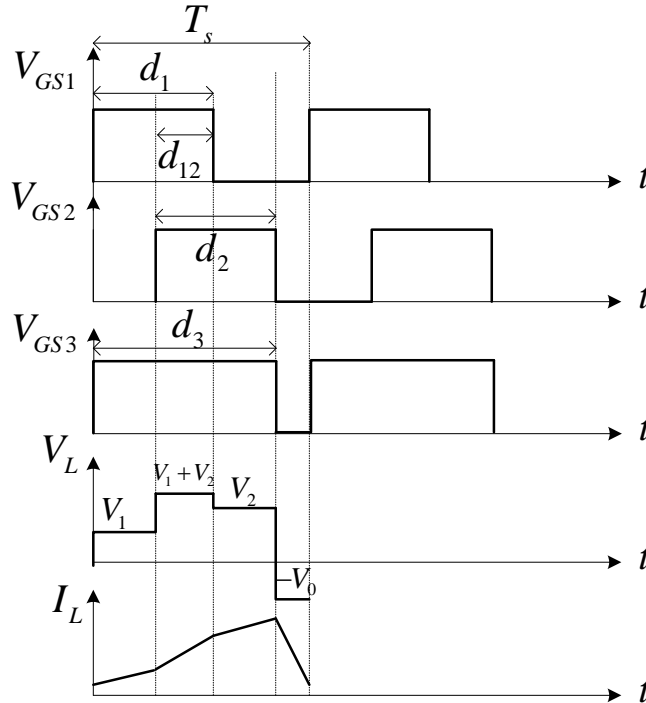
Figure 5.8. Switching signals V_{GS1}, V_{GS2} and V_{GS3}, and current and voltage through the inductor V_L and I_L for the double buck-boost circuit topology

Figure 5.9 shows four sketches of the different possible states of the circuit from Figure 5.4b. In Figure 5.9a, only the switch M_1 is on and as the switch M_3 is also ON, ON the inductance is being

charged with the current from the input source V_1. Meanwhile the voltage stored in the capacitor is maintaining the output voltage level.

In Figure 5.9b, as both switches M_1 and M_2 are ON, the inductor is charged with both input sources.In Figure 5.9c, only the switch M_2 is ON and the input voltage source V_2 is supplying energy to the inductance.

Finally in Figure 5.9c, the three switches are OFF and all the energy previously stored in the inductance flows to the load and to recharge the capacitor.
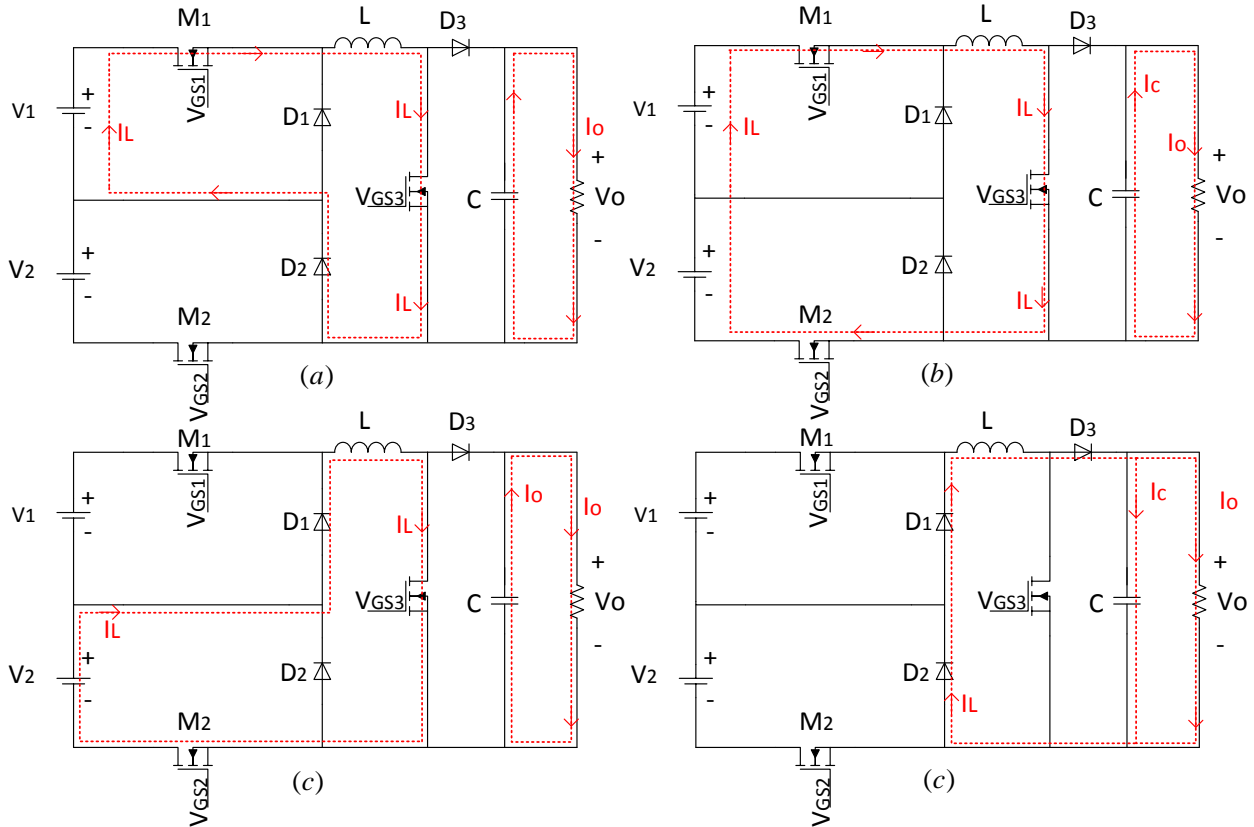
Figure 5.9. Four different working operation stages of the double buck-boost converter topology.

The input output voltage relation is derived following the same procedure as the double buck converter, and it is shown in Equation 5.4.

$$(5.4) \qquad V_o = \frac{V_1 d_1 + V_2 d_2}{1 - d_1 - d_2 + d_{12}} \qquad \text{[V]}$$

The current in the capacitor is defined in Equation 5.5.

$$(5.5) \qquad C\frac{dv_o}{dt} = i_c = i_L - \frac{V_o}{R} \qquad \text{[V]}$$

Considering the double input converter as a lossless ideal system, the input power must be the same as the output power. Then it yields to (5.6):

$$(5.6) \qquad V_1 I_1 + V_2 I_2 = V_o I_o \rightarrow I_o = \frac{V_1 I_1 + V_2 I_2}{V_o} = \frac{(V_1 I_1 + V_2 I_2)(1 - d_1 - d_2 + d_{12})}{V_1 d_1 + V_2 d_2} \qquad \text{[-]}$$

Both input current I_1 and I_2 can be expressed in function of the inductor current I_L, as $I_1 = d_1 I_L$ and $I_2 = d_2 I_L$ and previous Equation 5.6 can be simplified in (5.7)

$$(5.7) \qquad\qquad I_o = I_L(1 - d_1 - d_2 + d_{12}) \qquad\qquad [V]$$

Equation 5.7 can be transformed into the input current equation for both power generation sources, they are defined as follows5.8:

$$(5.8) \qquad\qquad \begin{aligned} I_1 &= I_o \frac{d_1}{(1-d_1-d_2+d_{12})} \\ I_2 &= I_o \frac{d_2}{(1-d_1-d_2+d_{12})} \end{aligned} \qquad\qquad [A]$$

From previous Equation 5.8, Equation 5.9 is derived. In here, it proves it is possible to control the input current by changing the duty ratio.

$$(5.9) \qquad\qquad \frac{I_1}{I_2} = \frac{d_1}{d_2} \qquad\qquad [A]$$

The inductor current and the capacitor voltage ripple ΔI_L and ΔV_L defines the inductor and capacitor values L and C respectively, as shown in Equation 5.10 and 5.11:

$$(5.10) \qquad\qquad \Delta I_L = \frac{V_o(1 - d_3)}{2Lf_s} \qquad\qquad [A]$$

$$(5.11) \qquad\qquad \Delta V_C = \frac{V_o}{2R_{load}Cf_s} \qquad\qquad [A]$$

5.3 System design and small signal model

In this section state-space averaging will be calculated for the topology selected, with the purpose of analysing the average values of state variables lie voltage and current in steady state. In state-space averaging the elements which store energy are considered the state space variables, and as the energy level stored does not remain constant over a switching cycle those elements need to be averaged. The procedure to follow in state-space averaging is to calculate the different equations for each state and then they are averaged with the corresponding duty ratio.

The state-space equation is defined in (5.12)

$$(5.12) \qquad\qquad \begin{aligned} [K]X(t) &= Ax(t) + Bu(t) \\ y(t) &= Fx(t) + Gu(t) \end{aligned} \qquad\qquad [\text{-}]$$

where the state-vector is $x(t) = \begin{bmatrix} i_L \\ v_c \end{bmatrix}$, the input vector is $u(t) = \begin{bmatrix} v_1 \\ v_2 \end{bmatrix}$ and $y(t) = \begin{bmatrix} i_1 \\ i_2 \end{bmatrix}$ is the output vector. K contains the value of the inductor and capacitor and matrix A, B, F and G corresponds to constants for different states of the converter.

The proposed converter, the buck-boost has four states on each cycle, shown in the graph from Figure 5.9.By multiplying Equation 5.12 to each time interval Equation 5.13 is derived, in which all the averaged state equations over a switching cycle are included.

(5.13)

$$K\dot{X}(t) = t_1 A_1 x(t) + B_1 u(t) + t_2 A_2 x(t) + B_2 u(t) + t_3 A_3 x(t) + B_3 u(t) + t_4 A_4 x(t) + B_4 u(t)$$
$$y(t) = t_1 F_1 x(t) + G_1 u(t) + t_2 F_2 x(t) + G_2 u(t) + t_3 F_3 x(t) + G_3 u(t) + t_4 F_4 x(t) + G_4 u(t)$$

[-]

where $t_1 = d_1 - d_{12}$, $t_2 = d_{12}$, $t_3 = d_2 - d_{12}$ and $t_4 = d_1 - d_1 - d_2 + d_{12}$.

Small perturbations need to be considered in the state-space equations in order to linearise disturbances on the system caused by the time varying variables. Therefore, small variations are included in all the time varying variables of the system(duty ratios, voltages and currents), as shown in Equation 5.14 and 5.15:

(5.14)

$$d_1(t) = d_1 + \tilde{\delta}_1(t)$$
$$d_2(t) = d_2 + \delta_2(t)$$
$$d_{12}(t) = d_{12} + \delta_{12}(t)$$

[-]

(5.15)

$$X(t) = X + \tilde{x}(t)$$
$$U(t) = U + \tilde{u}(t)$$
$$Y(t) = Y + \tilde{y}(t)$$

[-]

By deriving equations sated before, the state-space equations of buck-boost mode of operation after the small signal analysis are acquired. Equation shows the inductor voltage, the capacitor current and input current I_1 and I_2.

(5.16)

$$L\frac{di_L}{dt} = v_1(t)d_1 + v_2(t)d_2 - \{1 - (d_1 + d_2 - d_{12})\} v_c(t) + V_1\tilde{\delta}_1(t) + V_2\tilde{\delta}_2(t) - V_c\left\{\tilde{\delta}_1(t) + \tilde{\delta}_2(t) - \tilde{\delta}_{12}(t)\right\}$$
$$C\frac{dv_c}{dt} = \{1 - (d_1 + d_2 - d_{12})\} i_L(t) - \frac{v_c(t)}{R} + \left\{\tilde{\delta}_1(t) + \tilde{\delta}_2(t) - \tilde{\delta}_{12}(t)\right\} I_L$$
$$I_1 = i_L(t)d_1 + I_L\tilde{\delta}_1(t)$$
$$I_2 = i_L(t)d_2 + I_L\tilde{\delta}_2(t)$$

[-]

As shown in the small signal model, it is required to place a reactive element which as a filter to reduce the switching harmonics and transfer the energy from the input to the output. It consist on a low pass filter for the output currents and voltages at the cut-off frequency(lower than the switching frequency)[8].

Mathematical Model

After deriving the small signal model, it is possible to transform it into a mathematical model applying the Laplace transformation on the inductor voltage and capacitor current equations from (5.16). By obtaining the mathematical model, it is possible to analyse the effect of the small signal perturbation over the different variables in the model. The goal is to obtain the v_c equation in terms of those perturbations. The load current I_load is included in the model in order to study the open loop response of the system.

(5.17)

$$sLi_L(s) = v_1(s)d_1 + v_2(s)d_2 - \{1 - (d_1 + d_2 - d_{12})\} v_c(s) + V_1\tilde{\delta}_1(s) + V_2\tilde{\delta}_2(s) - V_c\left\{\tilde{\delta}_1(s) + \tilde{\delta}_2(s) - \tilde{\delta}_{12}(s)\right\}$$
$$sCv_c(s) = \{1 - (d_1 + d_2 - d_{12})\} i_L(s) - \frac{v_c(s)}{R} + \left\{\tilde{\delta}_1(s) + \tilde{\delta}_2(s) - \tilde{\delta}_{12}(s)\right\} I_L - i_{load}$$

Superposition law is applied on the previus equation and deriving the equations it is possible to obtain all the transfer functions for the $v_c(s)$ and i_L over the different perturbances.

For example, for obtaining the transfer function of $\frac{v_c(s)}{i_{load}}$, $v_1(s)$, $v_2(s)$, $\tilde{\delta}_1(s)$,$\tilde{\delta}_2(s)$ and $\tilde{\delta}_{12}(s)$ are equated to zero and combining both equations from 5.17 and isolating $v_c(s)$, Equation 5.18 is obtained:

$$(5.18) \qquad Z_o = \frac{sL}{s^2LC + s\frac{L}{R} + \{1 - (d_1 - d_2 + d_{12})\}^2} \qquad [V]$$

Transfer functions for the $v_c(s)$ referred to $v_1(s)$ and $v_2(s)$ respectivily are shown below in Equation 5.19 and 5.20

$$(5.19) \qquad \frac{v_c(s)}{v_1(s)} = G_{V,v_1} = \frac{d_1\{1 - (d_1 + d_2 - d_{12})\}}{s^2LC + s\frac{L}{R} + \{1 - (d_1 - d_2 + d_{12})\}^2} \qquad []$$

$$(5.20) \qquad \frac{v_c(s)}{v_2(s)} = G_{V,v_2} = \frac{d_2(1 - (d_1 + d_2 - d_{12}))}{s^2LC + (1 - d_1 - d_2 + d_{12})^2} \qquad [\text{-}]$$

Equation 5.21 and 5.22 show the transfer function for the output $I_L(s)$ referred to the input voltage $V_1(s)$ and $V_1(s)$ respectively.

$$(5.21) \qquad \frac{i_L(s)}{v_1(s)} = G_{I,v_1}(s) = \frac{d_1(sC + \frac{1}{R})}{s^2LC + s\frac{L}{R} + (1 - (d_1 + d_2 - d_{12}))^2} \qquad [\text{-}]$$

$$(5.22) \qquad \frac{i_L(s)}{v_2(s)} = G_{I,v_2}(s) = \frac{d_2(sC + \frac{1}{R})}{s^2LC + s\frac{L}{R} + (1 - (d_1 + d_2 - d_{12}))^2} \qquad [\text{-}]$$

Following the same procedure, the different transfer functions for all the perturbations can be derived. The superposition law states that the sum of all the individual perturbations equal to the total ouput perturbation. Hence, the total ouput perturbation of voltage is defined in Equation 5.23 and the total perturbation of current is defined in Equation 5.24

$$(5.23) \quad v_c(s) = -i_{load}Z_o(s) + G_{V,v_1}v_1(s) + G_{V,v_2}v_2(s) + G_{V,\delta_1}\delta_1(s) + G_{V,\delta_2}\delta_2(s) + G_{V,\delta_{12}}\delta_{12}(s) \qquad [\text{-}]$$

$$(5.24) \quad i_L(s) = -i_{load}\frac{Z_o(s)}{sL} + G_{I,v_1}v_1(s) + G_{I,v_2}v_2(s) + G_{I,\delta_1}\delta_1(s) + G_{I,\delta_2}\delta_2(s) + G_{I,\delta_{12}}\delta_{12}(s) \qquad [\text{-}]$$

Bode plot of transfer the functions $G_{I,v_1}(s)$, G_{V,v_1} are plotted together in Figure 5.10.

Frequency response analysis has been done for the double input buck-boost converter, for ideal components. A more real analyses is done by considering the effect of the inductor and capacitor resistances. Transfer functions from Equation 5.19 and 5.20 have been re-calculated by considering those losses and Equations 5.25 and 5.26 are derived:

(5.25)
$$\frac{v_c(s)}{v_1(s)} = G_{V,v_1} = \frac{d_1\left\{1 - (d_1 + d_2 - d_{12})\right\}(sCr_c + 1)}{s^2(LC + \frac{L}{R}Cr_c) + s(C(r_L + r_C) + \frac{L}{R} + \frac{Cr_Lr_C}{R}) + (\frac{r_L}{R} + \{1 - (d_1 + d_2 - d_{12})\}^2)} \quad [\text{-}]$$
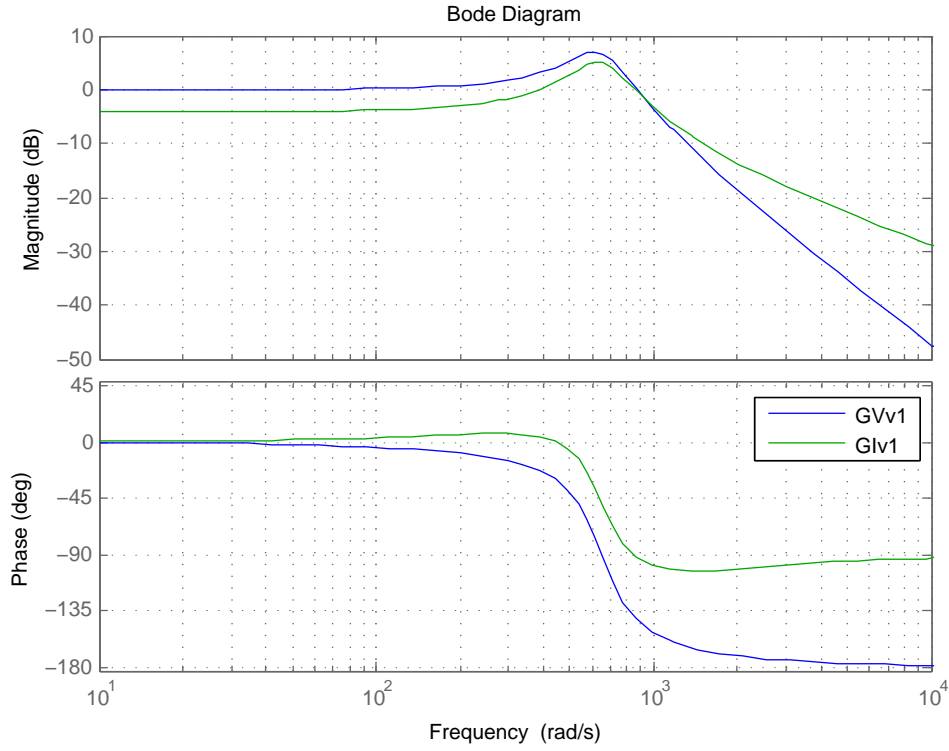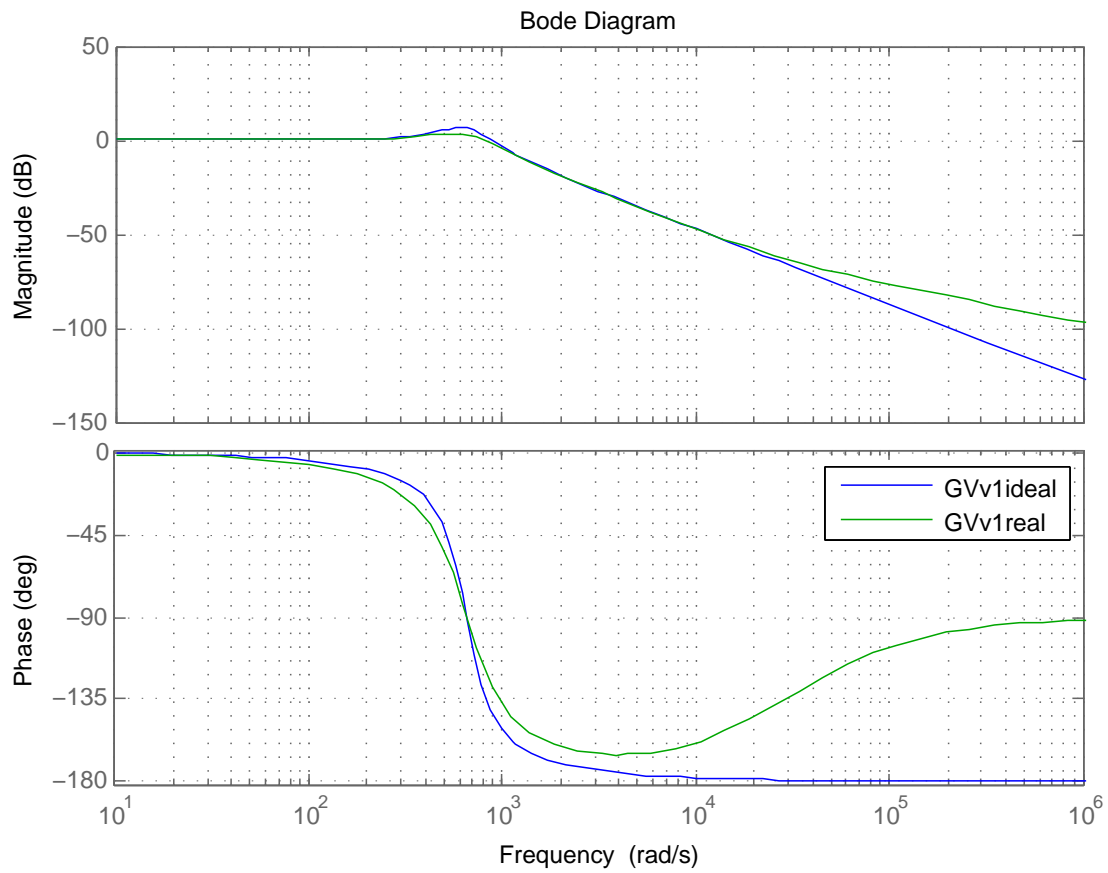
Figure 5.10. Bode plot for both transfer functions G_{V,v_1} and G_{I,v_1}.The parameters used are: $d1 = 0.4$, $d2 = 0.4$, $d12 = 0.2$, $L = 1.13\text{mH}$, $C = 333\mu\text{F}$ and $R = 10\Omega$.

(5.26)

$$\frac{v_c(s)}{v_2(s)} = G_{V,v_2} = \frac{d_2\left\{1 - (d_1 + d_2 - d_{12})\right\}(sCr_c + 1)}{s^2(LC + \frac{L}{R}Cr_c) + s(C(r_L + r_C) + \frac{L}{R} + \frac{Cr_Lr_C}{R}) + (\frac{r_L}{R} + \{1 - (d_1 + d_2 - d_{12})\}^2)} \quad [\text{-}]$$

where r_L and r_C are the inductance and capacitance resistances.

In Figure 5.11 the frequency response of G_V, v_1 for ideal components and real components is shown.

Figure 5.11. Bode plot for both transfer functions G_{V,v_1} and G_{I,v_1}, considering the losses produce by the capacitor and inductar resistance r_L and r_C. The parameters used are: $d1 = 0.4$, $d2 = 0.4$, $d12 = 0.2$, $L = 1.13\text{mH}$, $C = 333\mu\text{F}$ and $R = 10\Omega$.

Chapter 6

MIC power converter control and simulations results

In this chapter the power control of the MIC converter will be explained and the system controllers will be designed. Simulation results of the MIC converter under steady state conditions will be presented.

6.1 Power Management and control design

Figure 6.1 shows the schematic diagram of double input DC/DC converter implemented and the control unit for the wind turbine and photovoltaic panel input sources.
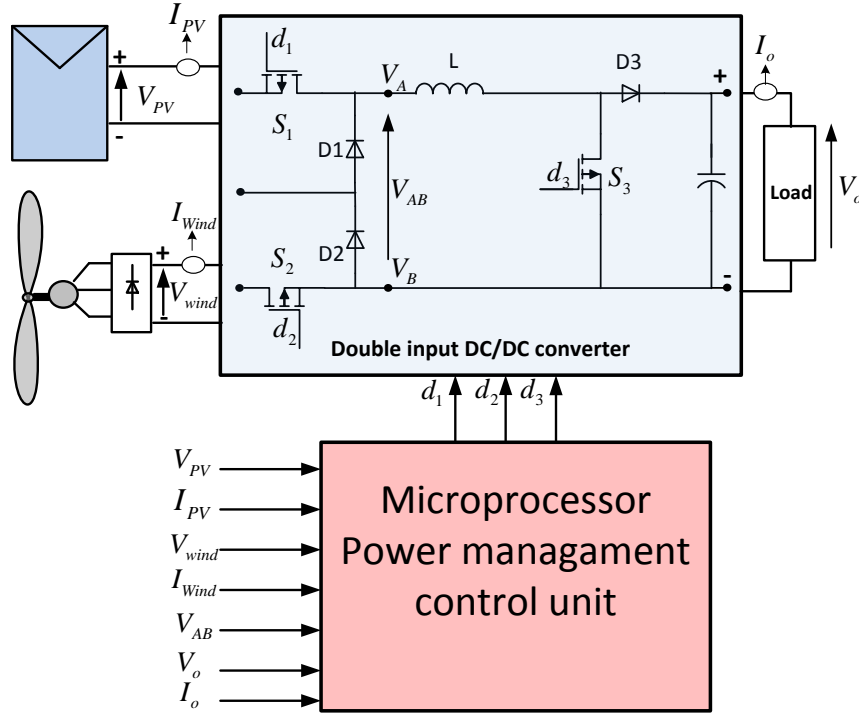
The system works under two modes of operation, buck-boost or buck mode. Figure 6.2 shows an schematic of the control operation mode algorithm inside the microcontroller. The control unit reads the value of the voltage V_{AB} and after filtering it is compared with the reference output. After this comparison the microcontroller selects the operating mode.

For values lower than the output reference voltage, the system will be working under operation mode I and for higher voltages it will be the operation mode II.

Operating mode I

Operating mode II starts when the voltage V_{AB} is greater than the voltage level required at the
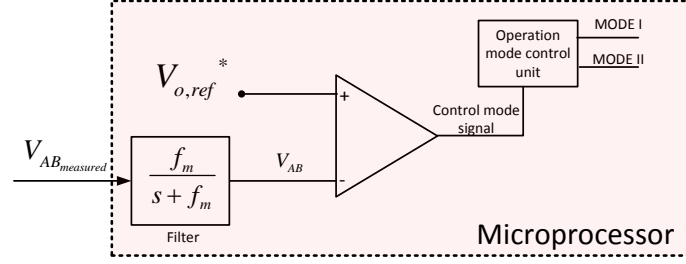
Figure 6.2. Operation model unit

output of the converter. In here, the system works under buck operation mode. Figure 6.3 shows the schematic diagram of this operating mode, were the control variables are only d_1 and d_2 as the switch S_3 is OFF permanently. In here, no MPPT algorithm is implemented as the system works under buck operating mode
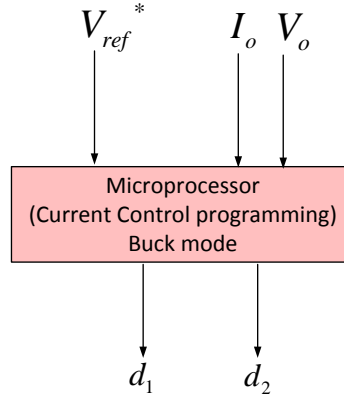
Figure 6.3. Control mode 2

From the small signal analysis, Equation 6.1 and 6.2 have been derived:

$$(6.1) \qquad L\frac{di_L}{dt} = v_1(t)d_1 + v_2(t)d_2 + V_1\tilde{\delta}_1(t) + V_2\tilde{\delta}_2(t) - v_c(t) \qquad [\text{-}]$$

$$(6.2) \qquad C\frac{dv_c}{dt} = i_L(t) - \frac{v_c(t)}{R} \qquad [\text{-}]$$

The plant transfer function for buck mode operation is given in 6.3, where $d_1(s)$ and $d_2(s)$ are the two control inputs, $i_L(s)$ and $v_c(s)$ are the two controlled variables. G_1, G_2, G_3 and G_4 are the transfer functions.

$$(6.3) \qquad Y(s) = \begin{bmatrix} i_L(s) \\ v_c(s) \end{bmatrix} = \begin{bmatrix} G_{11}(s) & G_{12}(s) \\ G_{21}(s) & G_{22}(s) \end{bmatrix} \begin{bmatrix} d_1(s) \\ d_2(s) \end{bmatrix} \qquad [\text{-}]$$

where G_{11} and G_{12} represent the control to current transfer functions and G_{21} and G_{22} control to output transfer functions.

Figure 6.4 shows the inner and outer loop of the system working in operating mode II. G_1 and G_2 are the control to current and current to output transfer functions. T_{C_1} represent the PI controller of the current loop, which increases the low-frequency loop gain. T_{C_2} is the controller for the outer loop. For the outer loop current to output transfer function is required, $G_2 = \frac{V_c(s)}{i_L(s)}$. The close loop gain H is equal to one, $H(s) = 1$
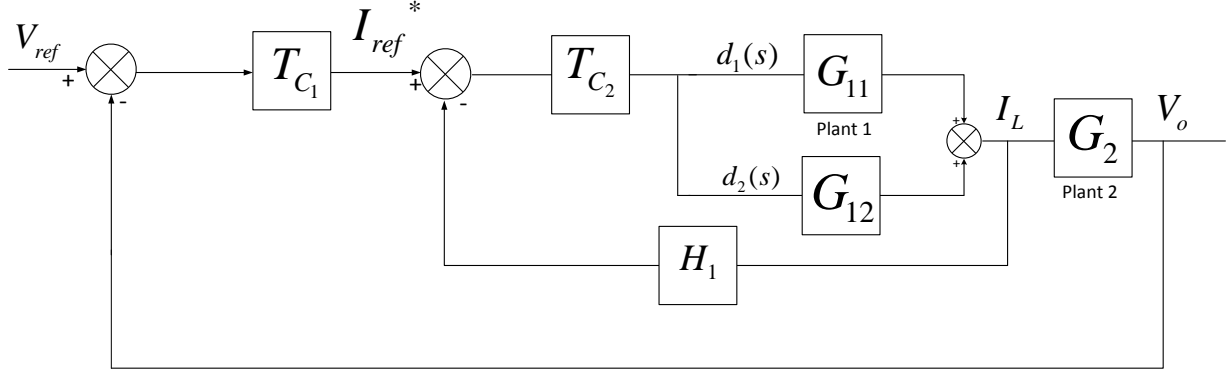
Figure 6.4. System control design

The dynamic response of the voltage loop must be lower than the inner loop and therefore, the crossover frequency of the outer loop should be lower than the current loop[22]. Applying this constraint, the design of both controllers results easier because as the inner loop has faster dynamics the current in the inductor changes more quickly than the response of the outer loop.

With the purpose of simplifying the control design, the system has been considered ideal so neither inductor resistance nor capacitor resistance has been considered.

Current regulator design

Control to output transfer function G_{11} and G_{12} from figure 6.5 are derived from the small signal model of the buck mode multiple input converter. They are shown in Equations 6.4 and 6.5. The transfer function of the compensator design is: $T_{C_2} = k_{p2} + \frac{k_{i_2}}{s}$.
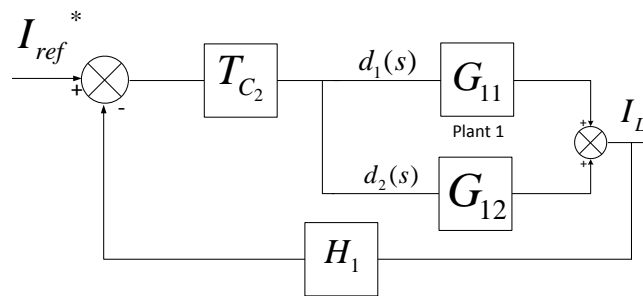
Figure 6.5. Current control

$$(6.4) \qquad G_{11} = \frac{i_L(s)}{\tilde{\delta}_1(s)} = \frac{V_1}{(Ls + \frac{R}{CR+1})} \qquad [-]$$

$$(6.5) \qquad G_{12} = \frac{i_L(s)}{\tilde{\delta}_1(s)} = \frac{V_2}{(Ls + \frac{R}{CR+1})} \qquad [-]$$

Bode diagram and step response of the plant G_1 formed by transfer functions G_{11} and G_{12} are shown below in (6.6) and (6.7)
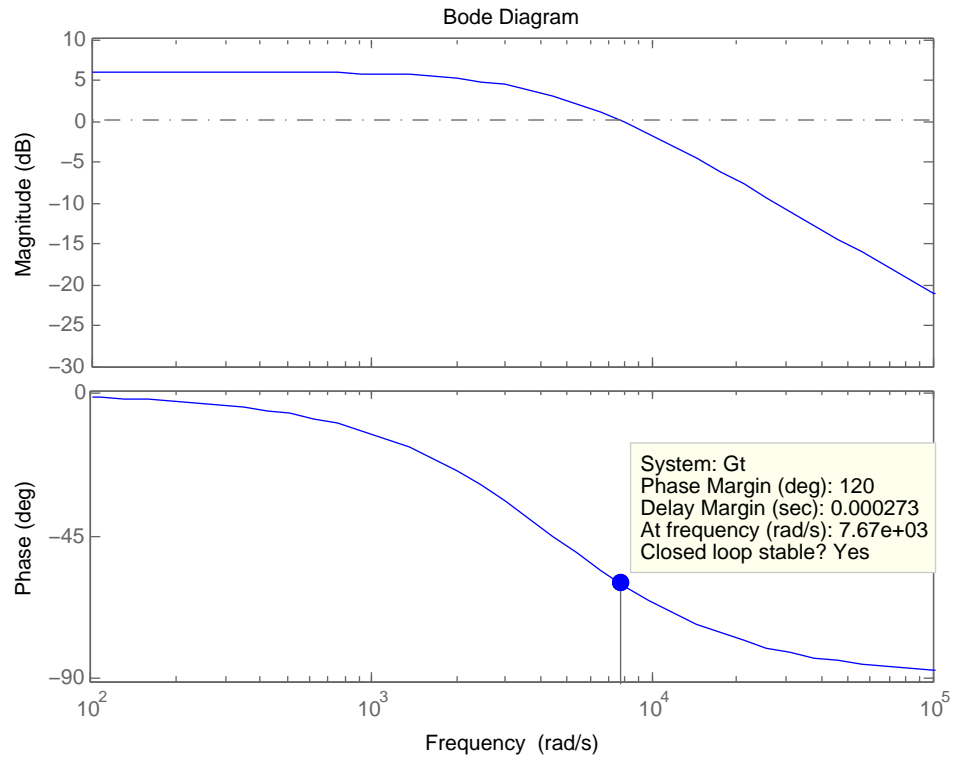
Figure 6.6. Bode diagram of the uncontrolled inner loop plant. Phase margin is $PM = 120°$ at $f_c = 1.22\text{kHz}(w_c = 7.67K\,\text{rad}/\sec)$
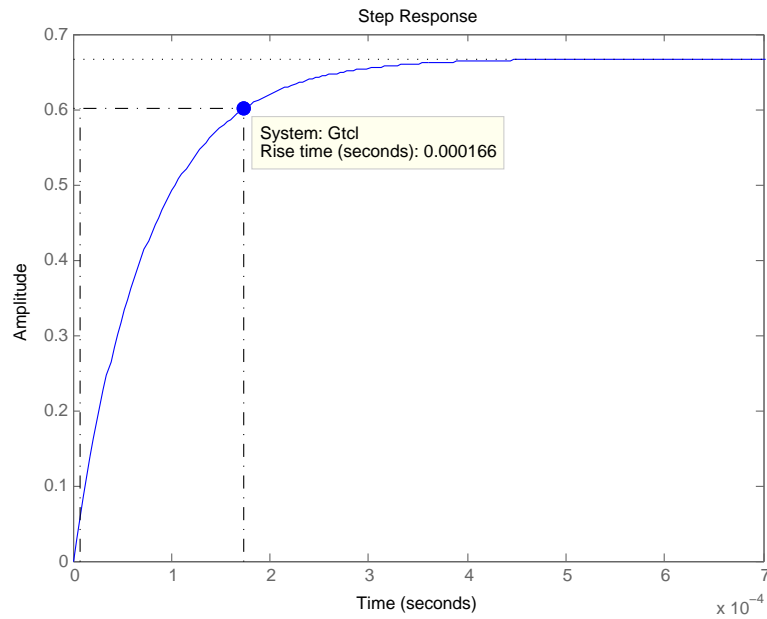

Figure 6.7. Step response of the plant G_1 uncompensated. The rise time is $T_r = 166\mu\sec$

The uncompensated system is stable and its phase margin is $PM = 120°$ at $f_c = 1.22$kHz$(w_c = 7.67K$rad$/$sec$)$. The system responds with a rise time of $T_r = 166\mu$sec. The system responds fast but the step response shows an steady state error which must be compensated. Therefore, a PI controller is designed to reduce this steady state error and increase the low frequency gain. The phase margin must be maintained positive and the frequency will be reduced.

The values of the PI controller have been obtained through SISOtool, keeping the constrains previously mentioned. The values of the controller are: $k_i = 516330$ and $k_p = 9.29$. The bode plot and the step response of the compensated system is shown below in 6.8 and 6.9.

The system is faster now, the rise time is $T_r = 13.7\mu$sec and the phase margin is $PM = 62.4°$ at $f_c = 15$kHz. The low frequency gain has been increased and the steady state error has been compensated.
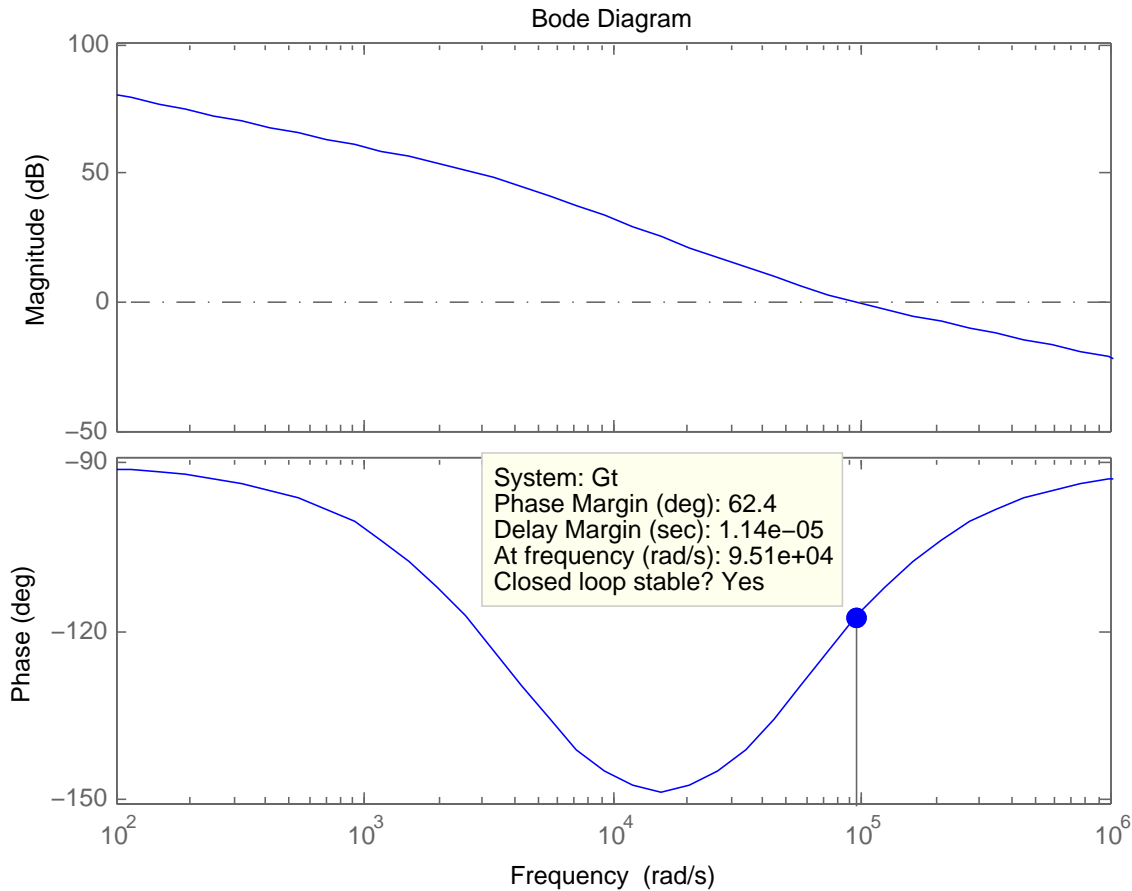
Figure 6.8. Compensated system bode diagram. Phase margin is $PM = 60°$ at $f_c = 15$kHz$(w_c = 95.1K$rad$/$sec$)$

Outer loop control design

Once the inner loop has been designed, it is possible to proceed with the design of the voltage loop controller. Figure shows the 6.10 outer loop, formed by the controller T_{C_1}, the inner loop and the transfer function for plant 2 G_2.

The controller for the outer loop should be slower than the inner loop as previously explained. It has been decide that the outer loop crossover frequency must ten times slower than the inner loop one. The transfer function of the compensator design is: $T_{C_1} = k_{p_1} + \frac{k_{i_1}}{s}$.
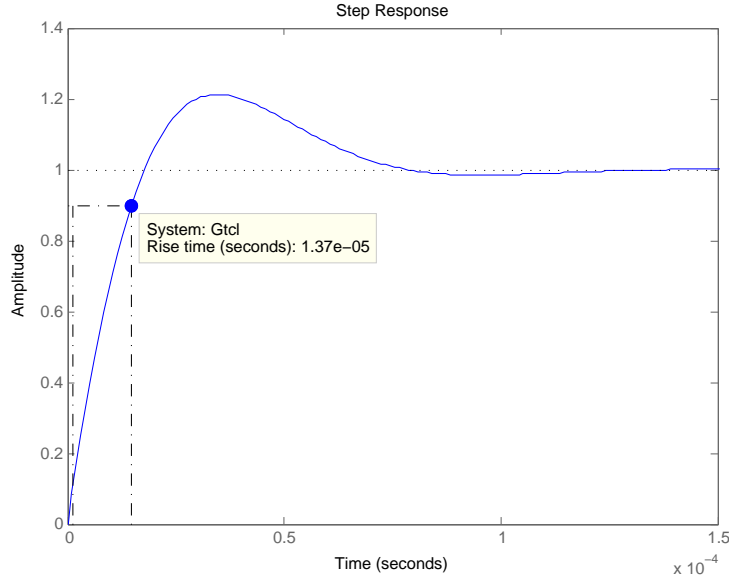
Figure 6.9. Step response of the compensated system, the rise time is $T_s = 351\mu\sec$ and the system reaches the steady state value at $t = 2.5\mathrm{m}\sec$
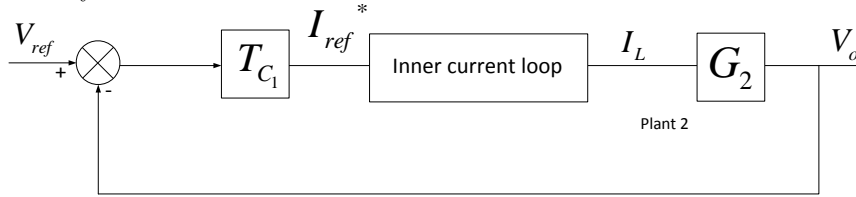
Figure 6.10. Outer control loop schematic diagram.

(6.6)
$$G_2 = \frac{v_c(s)}{i_L(s)} = \frac{R}{1 + sCR}$$
[-]

In Figure 6.12 the bode plot of the uncompensated outer loop is showed. Its phase margin is $PM = 102°$ at $f_c = 2.94K\mathrm{rad}\sec$. Following the constrain stated, the system must have a crossover frequency of $w_c = 9.4K\mathrm{rad}\sec$.

Figure 6.11 shows the step response of the uncompensated system, which shows a rise time of $T_r = 610\mu\sec$ and a steady state error which must be compensated.

The designed controlled has the following parameters: $k_i = 7424.8$ and $k_p = 31.92$. Figure 6.13 shows the bode plot of the whole system. It presents a crossover frequency of $f_c = 1.5\mathrm{kHz}$ and a phase margin of $PM = 79.6$. The step response is showed in Figure 6.14 and the rise time is $T_r = 157\mu\sec$.

The controller designed is verified by applying it to the simulation of the double input converter in buck mode of operation. Figure 6.15 shows the response of the simulated system under buck mode of operation. The response is slower than the step response of the system transfer function due the idealities considered when designing the controller.

Operating mode II

In this mode, the MPPT algorithm generates the reference current to control both input switches, S_1 and S_2 with the purpose of extracting the maximum power available from both input sources. On the
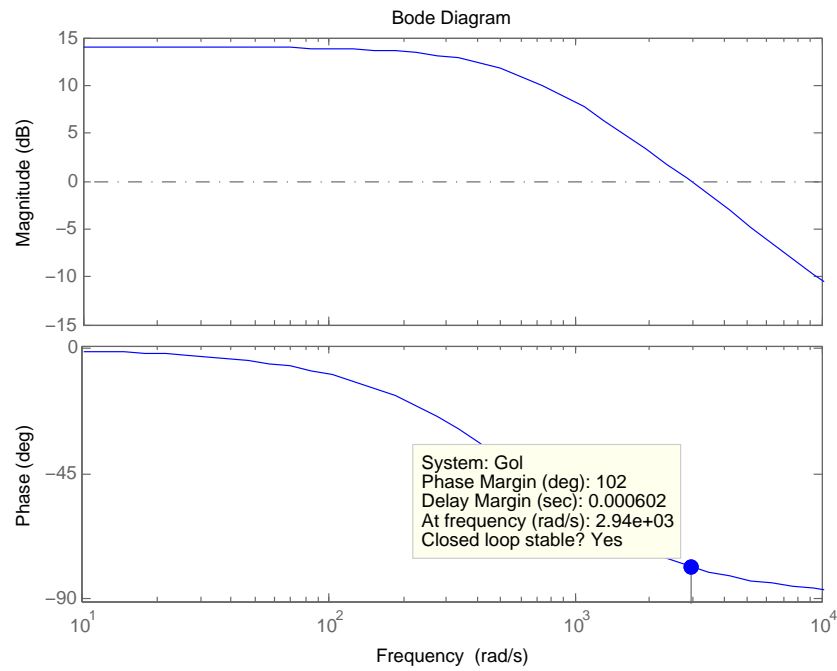
Figure 6.11. Bode diagram of the outer loop system. The phase margin is $PM = 102°$ at $f_c = 18\text{kHz}$.
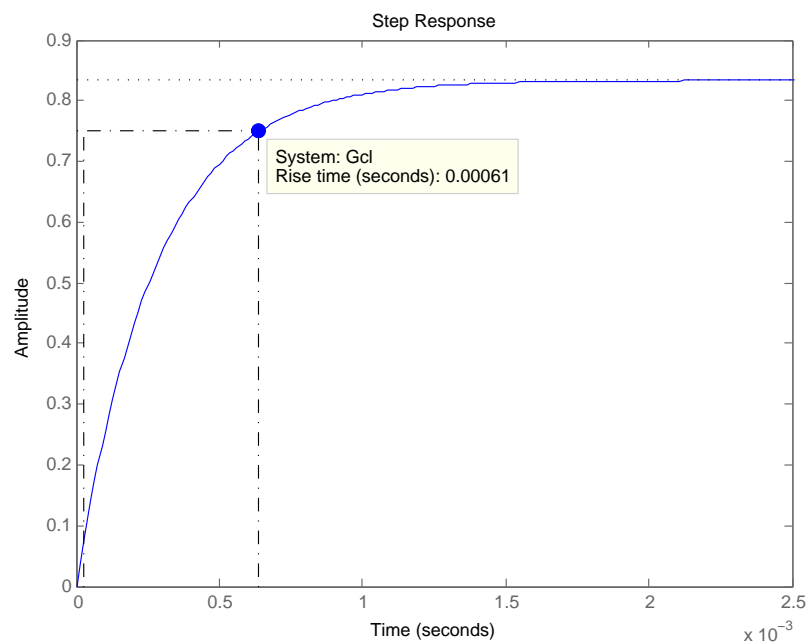
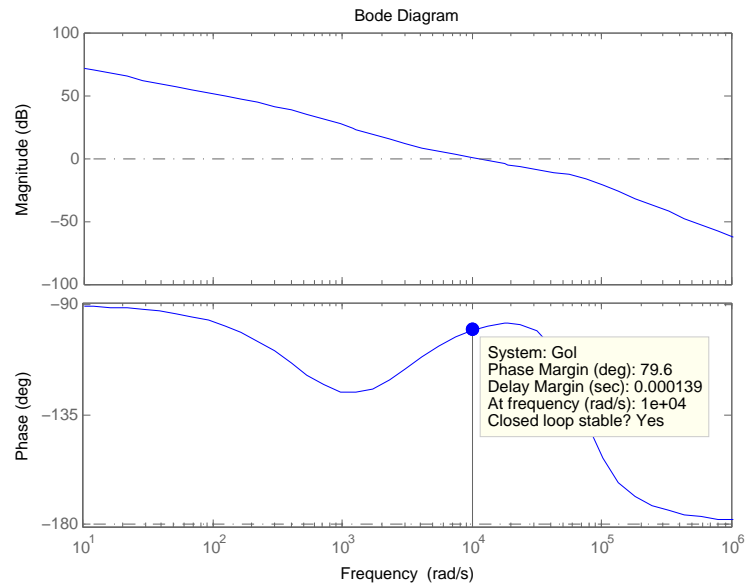**Figure 6.12.** Step response of the outer loop with no controller, $T_r = 610\mu\,\text{sec}$
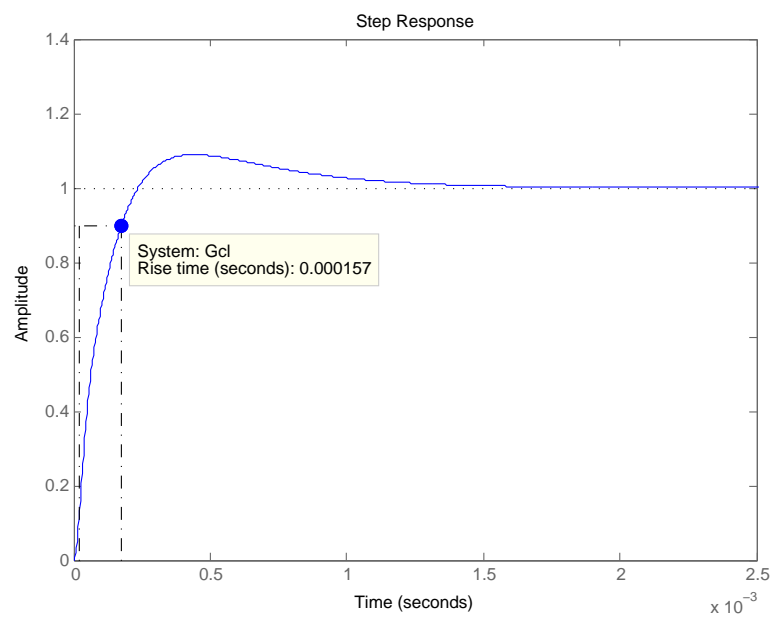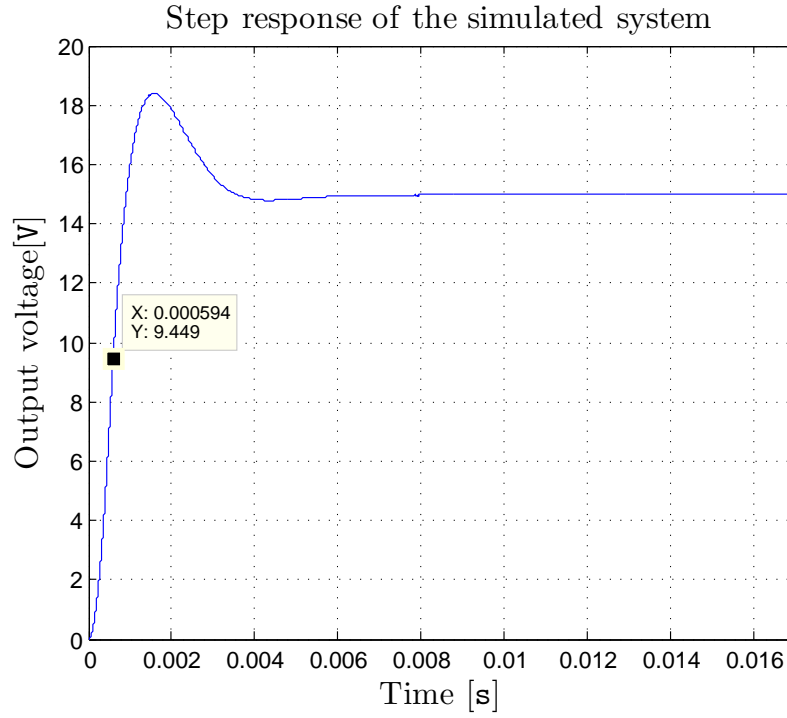
Figure 6.13. Bode

Figure 6.14. Step

Figure 6.15. Step response for the simulated system working under buck mode of operation $[V_1 = 10, V_2 = 15, V_o = 15\text{V}]$.

other hand, S_3 is controlled by the microcontroller to keep the voltage reference level at the output.

Figure 6.16 shows the schematic diagram of this control mode. The MPPT unit, as explained in Chapter 3 and 4,tracks the maximum power point and generates the reference current. Each input current source is measured and compared with its reference and both control signals are generated.

Switch S_3 is used to maintain the output voltage constant at the level of the reference signal. The system is basically a boost converter, being V_{AB} the input. Current and voltage control will be applied to maintain the desired output voltage level. In case of either one fo the input sources is not working or both power generation systems do not produce enough energy, the voltage is elevated to keep the desired output voltage level.
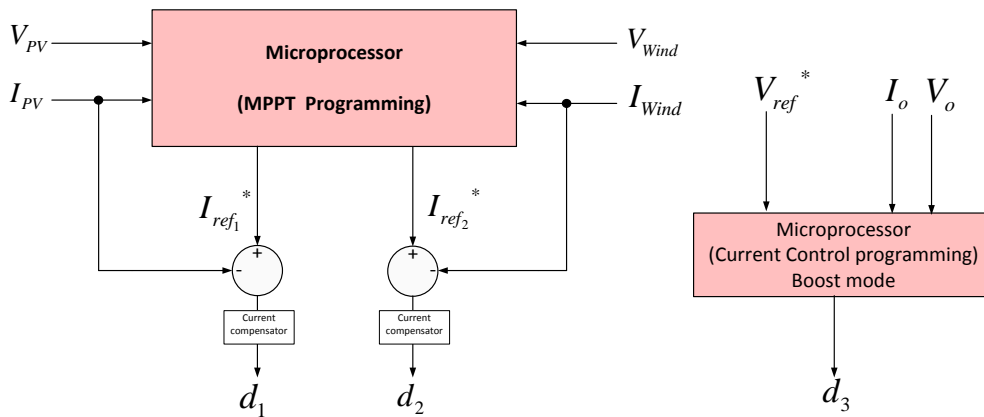
**Figure 6.16.** Control mode of operation II.

The design of the controller for the boost mode of operation is done similarly to the buck mode. The inner loop is designed to be faster than the outer loop, thereby the current loop can correct the errors

before voltage loop reads its input. Thereby, when designing the voltage loop the dynamics can be neglected in the transfer function. The control-to-input and current-to output transfer functions for boost mode of operation are shown in Equation 6.7 and 6.8

$$(6.7) \qquad \frac{i_L(s)}{\tilde{\delta}_3(s)} = \frac{V_o RCs + 2V_o}{LCRs^2 + Ls + (1-D)^2 R} \qquad [\text{-}]$$

$$(6.8) \qquad \frac{v_c(s)}{i_L(s)} = \frac{(1-D)}{Cs + \frac{1}{R}} \qquad [\text{-}]$$

The values of the PI controller have been obtained through SISOtool, following the same procedure as the buck mode. The values of the controller for the inner loop are: $k_i = 44939$ and $k_p = 13.93$. For the voltage loop the values of the controller designed are $k_i = 160$ and $k_p = 0.176$. The bode plot and the step response of the compensated system is shown below in 6.17 and 6.18.
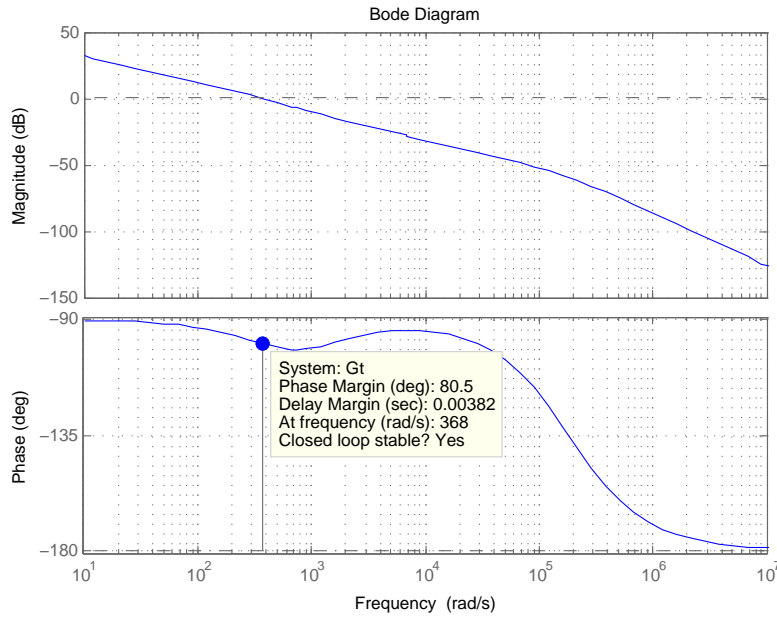
Figure 6.17. Bode plot of the compensated system

It must be mentioned that the design of this controller has been done considering the duty cycle from both input sources to be constant. In a further work, it should be tunned again considering that the MPPT controller will vary those duty cycles to extract the maximum power possible, and it will affect the response of the boost part of the circuit.

6.2   Steady state simulations of the proposed converter

In here the proposed converter will be simulated under different steady-state test conditions in order to verify the theory explained in Chapter **??**. In Table 6.1 the simulation parameters used for analysing the converter are shown.

Table 6.1. Simulation parameters for the two input DC/DC converter proposed.

V_1(V)	V_2(V)	L(mH)	r_L(mΩ)	C(mF)	r_C(mΩ)	f_s(kHz)	R_{load}
10	18	1	1	500	1	30	5
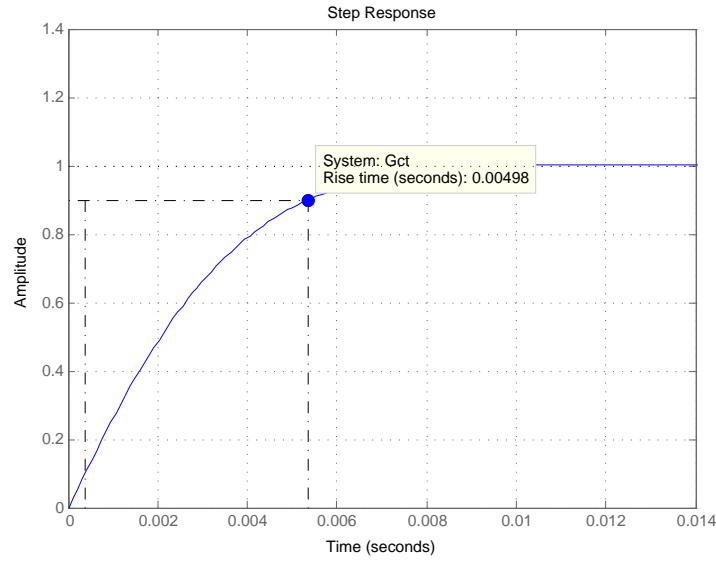
Figure 6.18. Step response of the compensated system

Figure 6.19,6.21 and 6.23 show the behaviour of the converter(using ideal volage sources) under the three different mode of operation: buck, buck-boost and boost. Figure 6.20, 6.22, 6.24 and 6.25 shows the output voltage and current waveform for different cases varying the three control signals, d_1, d_2 and d_3.

First, the converter is tested under buck mode of operation by keeping in OFF state the S_3 switch. Output voltage can be reduced by changing the values of switches S_1 and S_2. Figure 6.19 shows this mode of operation, in which inductor voltage v_L and current i_L waveforms are shown. Switching signals S_1 and S_3 use intermediate synchronization. In the inductor voltage waveform it is possible to observe the working principle of the converter, in which the inductance it is first charged with the energy coming from the input source V_1, then both input sources V_1 and V_2 supply energy to the inductance and to the output load and capacitor, then only V_2 supplies energy and finally all the energy stored in the inductance is used to keep the output voltage level. In Figure 6.20 the output voltage and current of the converter in buck mode of operation in which the output voltage is the 40 % of the total input voltage.

Figure 6.21 shows the waveforms of the buck-boost operation mode. In here, switching signals S_1 and S_2 step down the voltage, whereas signal S_3 is used to step up the voltage. The output voltage of the converter is the same(neglecting power losses) as in the input, even though switches from input V_1 and V_2 are ON only 40%of its maximum, because the voltage is then increased with S_3. By using this operation mode it would be possible to control the input voltage sources but at the same time maintaining the desired voltage in the output. In Figure the output waveforms are shown 6.22, both input voltages are first reduced and boosted in the output.

In Figure 6.23, the converter works in boost mode. In here the output voltage is increased by switching S_3. Figure 6.24 shows that the output voltage is 150 % greater for these values of the control signals.

In Figure 6.25 the output is only supplied by V_2 but switch S_2 is only opened for 40%, at time $t = 0.02$ sec the S_1 turns ON supplying all its energy into the system.

In this Chapter, MIC converters has been explained and the converter selected for this project has been stated. The MIC converter used for this purpose has been deeply analysed in order to understand its behaviour and its capacity. In the next Chapter the power converter control and simulation results
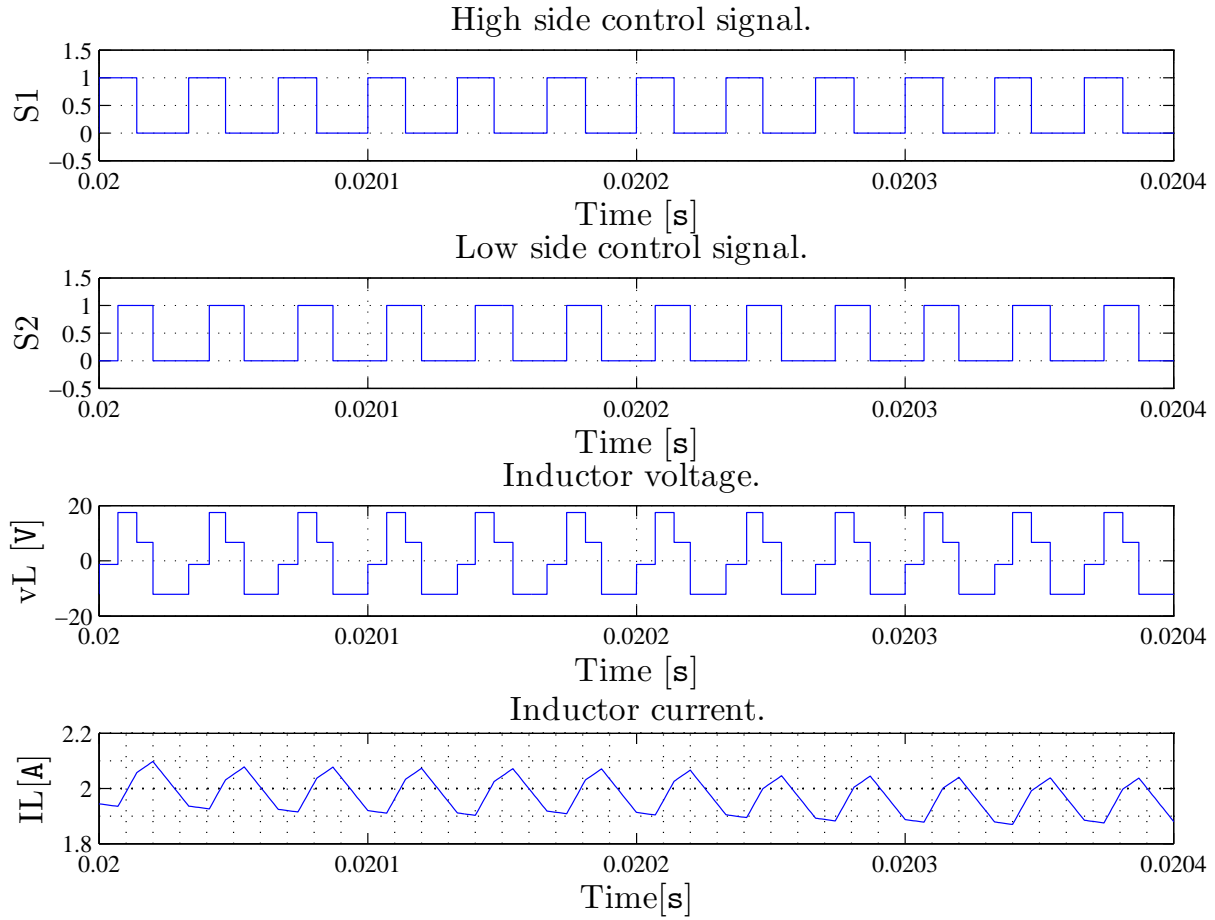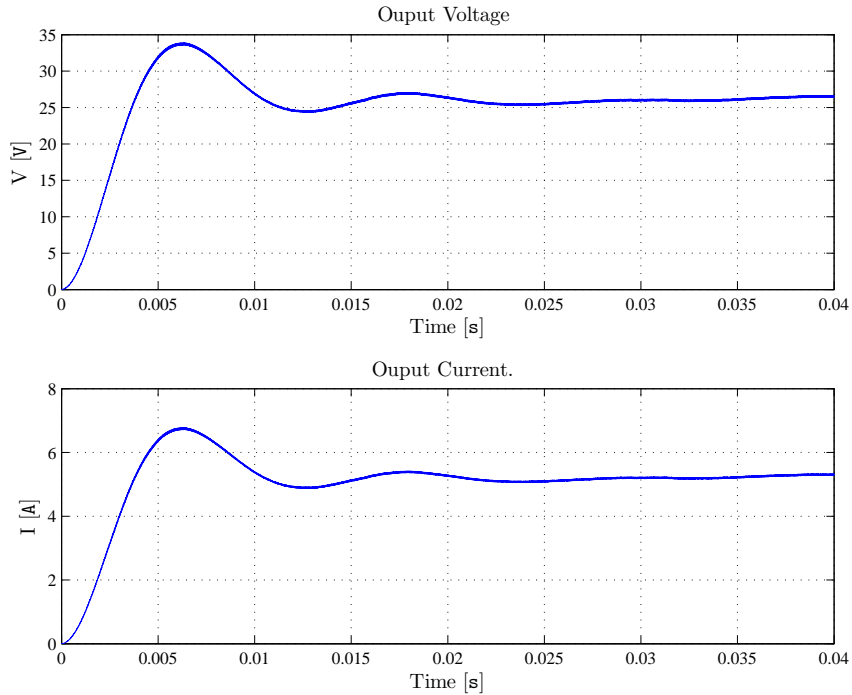
Figure 6.19. Simulation test of the MIC converter proposed under buck mode of operation, switching signals, I_L and V_L waveforms.[$d_1 = 0.4, d_2 = 0.4, d_3 = 0; V_o = 9.6$V]
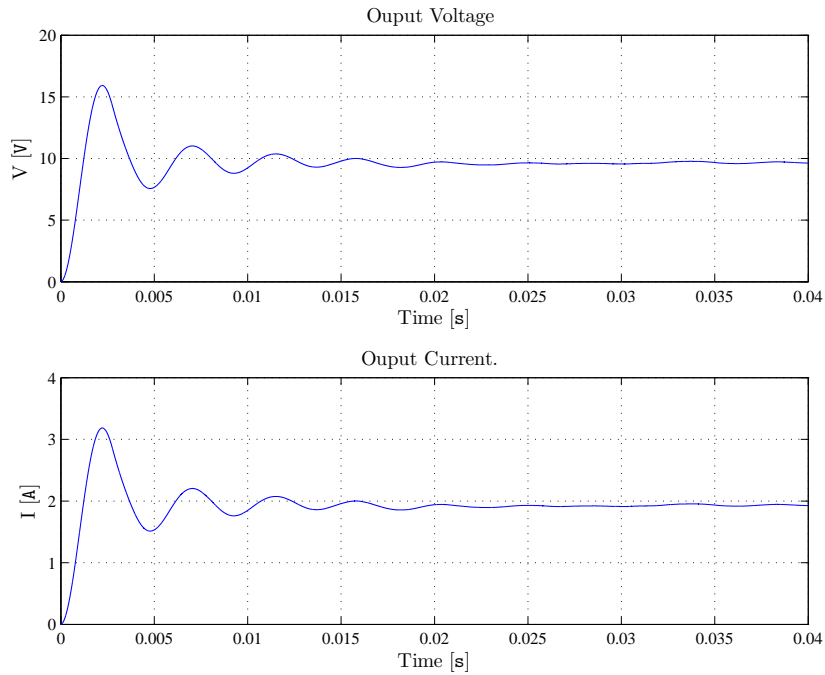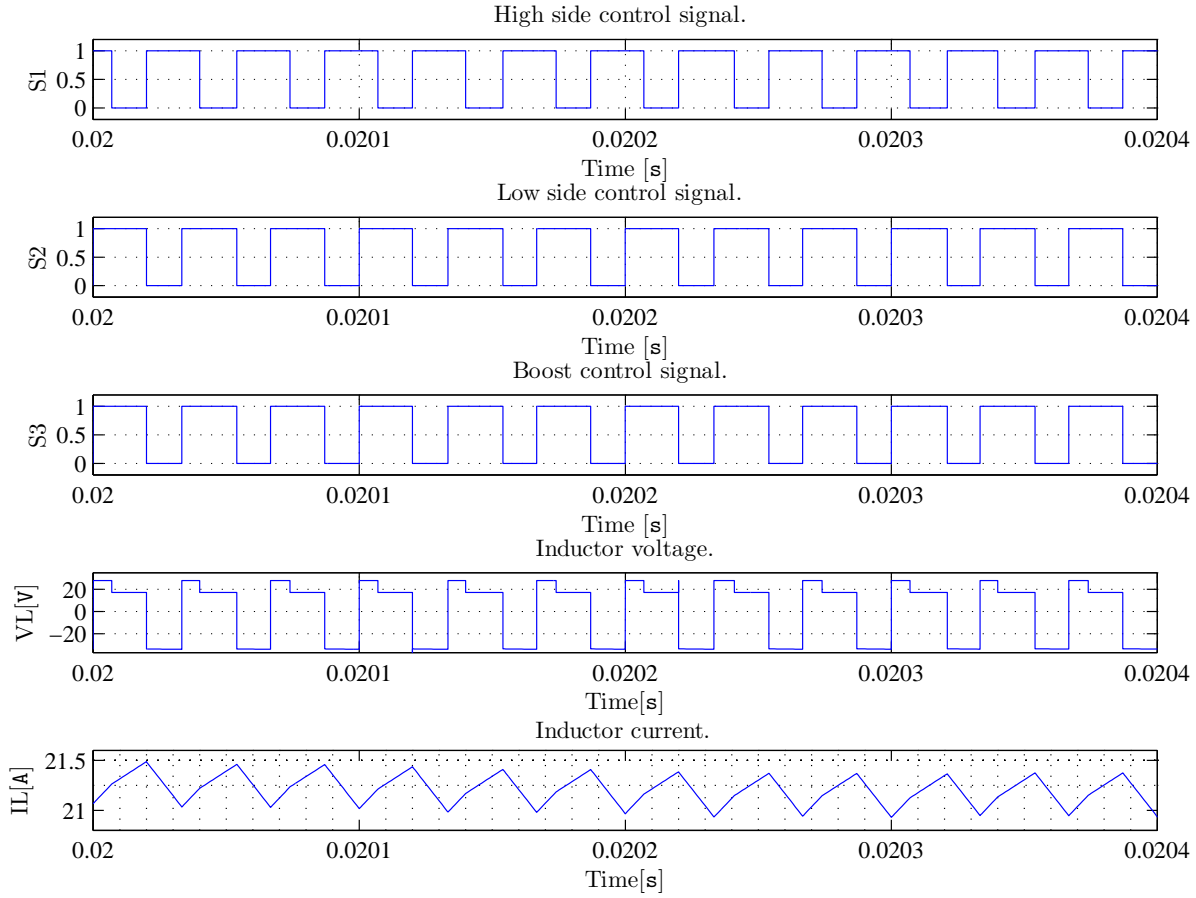

Figure 6.20. Output voltage and current of the proposed converter working in buck mode [$V_1 = 10, V_2 = 18, d_1 = d_2 = 0.4, d_3 = 0; V_o = 9.6$V].
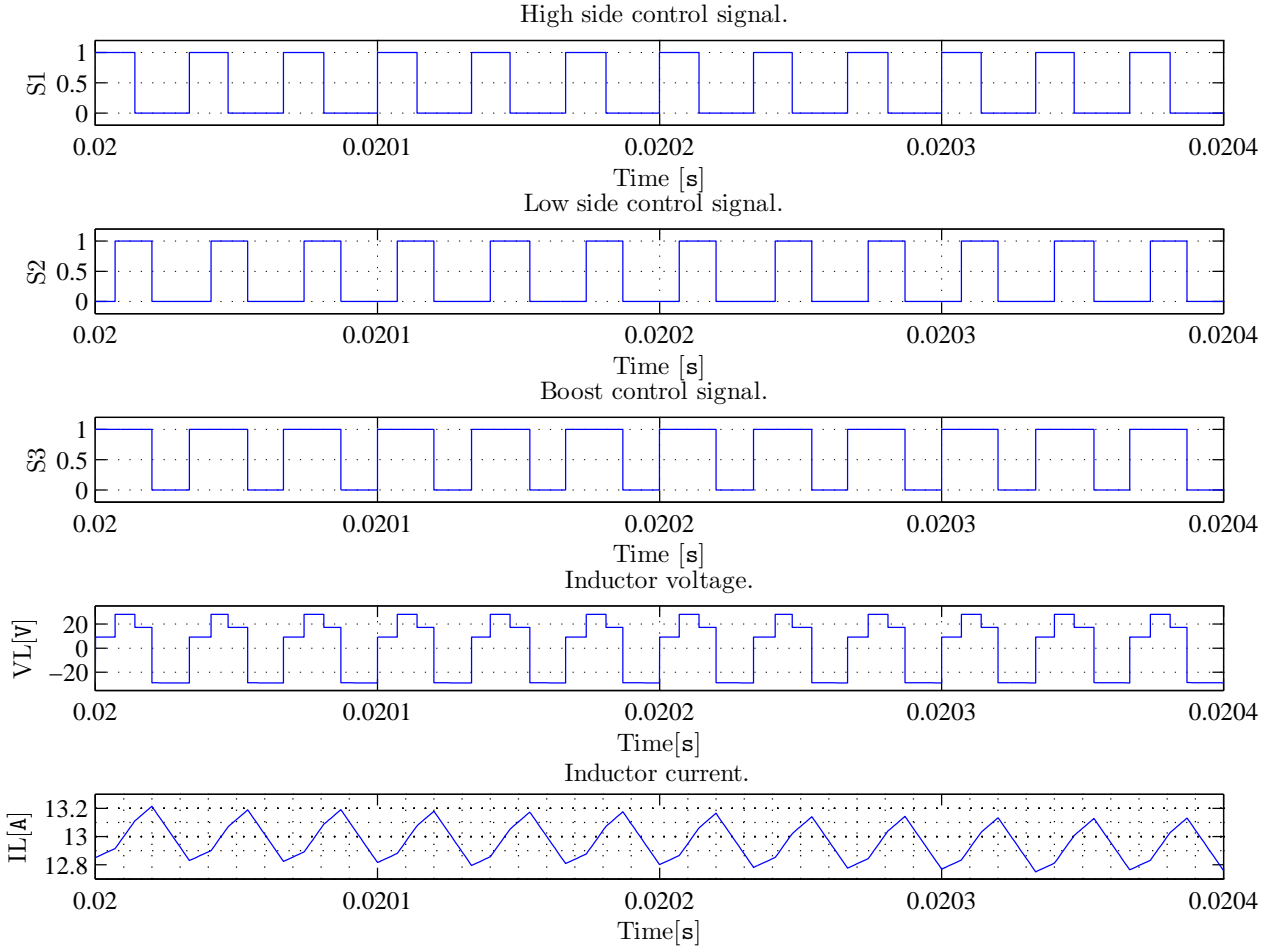
Figure 6.21. Simulation test of the MIC converter proposed under buck-boost mode of operation, switching
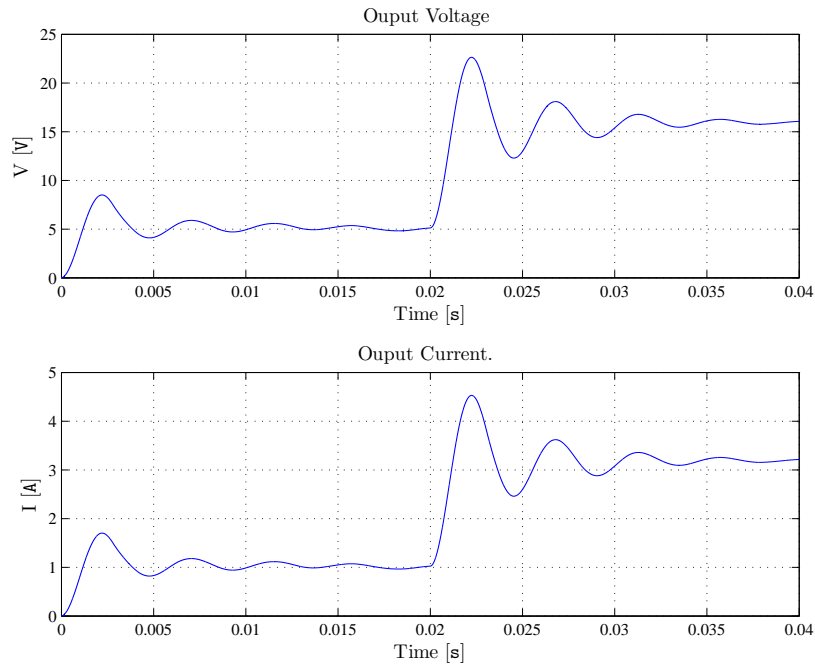signals, I_L and V_L waveforms.[$d_1 = 0.4, d_2 = 0.4, d_3 = 0.6; V_o = 26.5$V]

Figure 6.22. Output voltage and current of the proposed converter working in buck mode [$V_1 = 10, V_2 = 18, d_1 = d_2 = 0.4, d_3 = 0.6; V_o = 26.5$V].

Figure 6.23. Simulation test of the MIC converter proposed under boost mode of operation, switching signals, I_L and V_L waveforms.[$d_1 = d_2 = d_3 = 0.6; V_o = 42.5$V]
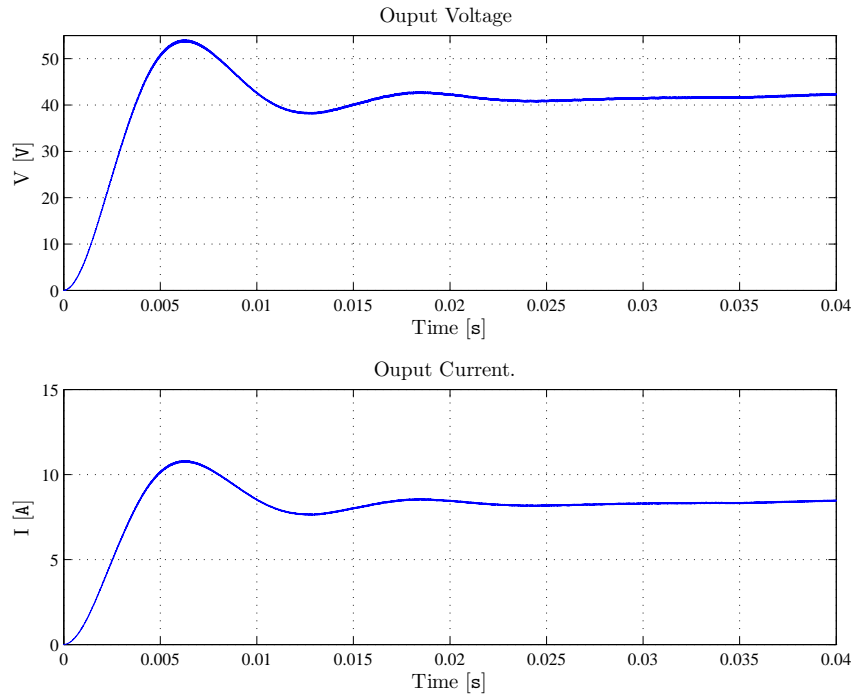
Figure 6.24. Output voltage and current of the proposed converter working in buck mode [$V_1 = 10, V_2 = 18, d_1 = d_2 = d_3 = 0.6, V_o = 42.5$V].

Figure 6.25. Output voltage and current of the proposed converter working in buck mode $[V_1 = 10, V_2 = 18, d_1 = d_2 = [0; 1], d_3 = 0; V_o = [5; 15]\text{V}]$.

will be showed and analysed.

Chapter 7

System design and experimental results

In this Chapter, the design of double input charge controller and load management system will be explained and the laboratory results will be showed and analysed.

7.1 System design

Figure 7.1 shows the system designed for this report. Apart from the double input capability, it is also designed for controlling the charge of a battery and the load management.
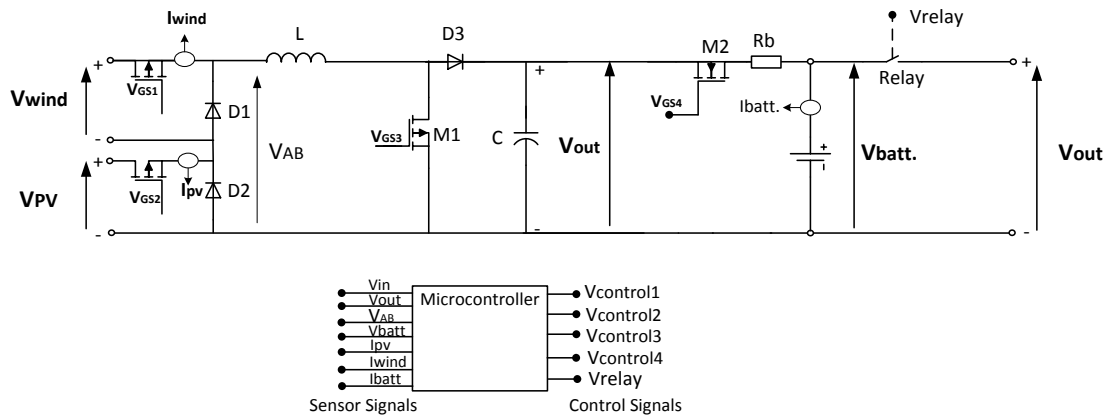
***Figure 7.1.*** Multi input boost converter designed for this report.

Table 7.1. Hybrid System electrical characteristics

| Inductance	2 mH
Capacitor	330µF
Diode	IRF1404(DIODE)
MOSFET	STP12NB3

Due the difficulties to find a fast switching diode for high current, the internal diode of the MOSFET IRF1404 has been used for this purpose, short-circuiting the Gate and Source terminals to block the MOSFET capability.

The microcontroller digital output only produces $[0; 5]$V and low current PWM signals which are not enough for driving the MOSFETs. Thereby, first circuit from Figure 7.2 was built for this purpose. It is formed by an optocoupler and a bipolar transistor. The input of the optocoupler comes from the microcontroller and it is totally isolated from the output. In order to drive the MOSFEt with more current, a bipolar transistor is connected to the output of the optocoupler.The design of voltage supply circuit for each driver is explained below:

However, when testing the system in the lab, as the switching frequency is quite fast (30 kHz), the MOSFET discharge time was too slow. Thereby, it was decided to modify the drive circuit using the High Speed photocoupler PC923. Figure 7.3 shows the schematic diagram of the final drive circuit.
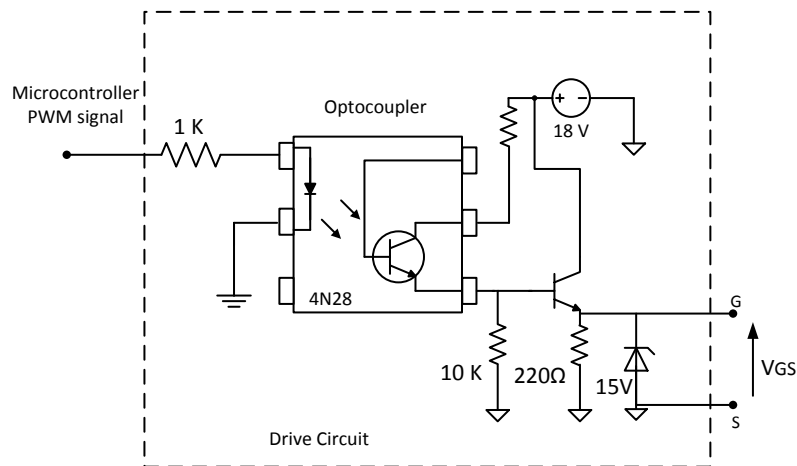
Figure 7.2. Drive circuit for switching the MOSFETs using optocoupler and a bipolar transistor.
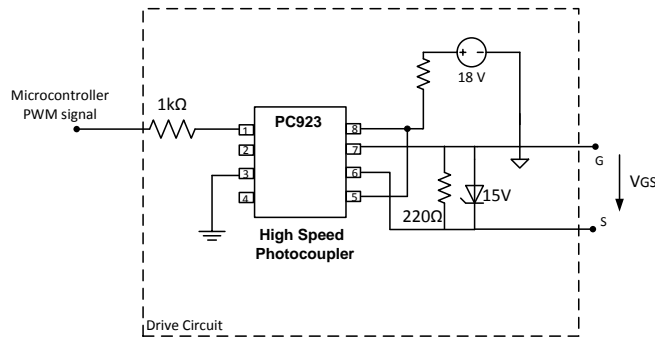
Figure 7.3. Final drive circuit schematic for switching the MOSFETs. In here, a High speed photocoupler is used.

The main problem when designing this converter has been the ground points of the different signals for driving the MOSFETs. Each ground must be isolated from each other in order to connect it to the different "*source*" point of the circuit, in order no to short circuit the system.

It is required then to have an isolated voltage source to supply the drive circuit of each MOSFET. Figure 7.4 shows the power supply circuit designed for this purpose. The battery voltage is converted to square wave voltage by the SG3525, it is possible to obtain trough a transformer three isolated voltage sources which must be rectified in order to get DC voltage supply. The last rectifier DC output is used as reference voltage to regulate the width of the SG3525 and thereby regulate the voltage in the transformer.

For the different test done in the laboratory and due the lack of time, the AC TAP transformer LP-575 has been used. It produces two isolated AC voltages of approximately 12 V and by rectifying and filtering the output, two isolated DC voltage are obtained which can be connected to any point of the circuit. Figure 7.5 shows the schematic diagram of this configuration.

7.2 Experimental results

In order to validate the electrical feasibility of the system designed and built, different test has been done. Figure 7.6 shows the system built for this purpose and the laboratory set-up for testing the
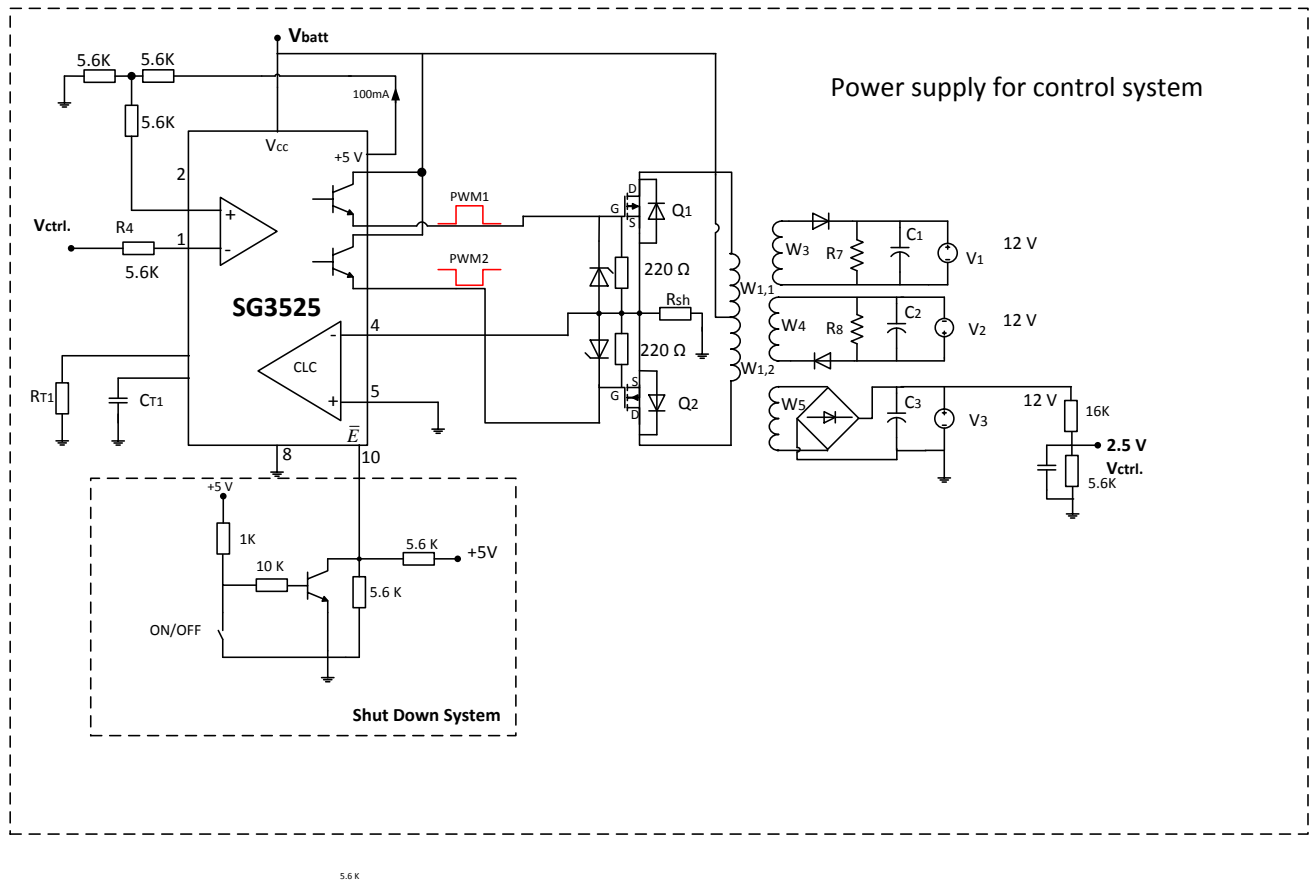
Figure 7.4. Power supply circuit for supplying the control system from the voltage of the battery
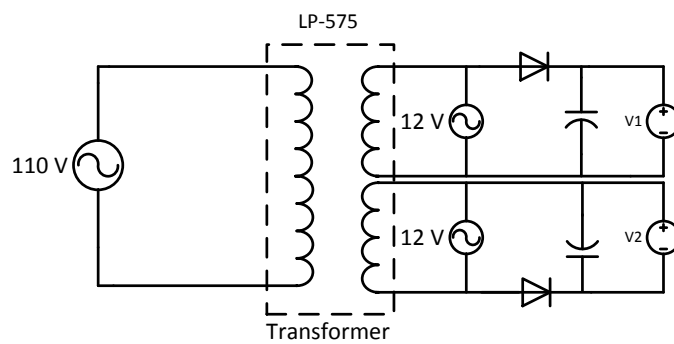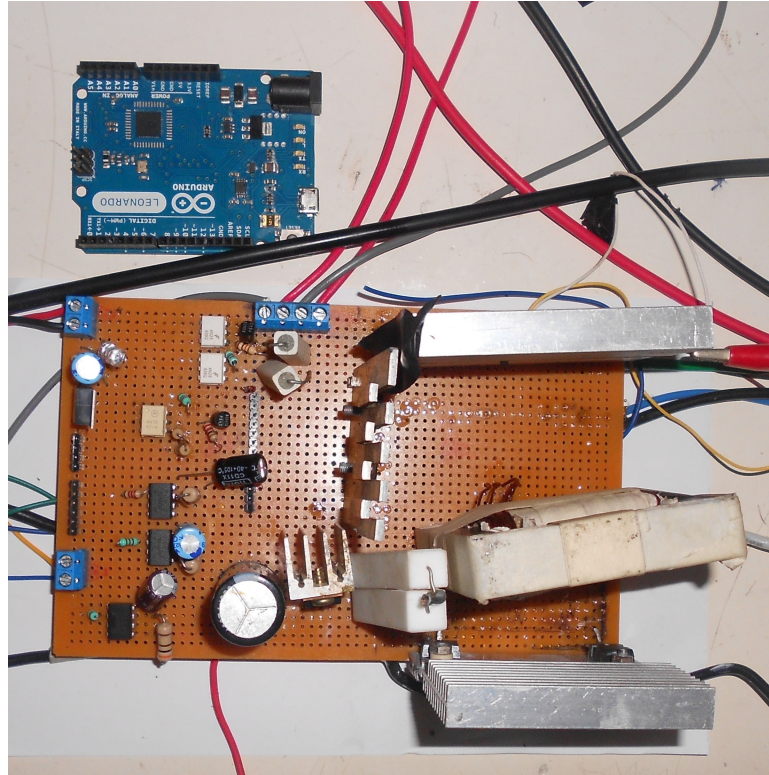

Figure 7.5. Tranformer circuit used for independt ground voltage supplies

power converter.

Figure 7.6. Laboratory set-up for testing the system built.

Test Limitations

It must be mentioned, that due to the lack of laboratory facilities it has not been possible to show better results. The scope accuracy was not the proper one to catch 30000 kHzsignals and for measuring the current through the inductor, a 0.30 Ωpower resistor was placed in series with the inductor tu measure the voltage accross it and get the current. In the simulations, intermediate synchronization was used for the switching signals. However, in order to facilitate the programming of the PWM microcontroller module, rising edge synchronization is used which results in similar behaviour of the system. Test of the three modes of operation will be showed in this section.

Buck mode of operation

In this mode of operation the MIC is tested with the signal S_3 set to zero and the duty cycle of S_1 and S_2 is set to different values. Table 7.2 shows the test conditions of this scenario

Table 7.2. Values used for Buck mode test

Attribute	Value
V_1	5V
V_2	10V
S_1	0.8
S_2	0.6
S_3	0
R_{load}	5Ω
V_o	7.42 V

Figure 7.7 shows the switching signals waveform for this scenario, MOSFET 1 is widther than MOSFET 2 in order to leave more energy to go into the converter.
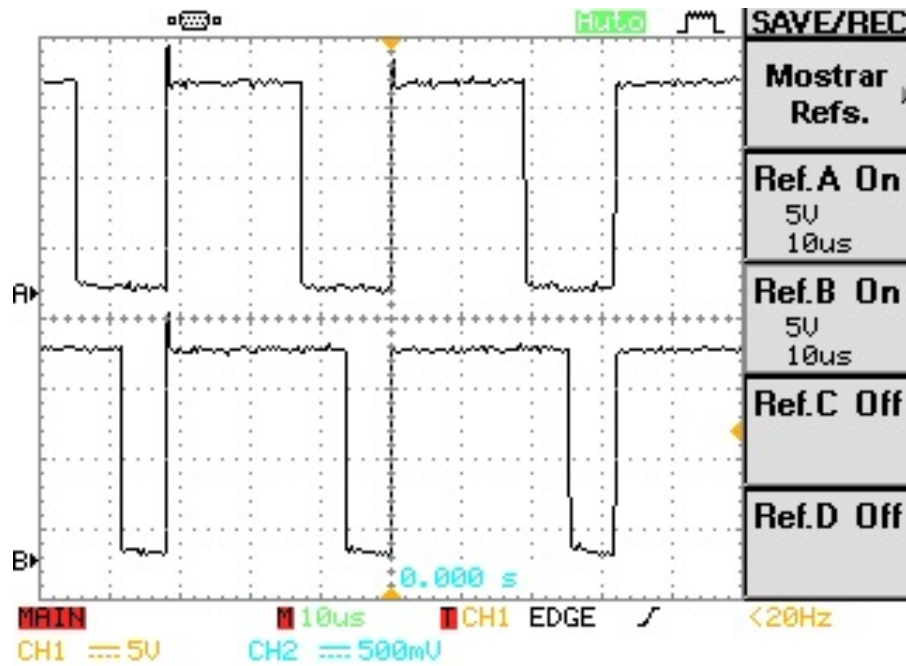
Figure 7.7. Buck mode switching signals [$S_1 = 0.8$ [$S_2 = 0.6$], [$S_3 = 0$]

Figure 7.8 shows the inductor voltage and current waveform, in which it can be appreciated that there is a step on the voltage waveform. As one duty cycle is longer than the other one, the inductor stored energy decreases.
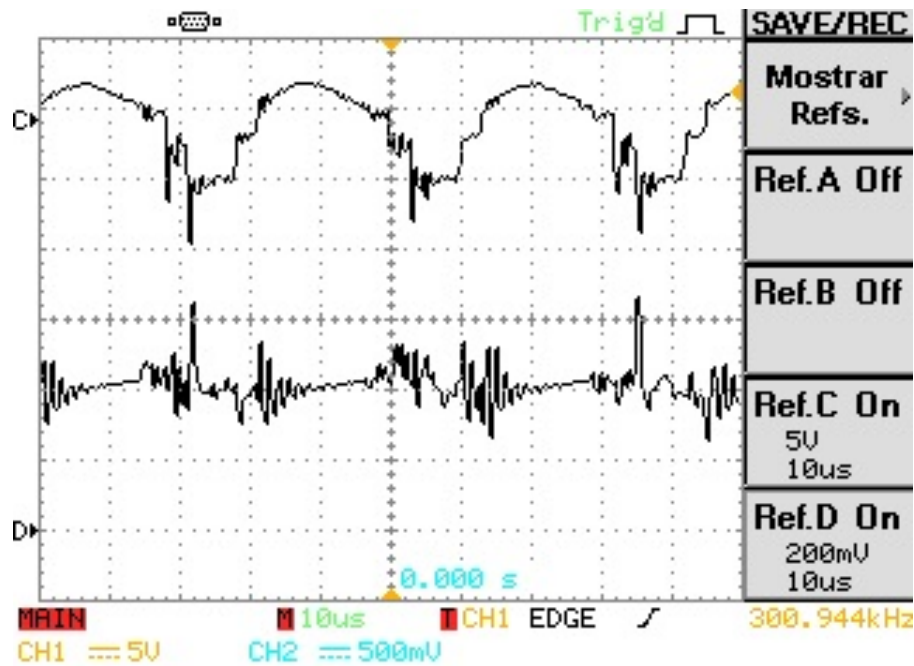

Figure 7.8. Buck mode operation inductor voltage V_L and inductor current i_L

The output voltage of the converter in this case is lowe than both inputs added toguether as it is tested in buck mode of operation.
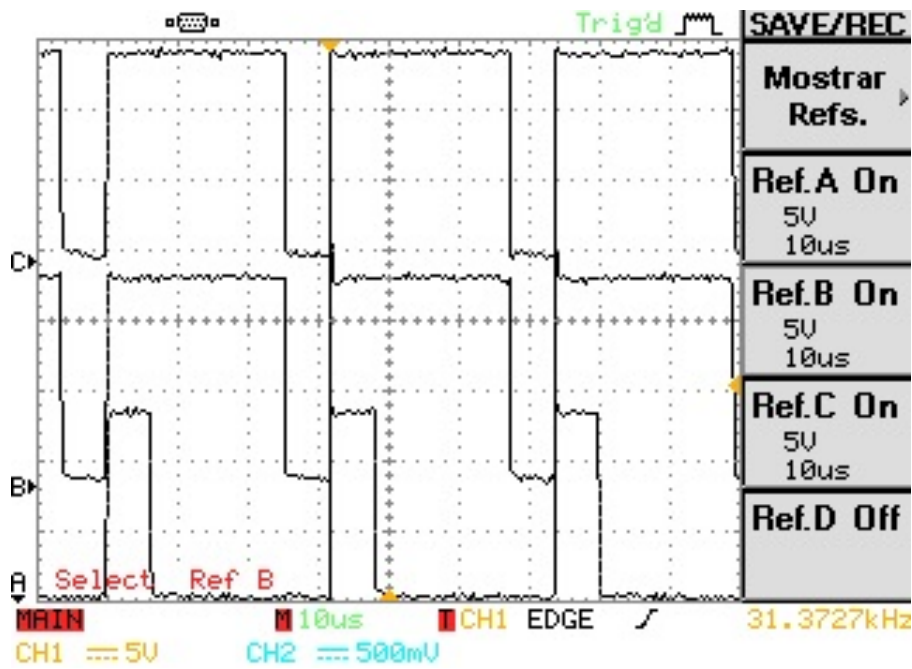
Buck-Boost mode of operation

In here, both voltage input are first reduced and due its boost capability the output voltage is incremented. Resulting in the sum of both input voltages.

Table 7.3 shows the test conditions of this scenario

Table 7.3. Values used for Buck mode test

Atribute	Value
V_1	5V
V_2	10V
S_1	0.8
S_2	0.8
S_3	0.2
R_{load}	5Ω
V_o	12.2V

Figure 7.9 shows the switching signals waveform for this scenario, MOSFET 1 is more width than MOSFET 2 in order to leave more energy to go into the converter.

Figure 7.9. Buck-Boost mode of operation switching waveforms [$S_1 = 0.8$ [$S_2 = 0.8$], [$S_3 = 0.2$]

Figure 7.10 shows the inductor voltage and current waveform, as the three PWM signals are synchronized with the rise edge, there is no step as in the previous case. The ouput voltage is the same as if there was no buck or boost capability.

Boost mode of operation

In here, the output voltage is increased using the boost mode of operation. Table 7.4 shows the test conditions of this scenario.

Table 7.4. Values used for Buck mode test

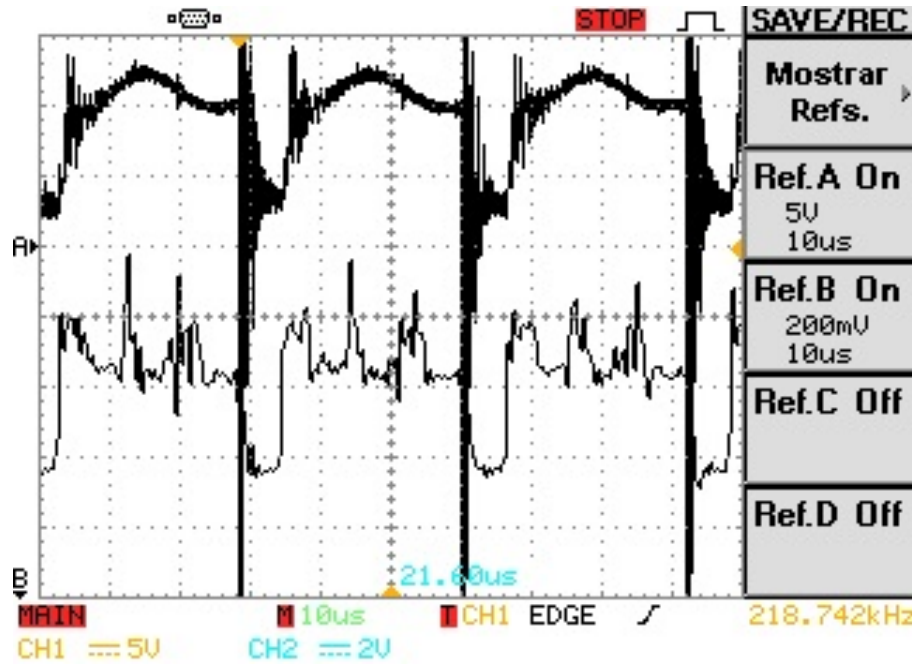| Attribute	Value
V_1	5V
V_2	10V
S_1	0.8
S_2	0.8
S_3	0.3
R_{load}	5Ω
V_o	15.3V

Figure 7.10. Buck boost mode of operation, inductor voltage V_L and inductor current i_L

Figure **??** shows the switching signals waveform for this scenario, S_1 and S_2 are almost and S_3 is set to 20% in in order to leave step up the voltage.
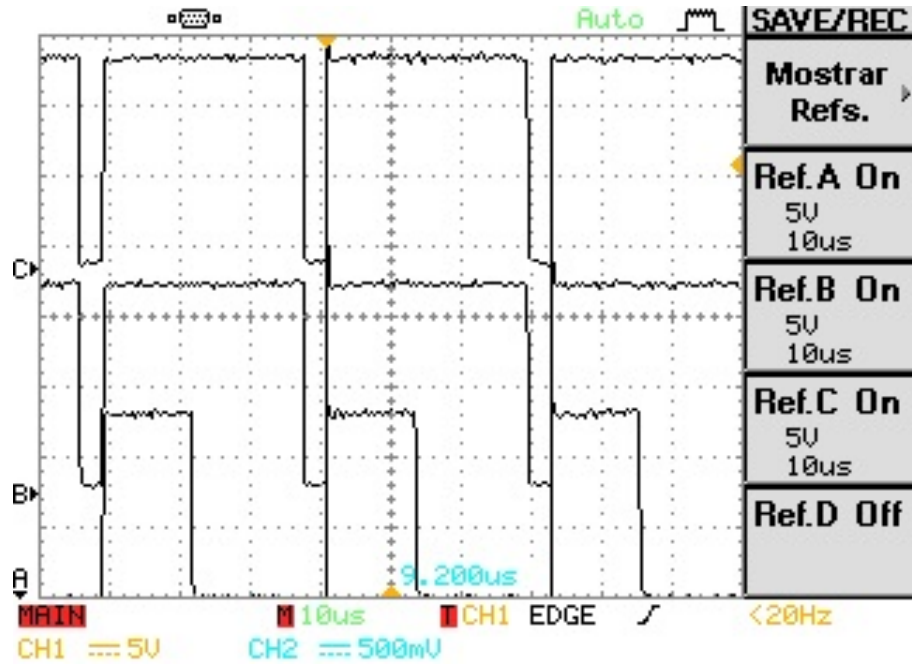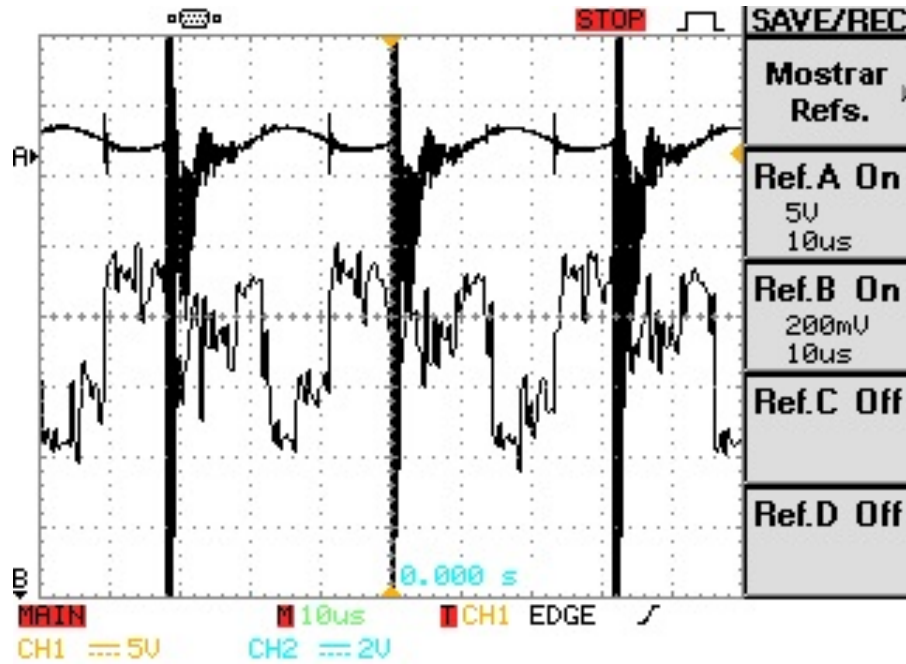

Figure 7.11. Boost mode of operation switching waveforms $[S_1 = 0.8$ $[S_2 = 0.8]$, $[S_3 = 0.3]$

It can be observed that the inductor voltage never goes to zero as both input switches are almost one continuously.

The expected waveform of the current in the inductor in all the cases is impossible to distinguish due all the noise produced by the high switching frequency. The values of the waveforms can not be taken into account due to the high movement and it has been averaged through a tool of the oscilloscope.

7.2.1 Initial test of the efficiency of the system

Several test were done in order to verify the efficiency of the system.

Figure 7.12. Buck boost mode of operation, inductor voltage V_L and inductor current i_L

Low Side Test

The high side switch is kept ON permanently, whereas the low side is OFF. Applying an input voltage in the high side of 12V a ouput voltage of V_o=9.20Vis obtained. The voltage losses is arround 2.8 V, which are produced by the low side diode voltage,the output diode, the ON resistance of the MOSFET and the losses in the inductor.

$$(7.1) \qquad\qquad V_o = V_{in} - V_{RDS} - V_{XL} - V_{D2} - V_{D23} \qquad\qquad [-]$$

High Side Test In the same way as the previous test, but now the low side switch is kept ON permanently and the high side OFF. Applying 12 V in the input, $V_o = 9.52$V similar as the other case.

Both sides working together

Both MOSFETs are ON now and 6V are applied from each voltage source. The output voltage is now V_o=9.52 which is the same as the previous cases.

If we reduce the width of both switching signals to $S_1 = S_2 = 0.5$, the output voltage should theoretically $V_o = d_1V_1 + d_2V_2 = 6$V. In the test V_o is 3.87V because the current is not high so the switching losses can be neglected.

In this test, the efficiency of the system is around 77%. It is really low value but when the system works under high voltage values these losses will be minimal.
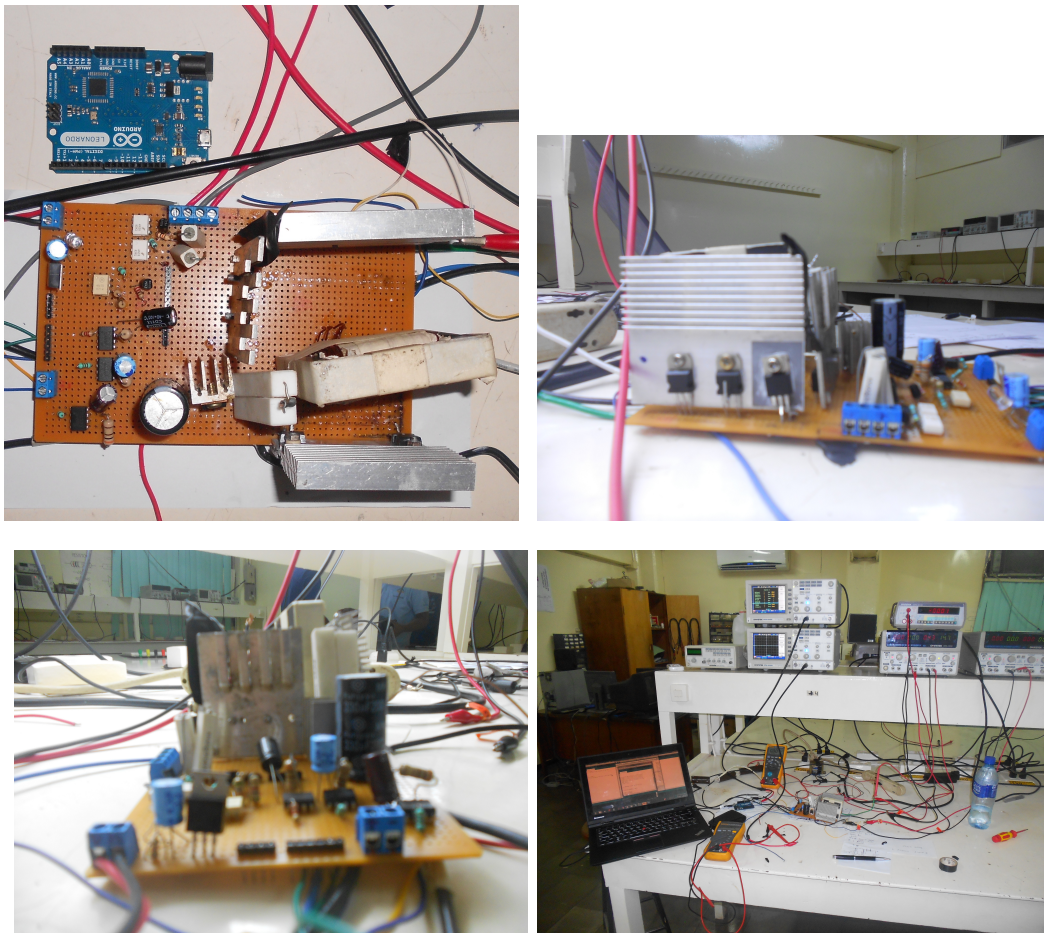
Figure 7.13. Double input buck-boost converter designed and built for this purpose and laboratory set-up.

Chapter 8

Conclusion

The purpose of this project was to study the MPPT systems for both wind and photovoltaic energy, and to design, implement and test a multiple input converter for controlling a hybrid system. This goal has been kept in mind during the whole development of the project.

A deep research about maximum power point tracking algorithm for both wind and photovoltaic energy systems has been done. In addition, a boost converter has been designed and built for controlling independently the wind turbine, but it has not been possible any result from this system.

After researching different MIC converter topologies, the selected one as been analysed and simulated obtained satisfactory results. Small signal analysis and a control system has been proposed.

The system selected has been designed and build, and the laboratory results corresponds with the simulation results and the system behave as expected. Due the lack of facilities at the laboratory, it has not been possible to show better results.

Due to the fact some time was spent building a single input DC/DC converter for analysing the nominal rates of the wind turbine system, there has been to time to test the system built under dynamical conditions.

The system has only been tested under steady state conditions and no control has been tested. Due the lack of time it has not been possible to achieve this goal. However, for further work is expected to test the system with the wind turbine and the solar panel with the control system proposed.

It is also required to fit the system designed with the requirements of both power generation systems. In Chapter 2, it was stated that the PV modules produces an opern circuit voltage of 27V. However the wind turbine is not believe it can produce more than 20 V. Thereby, if both systems are connected to the double input converter designed to a 12V battery, the PV modules will be working under lower power than their capability.

The best solution would be to use 60W PV modules for this wind turbine. Or it is also fesible for the converter to use a higher voltage and charge 24V batteries.

It can be conclude that the goal of the project which was to study the MPPT tracking technology for both PV and wind energy and to build a double input power converter has been achieved. However, it is missing the control part of the system which could not be tested due the lack of time. In addition, the presentation of the laboratory results is not satisfactory more simulation content is missing.

Future prospects

Simulate the whole system control with MPPT with both power generation models and test the whole control with the system implemented under real circustances. Improve the control system for extracting the maximum energy possible. Test the maximum capability of the system built and select in which cases behaves more optimum.

Chapter 9

CD Content

- References.
- Matlab files of simulations.
- P10Report.

Bibliography

[1] A Marandin, C. and Casillas (2013). Small-scale wind power in nicaragua, market analysis 2012 - 2013. Green Empowerment.

[2] Bertenyi, T. and Youngy, T. (2009). Power electronics solutions for vertical axis urban wind turbines. IEE.

[3] company, T. B. (2005). 27tmx data sheet.

[4] DenHerder, T. (2006). Design and simulation of photovoltaic super system using simulink. Electrical Engineering department California Polytechnic State University.

[5] Esram, T. and Chapman, P. L. (2007). Comparison of photovoltaic array maximum power point tracking techniques. IEEE TRANSACTIONS ON ENERGY CONVERSION.

[6] Johnson, D. G. (2001). Wind energy systems. Rainbow Power Company.

[7] Koutroulis, E. and Kalaitzakis, K. (2006). Design of a maximum power tracking system for wind-energy-conversion applications. Rainbow Power Company.

[8] Lalit Kumar, S. J. (2013). Multiple-input dc/dc converter topology for hybrid energy system. Department of Electrical Engineering, MANIT, Bhopal, India.

[9] Mathias Pedersen, Erik Nielsen, C. H. (2011). A domestic wind turbine system for sub-saharan africa. 5th semester Aalborg Univesity group project.

[10] Ned Mohan, Tore M.Undeland, W. P. (1989). POWER ELECTRONICS. Converters, Applications and Design.

[11] Nicola Bianchi, S. B. (2012). Optimal drive and machine sizing for a self starting vertical axis, low power wind generator.

[12] NRG (2007). Renewable nrg systems 40c anemometer, calibrated. Product Specifications.

[13] P.Dunlop, J. (1997). Batteries and charge control in stand-alone photovoltaic systems. fundamentals and application. Florida Solar Energy Center.

[14] Perez, R. (1993). Lead-acid battery state of charge vs. voltage.

[15] Prez, B. H. (2007). Fhotovoltaics: Design and Installation Manual. Solar Energy International and New Society Publishers.

[16] Robert W.Erickson, D. M. (2001). Fundamentals of Power Electronics.

[17] Schilling, S. (1998). Ensuring lead-acid battery performance with renew-it pulse technology. PulseTech.

[18] Technology, W. (2013). Nicaragua: self-reliance and sustainability. Global Trade Media.

[19] Tender, B. (2002). Battery charging basics and charging algorithm fundamentals. Deltran Coorporatio.

[20] V. Salas, E. Olas, A. (2005). Review of the maximum power point tracking algorithms for stand-alone photovoltaic systems. ELSEVIER.

[21] Xiao, W. and Dunford, W. G. (2004). A modified adaptive hill climbing mppt method for photovoltaic power systems. 35th Annual IEEE Power Electronics Specialist Conference.

[22] Yan Li, Xinbo Ruan, D. Y. and Liu, F. (2009). Modeling, analysis and design for hybrid power systems with dual-input dc/dc converter. IEEE.

[23] Yaow-Ming Chen, Tuan-Chuan Liu, S.-C. H. and Cheng, C.-S. (2007). Multi-input inverter for grid-connected hybrid pv/wind power system. IEEE.

[24] Yaow-Ming Chen, Y.-C. L. and Lin, S.-H. (2013). Double-input pwm dc/dc converter for hig/low voltage sources. Power Electronics Applied Research Laboratory Department of Electrical Engineering National Chung Cheng University.

[25] Y.Baghzouz (2012). Photovoltaic devices.

Appendix A

Energy Storage. Lead-acid Batteries

Batteries are formed by electrical cells with a certain DC voltage interconnected in series to supply the nominal voltage of the battery. For renewable energy systems Lead-Acid batteries and Nickel-Cadmium(Ni-Cad) batteries are the most common.

Ni-Cad batteries present better characteristics than Lead-Acid batteries as a longer life-time(more charge and discharge cycles), more resistance to over-discharge and better behaviour under extreme temperature conditions. However, Lead-acid batteries present a lower cost which make them more suitable for small residential applications [13] [15].

However, Ni-Cad batteries present a higher cost and their availability is limited compared with Lead-acid batteries Thereby, lead-acid batteries are commonly used for residential photovoltaic installations and Ni-Cad batteries are used for industrial applications, extreme temperatures locations and small portable devices [13] [15].

Lead-Acid batteries are formed by lead dioxide(PbO2) in the positive plate ,lead(Pb) in the negative plate and sulfuric acid(H2SO4) in the electrolyte. The electrical energy is produced by the chemical reaction between the different materials on each plate and the electrolyte [17].

During the discharge process, the lead dioxide(PbO2) is combined with the sulphate(SO4) of the electrolyte forming lead sulphate(PbSO4) in the positive plate. Similarly, in the negative plate the same process occurs, the lead reacts with the sulphate forming lead sulphate on the plate. The molecules of oxygen are lost at each reaction [17].

If electrical current is passing through the battery, the cycle is reverse than during the discharge. The lead sulphate formed in both plates splits in lead(Pb) and acid(SO4), and reacting with the hydrogen(H) of the water in order to restore the electrolyte. The lead and the oxygen combines again forming lead dioxide(PbO2) in the positive plate. In the negative plate only lead is formed [17].

When the discharged process occurs fast more sulphate is generated. It is important that the sulphates do not crystallize on the plates by leaving the battery discharged during a long period or by improper recharge, because they will not recombine again into active materials. In addition high level of crystal sulphate on the plates can damage the battery [13] [19].

Thereby, it is required to control the discharge and charge battery process which is usually charge algorithm and consists on different electrical stages software controlled.

Appendix B

Single DC DC converter

During the procedure of this report, it was required first to build a single DC/DC converter for the VAWT system for controlling it and being able to charge a battery. Due to the fact the VAWT system was located far from the university, a data logger was built to record measurements of the power produced and the wind speed.

Following initial contacts, the first requirement was to step up the voltage as the wind turbine was producing lower voltage than the battery voltage level and thereby, no energy was transferred into the battery. By doing this, for low wind speeds the voltage could be increased and the little energy produced was stored into the battery. When there would be high wind speed, the power converter could be turned off and the energy would be transferred directly to the battery.

In this Chapter, there will be first a brief study of the principle of working of the boost converter. Afterwards, the designed system will be explained.

B.1   Boost converter analysis

Figure B.1 shows the basic topology of a Boost or Step-Up converter. The switch has two possible states ON or OFF, which will depend on the PWM control signal.
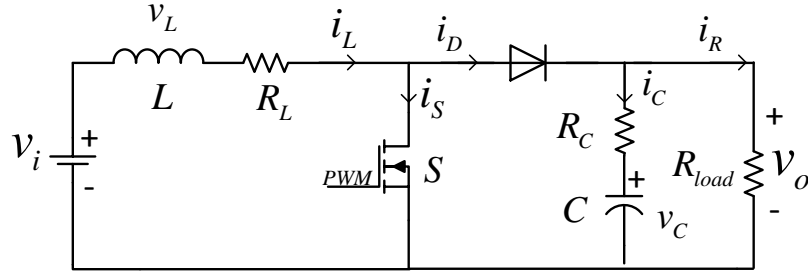
Figure B.1. Boost converter circuit

When the switch is ON, the current flows through the circuit as shown in Figure B.2. The input current, which is the same as the inductor current I_L, goes through the switch as it is closed. The output voltage is supplied by the energy stored in the capacitor. The voltage across the inductor is expressed in Equation B.1.
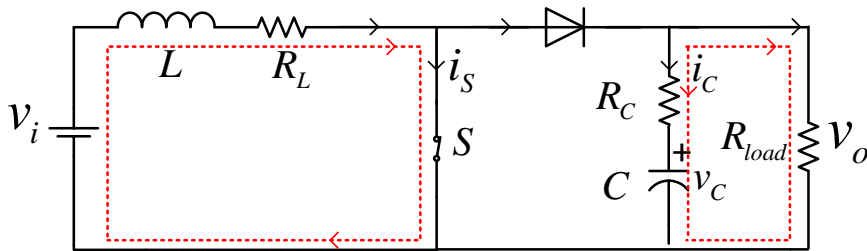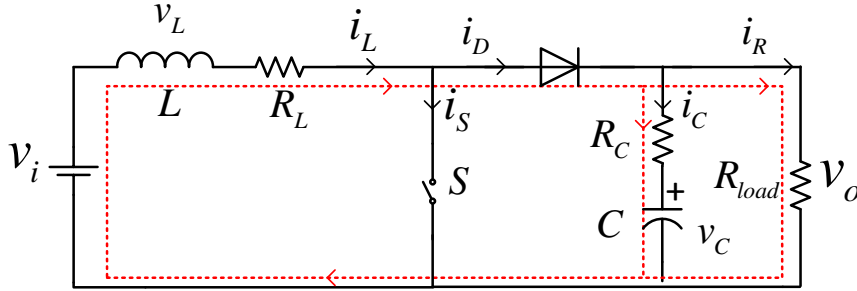

Figure B.2. Boost converter circuit when the switch is ON

(B.1)
$$v_L = v_i$$
[V]

The current through the capacitor is defined in Equation B.2

(B.2)
$$i_C = -\frac{V_o}{R_{load}}$$
[A]

Figure B.3 shows the boost converter when the switch is OFF. In here, the energy stored in the inductor and the input current recharges the capacitor and supplies the load.

Figure B.3. Boost converter circuit when the switch is OFF

Equations B.3 and B.4 define the voltage across the inductor and the current through the capacitor.

(B.3)
$$v_L = v_i - v_o$$
[V]

(B.4)
$$i_C = I_L - \frac{V_o}{R_{load}}$$
[V]

In Figure B.4 it has been sketched the equations of the voltage across the inductor and the capacitor current during one switching period:
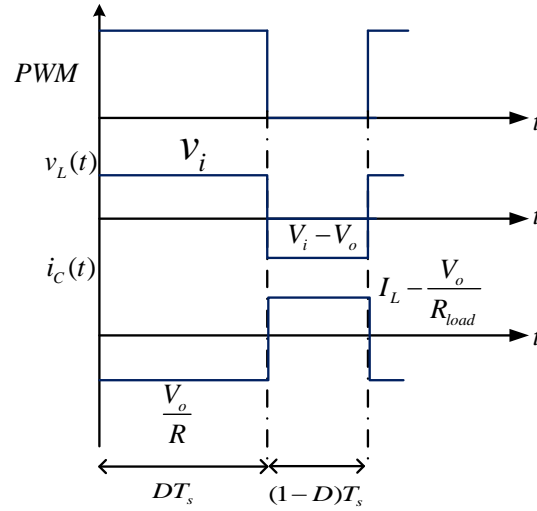
The current through the inductor can be calculated as showed in Equation B.5:

(B.5)
$$i_L = \frac{1}{L} \int_0^{T_s} v_L(t)dt + i_L(0)$$
[A]

From (B.1), (B.3) and (B.5) it is possible to derive the current flowing through the inductor, by integrating the voltage across the inductor during one switching time T_s as shown in Equation B.6 and (B.7).

(B.6)
$$i_L = \frac{1}{L} \int_0^t (v_i)dt + I_1 = \frac{1}{L}v_i t + I_1$$
[A]

(B.7)
$$i_L = \frac{1}{L} \int_0^t (v_i - v_o)dt + I_1 = \frac{1}{L}(v_i - v_o)t + I_1$$
[A]

Figure B.4. Voltage and current waveform of the inductor voltage V_L and the capacitor current I_C waveforms.

where I_1 is the previous value of the current in the inductor.

According to the second-volt balance theorem in steady state the variation of the current in the inductor in one switching period must be the zero, $i_L(T_s) = i_L(0)$. Then Equation B.5 can be expressed as (B.8).

$$(B.8) \qquad \int_0^{T_s} v_L(t)dt = 0 \qquad [\text{-}]$$

If Equation B.6 and B.7, and applying the concept stated in B.8 are combined depending on the state of the PWM signal and equated to zero, Equation (B.9) is derived:

$$(B.9) \qquad v_i DT_s + (v_i - v_o)(1 - D)T_s = 0 \qquad [\text{A}]$$

Simplifying Equation (B.9) the relation between the input and output voltage can be derived as shown in Equation B.10

$$(B.10) \qquad V_o = \frac{V_i}{(1 - D)} \qquad [\text{A}]$$

Thereby, the conversion ratio of the boost converter is presented in Equation B.11 as showed in Figure B.5

$$(B.11) \qquad M(D) = \frac{1}{1 - D} \qquad [\text{-}]$$

When the duty cycle D rises the output voltage V_o increases. When the duty cycle reaches its maximum value $D = 1$ the output voltage ideally tends to infinity [16]. Thereby the boost converter is able to produced on its output a greater voltage than at its input.
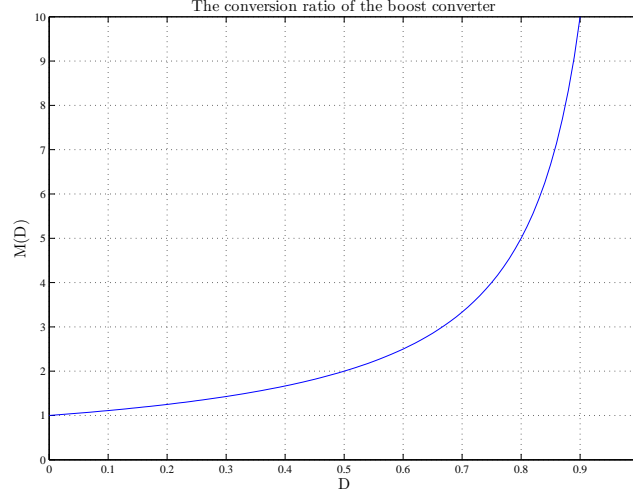
Figure B.5. Conversio ratio curve characteristic of the boost converter

The voltage in the capacitor can be calculated by integrating the capacitor current I_C during one switching period. The variation of the voltage in one switching period in steady state conditions must be zero. Thus $v_c = v_C(0)$ and it leads to Equation B.12:

$$(B.12) \qquad v_c(T_s) = \frac{1}{C} \int_0^{T_s} i_C(t)dt + v_C(0) \rightarrow (-\frac{V_o}{R_{load}})DT_s + (I_L - \frac{V_o}{R_{load}})(1-D)T_s = 0 \qquad [A]$$

Solving Equation B.12 and isolating the inductor current I_L the follow equation is derived B.13:

$$(B.13) \qquad\qquad\qquad\qquad I_L = \frac{V_O}{(1-D)R_{load}} \qquad\qquad\qquad\qquad [A]$$

Combining Equations B.13 and (B.10) the inductor current DC component depending on the duty cycle D, the input voltage V_i and the load resistance R_{load} is shown in Equation B.14

$$(B.14) \qquad\qquad\qquad\qquad I_L = \frac{V_i}{(1-D)^2 R_{load}} \qquad\qquad\qquad\qquad [A]$$

The input current of the converter is the same as the inductor current from Equation (B.14). As the output voltage of the boost converter is greater than the input and output power are ideally equal, the output current must be lower than the input current. In a real system, when the duty cycle rises close to 1, the current in the inductor becomes very high which causes big losses due to the inductor winding resistance and semiconductor R_{ON} resistance. Thereby, the efficiency of the Boost converter decreases significantly [16].

Inductor ripple

Inductor waveform is sketched in Figure (B.6). From this graph the inductor ripple ΔI_L can be determined:

During the first time interval $t = [0; DT_s]$ the change in the inductor value is showed in (B.15). Once this has been stated the ripple in the inductor, ΔI_L can be determined:

(B.15)
$$2\Delta I_L = \frac{V_i}{L}DT_s \rightarrow \Delta I_L = V_i\frac{DT_s}{2L}$$
[-]
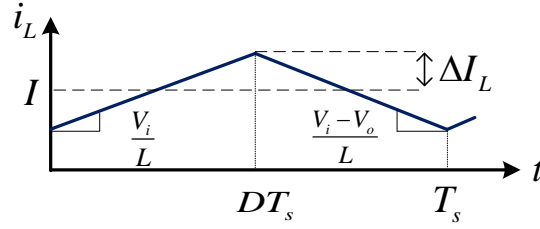
***Figure B.6.*** Inductor waveform during one period.

Output voltage ripple

The output voltage ripple is defined by the variation of voltage in the capacitor, Δv_c. The voltage in the capacitor v_C can be determined knowing the capacitor current, i_C.

From Equation B.2 and B.4 the slope of the capacitor waveform $v_C(t)$ at both time intervals can be derived (B.16):

(B.16)
$$\frac{dv_C(t)}{dt} = \frac{i_C(t)}{C} = \frac{-V_O}{R_{load}C}$$
$$\frac{dv_C(t)}{dt} = \frac{i_C(t)}{C} = \frac{I_L}{C} - \frac{V_O}{R_{load}C}$$
[-]

The capacitor voltage v_C is sketched in Figure B.7. The slope of the waveform during the first interval times the time period is equal to to times the voltage ripple. From this statement, the ripple in the capacitor v_c can be determined B.17:

(B.17)
$$C = \frac{V_o}{2R_{load}\Delta v_c}DT_S$$
[-]
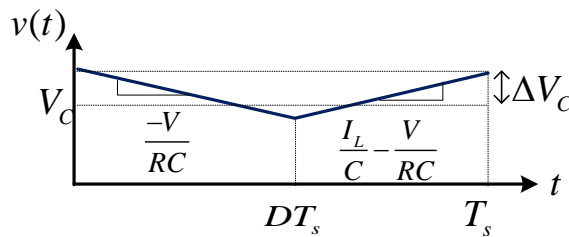
***Figure B.7.*** Boost converter ouput voltage waveform.

Equations B.16 and B.15 can be used to determine the value of the capacitor and the inductance depending on the ripple desired [16].

B.2 Boost converter design and data logger

Figure B.8 shows the main circuit diagram of the boost converter and battery controller designed for the wind turbine system. The values of the main components of this circuit schematic are shown in Table B.1.

The first part of the circuit is formed by the Boost circuit explained in Chapter B which is connected to the output of the rectifier. In here, the input voltage and current are measured by the microcontroller in order to generate the control signal to switch the MOSFET, using the MPPT algorithm described in Chapter3.

The second part of the circuit is the battery charge controller and load management explained in Chapter **??**. It consist on a P-Channel MOSFET, a resistor R_b(it is used to reduce the spikes produced by the switching current flowing into the battery) and the relay used to shut down the load in case of over-discharge. In here, the voltage and the current are sensed to regulate the current flowing into the battery and the battery voltage level.
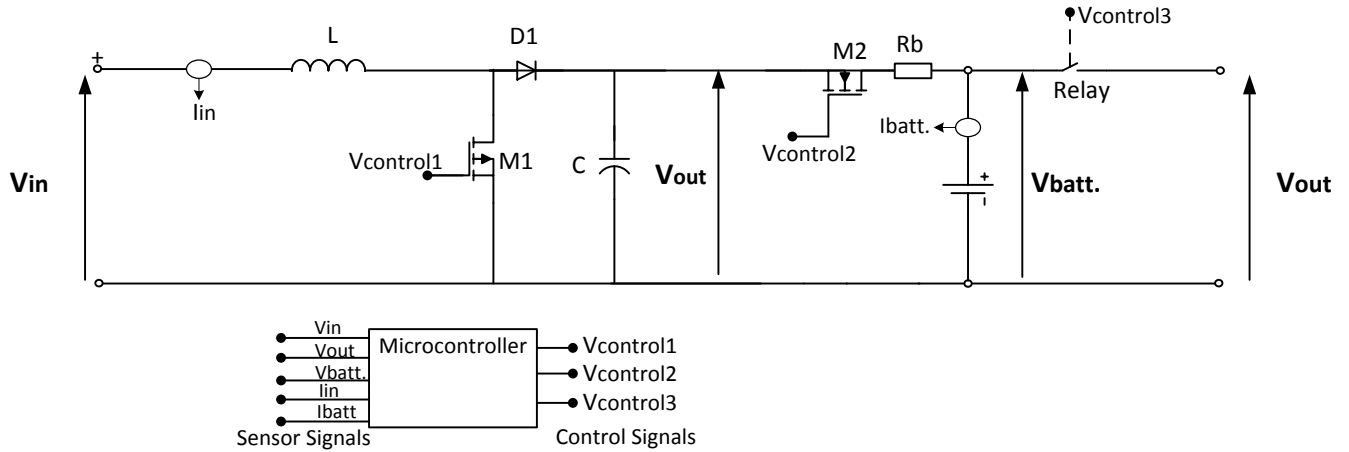

Figure B.8. Boost converter and control circuit designed for this purpose.

Table B.1. Boost converter and charge controller components used.

Name	Symbol	Value
Inductor	L	1 mH
Capacitor	C	330μF
Resistor	R_b	
Diode	D1	MOSPEC S20C40C
MOSFET	M1	FQP12N20
MOSFET	M2	FQP12P20
Relay	-	RP310012
Microcontroller	-	Arduino Uno

In order to characterize the power produced by the wind turbine designed, an anemometer is used to measure the wind speed. The anemometer used is called $NRG\#40$ which generates an output AC voltage signal and its frequency depends on the wind speed [12]. Thus, it is required to read the frequency of the signal in order to know the wind speed.For reading the signal with the microcontroller, this signal needs to be conditioned as it has a minimum amplitude of 0.3V and the microcontroller can not read negative signals. Therefore, an amplification and zero-crossing detector system has been implemented. Figure B.9 shows the analog circuit designed for this purpose.

Table B.2 shows the values of the resistors used on the analogue circuit used for conditioning the output signal of the converter so it can be read and processed by the microcontroller. The value of R_f is designed according to the gain desired for the ouput of the first amplifier, which in this case $G = 4$.
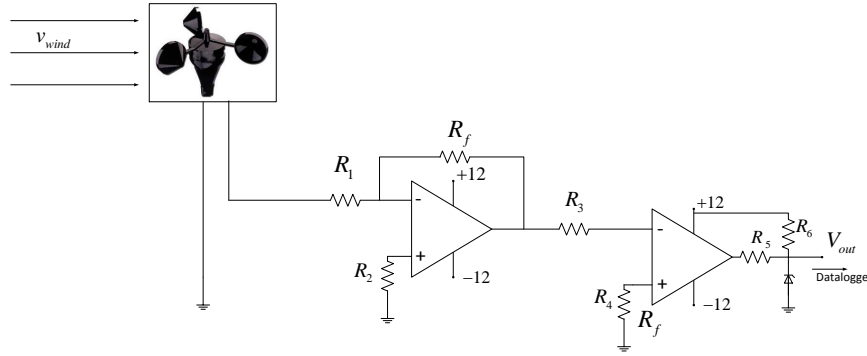
Figure B.9. Analog conditioning circuit designed for obtaining the wind speed fromt the anemometer NRG #40S

**Table B.2.** Anemometer conditioning circuit resistor values used.

Resistor	Value
R_f	20kΩ
R_1	5kΩ
R_2	2kΩ
R_3	2kΩ
R_4	2kΩ
R_5	18kΩ
R_6	18kΩ

Figure B.10 shows the signals obtained from the circuit designed on the simulation, where the green signal is the output of the anemometer, the blue one the amplified signal and the red one the square signal obtained by detecting the zero-crossing.
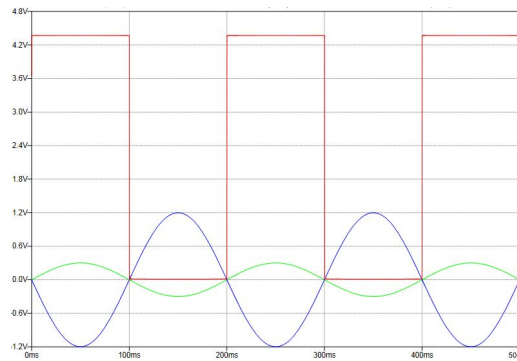

Figure B.10. Signals of the conditioning of the output of the anemometer. Green signal, AC signal from the anemometer, Blue signal the one after the first amplifier and the red one the output signal of the circuit.

As seen in the graph of the previous Figure B.10 a 0-4.3V square wave signal is obtained from the sinewave signal from the anemometer. Thus, the output signal from this circuit can be connected to the microcontroller and it can detect the frequency of the signal and thereby, process the wind speed.
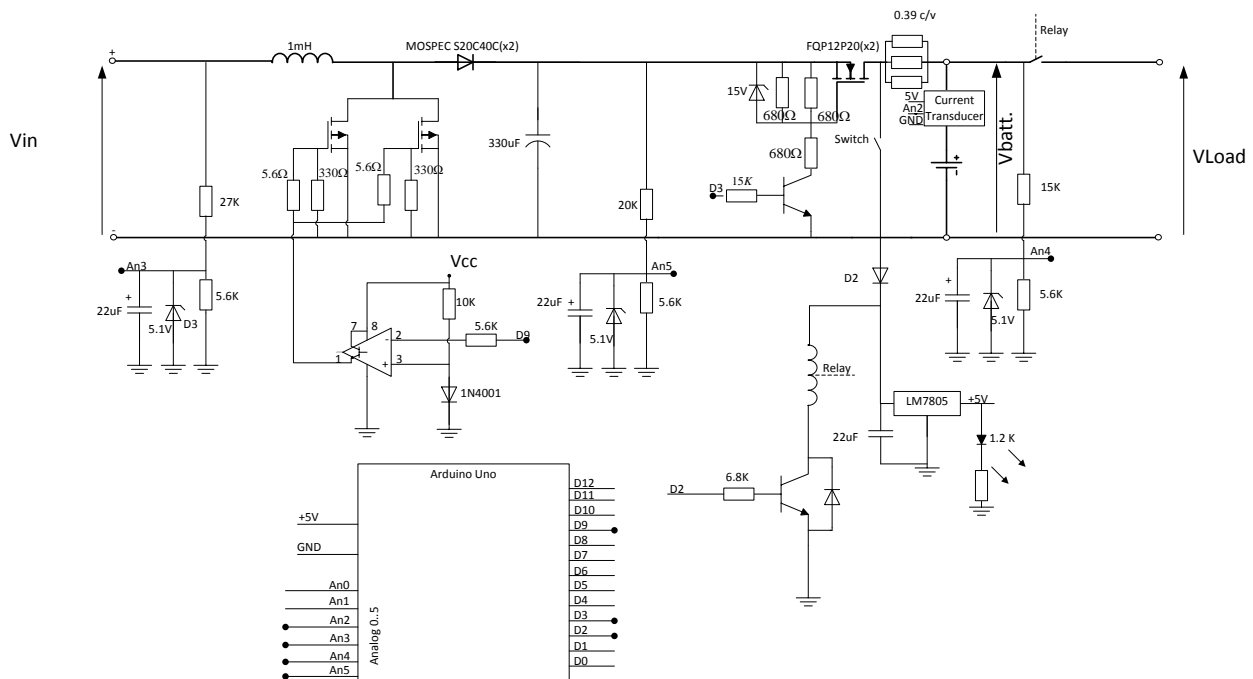
Figure B.11. Wind turbine charge controller designed for this report. It is formed by a boost converter and the battery controller and load management system.
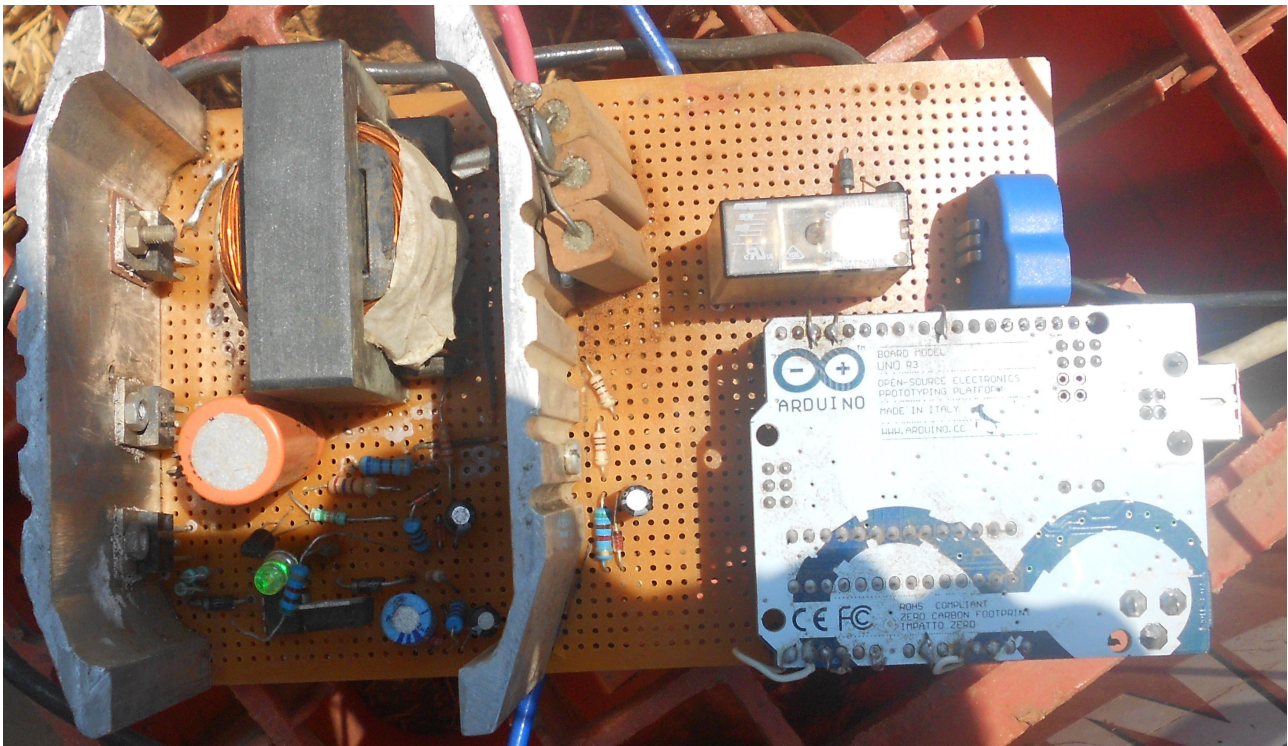
Figure B.12. Boost Converter built for controlling the wind turbine system and charge the battery

Appendix C

Small signal analyse for multiple input DC/DC converter

<div style="height:1px;"></div>

$$(C.1) \qquad v_c(s) = -i_{load} Z_o \qquad [V]$$

$$(C.2) \qquad Z_o = \frac{sL}{s^2 LC + \{1 - (d_1 - d_2 + d_{12})\}^2 + s\frac{L}{R}} \qquad [V]$$

$$(C.3) \qquad v_c(s) = G_{V,v_1} v_1(s) \qquad [V]$$

$$(C.4) \qquad G_{V,v_1} = \frac{\{1 - (d_1 - d_2 + d_{12})\} d_1}{s^2 LC + \{1 - (d_1 - d_2 + d_{12})\}^2 + s\frac{L}{R}} \qquad [V]$$

$$(C.5) \qquad G_{V,v_2} = \frac{d_2(1 - (d_1 + d_2 - d_{12}))}{s^2 LC + (1 - d_1 - d_2 + d_{12})^2 + s\frac{L}{R}} \qquad [V]$$